University of Reading

Mathematical Modelling of Liquid Transport in Porous Materials at Low Levels of Saturation

Submitted for the degree of Doctor of Philosophy

Department of Mathematics and Statistics

Penpark Sirimark

August 2019

Abstract

Persistent (low volatility) liquids can disseminate significantly in porous substrates and wet large volumes before they are removed by evaporation or chemical processes. The liquid saturation during this kind of dissemination process quickly reaches very low levels, well below 10% of the available void space, and the liquid dispersion enters a special regime of spreading, when the transport predominantly occurs over surface elements of the porous matrix.

On the 'macroscopic' level, this phenomenon can be described by a special super-fast non-linear diffusion model. But, the model requires the knowledge of permeability coefficients defined by 'microscopic' mechanisms. The focus of this study is on the mathematical problems associated with the 'microscopic' level, that is on the details of the surface diffusion processes to obtain accurate definitions of the 'macroscopic' parameters. We consider two kinds of porous structures with representative properties, paper-like and particulate porous materials, and as a result, two different model approaches, a network model and a surface diffusion model based on the Laplace-Beltrami operator and on the associated Laplace-Beltrami boundary value problems. We demonstrate their feasibility by applying numerical methods, specifically, surface finite elements techniques.

We will show, in the Thesis, that the network model is capable of accurately reproducing macroscopic descriptions of the fibrous material, while at the same time providing necessary permeability coefficients of the porous network with minimal assumptions. In the case of particulate porous media, we will demonstrate that, solutions to the Laplace-Beltrami boundary value problem can be used to obtain surface permeability of both single porous matrix elements and their interconnected compositions. We will also demonstrate, for the first time, how effects of tortuosity of the surface flow can be easily obtained while analysing solutions of the Laplace-Beltrami boundary value problem set in the multiply-connected domains formed by mutually coupled particles. Overall, results of this study will improve our understanding of microscopic dispersion processes central to applications of macroscopic descriptions formulated at low saturation levels. Numerical studies of the Laplace-Beltrami boundary value problem using the surface finite element method are interesting on their own, since they demonstrate that similar convergence rates (using relatively standard surface element settings) can be achieved in the domains with smooth boundaries to those regularly observed in the problems without domain boundaries.

Therefore, due to the fundamental advances achieved in the study, the macroscopic descriptions used in practice at low saturation levels obtained rigorous foundation and practical recipes, which can be directly used in applications.

Declaration

I confirm that this is my own work and the use of all materials from other sources has been properly and fully acknowledged.

Acknowledgements

Firstly, I would like to express my deepest appreciation to my respected supervisor Dr. Alex V. Lukyanov and co-supervisor Dr. Tristan Pryer for their valuable discussions and for their important suggestions during my research period. They have gone the extra mile to help me, and I consider them as my family. I am extremely blessed to have supervisors who cared a lot for my work, and who always answered to my questions at any point of time. This thesis could not have been possible without their encouragement and persisted motivation indeed.

I would like to express my gratitude to my Thai government who supported the financial aspects of my education, and I also thank Rajamangala University of Technology Isan which gave me a good opportunity to pursue my study abroad.

Furthermore, I also wish to extend my thanks to all of my teachers for sharing their knowledge which helped me immensely in my higher education.

I would like to thank my mother and my grandmother for their understanding, supporting and their unceasing patience towards my research.

Finally, I am grateful to all my colleagues and the department of Mathematics and Statistics staff of the University of Reading for supporting the preparation of my thesis.

Contents

Chapter 1

Introduction

Most materials we encounter in everyday life, ranging from ordinary rocks, soils and clothing to sophisticated household products have porous structure. The structure of the porous materials has direct implications on their mechanical and transport properties, such as rigidity, plasticity, thermal conductivity, gas diffusivity and the coefficients of liquid dispersion, which are in turn associated with the relevant processes, such as deformation, gas diffusion and liquid dispersion. The phenomenon of liquid dispersion is of particular importance due to its role in modern technological applications (for example, filtering, medical diagnosing and cleaning), and geophysical and agricultural processes, (for example, land sliding and flooding). Understanding of the liquid transport in porous media is crucial in the design and assessment of building facilities, for example in construction of dams and artificial reservoirs, and in the environmental analysis of dissemination processes (Baker 1963; Bear and Verruijt 2012; Koorevaar et al. 1983; Bear and Verruijt 1987).

The abundance and variety of liquid transport phenomena in porous media, and their importance have been stimulating research in this direction providing us with practical and reliable mathematical models, which can be further used in the analysis and simulations. Until recently, the least studied area of liquid transport was at low and very low concentrations of transporting liquids in porous matrices (Herminghaus 2005; Lukyanov et al. 2012; Scheel et al. 2008a,b). The mathematical aspects of modelling of this kind of processes is the main subject of this doctoral study. We aim to understand general and specific features relevant for the mathematical description of this particular regime of spreading.

To understand the setting of that specific research area, we first consider general aspects of transport phenomena, which are relevant to the mathematical modelling in porous materials.

1.1 Structure and Properties of Porous Media

1.1.1 Porosity and Saturation

One of the main parameters used in the description of porous materials is porosity, commonly, and in the thesis, designated by ϕ, the detail is in (Koorevaar et al. 1983). Generally speaking, porosity is the measure of the void space in a porous matrix, Fig.1.1. It is defined by the ratio of the total volume of voids V_v in a sample volume element V of the material, that is

$$\phi = \frac{V_v}{V}.$$

Depending on the application, one can distinguish porosity defined with respect to the total or with respect to the available void space. The porosity defined with respect to the available void space, which is also often called the effective porosity and is measured by standard mercury intrusion or gas expansion methods, is of particular importance, since only open-to-flow pores can participate in the liquid transport processes (Sahimi 1993). Note, further in the study, the porosity is defined with respect to the available void space.

Porosity takes values in between 0 and 1, $0 \leq \phi \leq 1$, and varies in a wide range depending on the material. For example, porosity of the common granite is found to be as low as $\phi \approx 0.01$, while porosity of sands lies in between $0.25 \leq \phi \leq 0.50$, the clay porosity was found in between $0.40 \leq \phi \leq 0.70$, and clothing and paper-like materials have porosity values up to $\phi \approx 0.87$ (Dimri et al. 2012; Freeze 1979; Rasi 2013). A list of typical porosity values can be found in the following table.

Material type	Porosity
Unconsolidated deposits	
Clay	0.40 - 0.70
Gravel	0.25 - 0.40
Sand	0.25 - 0.50
Silt	0.35 - 0.50
Rocks	
Dense crystalline rock	0.00 - 0.05
Fractured basalt	0.05 - 0.50
Fractured crystalline rock	0.00 - 0.10
Granite	< 0.01
Karst limestone	0.05 - 0.50
Limestone, dolomite	0.00 - 0.20
Paper	
Mechanical pulp	0.50 - 0.60
Filter paper	0.10 - 0.87

Table 1.1: Range of typical porosity values.

Porosity of porous media is closely related with another parameter, the liquid saturation of porous materials, s, which is defined as the ratio of the liquid volume V_L in a sample macroscopic volume element V to the volume of the available void space, that is

$$s = \frac{V_L}{V_v}.$$

Saturation is closely related with another parameter often used in the analysis of transport phenomena in porous materials, the total liquid content w, which is

$$w = \frac{V_L}{V} = \phi s.$$

Both parameters are informative, but we mostly use saturation as a variable in the study. So, the saturation, which is, as well as porosity, a non-dimensional parameter, takes also the values in between 0 and 1, $0 \leq s \leq 1$. Saturation indicates how the empty space available to the liquid flow is filled in with the liquid. If $s < 1$, this implies that there is some void space still available for the liquid. While at $s = 1$, the porous media can not absorb any more liquid and is called fully saturated. **Note,** the low saturation regime, which is the subject of the study, takes place at $s \leq s_c \approx 0.1$.

In defining parameters of porosity and saturation, we have used representative sample volume element V, which is assumed to be 'macroscopic'. 'Macroscopic' in the context of porous media studies does not imply that we are only ignoring molecular structure of the material. Averaging procedures required to obtain meaningful information in porous media dynamics are applied on different resolution levels all of them being much larger than the molecular and/or atomic time and length scales. Effectively, as we will discuss this further, this implies that the sample element is used to obtain average quantities, so that it should be large enough to guarantee that the properties and the parameters of the porous media will not depend anymore on the size of the volume element with some reservations, as we would like at the same time to describe variations of average properties. That is, if we increase the size of the sample volume element V, say two times, and then calculate porosity and saturation, then we will find their values at the same level as it was at the twice smaller volume element size. So that, the sample volume element of the porous matrix should contain many 'microscopic' (in the context of the porous media studies at lower level of the description than the averaging was done) details of porous media, for example, many, a lot of grain particles in the case of ordinary sands. It is obvious that, if we take too small volume element, a too small part of the porous media, then porosity and hence saturation may evince strong deviations from the average. For example, if we consider a volume element of the size of a grain particle, then we may find that there is no void space available at all. At the same time, if we take too big volume element, then we may during the averaging procedure wash out essential details of average quantities variations. A good balance should be observed between the length scales involved in the processes and the size of the averaging volumes, V.

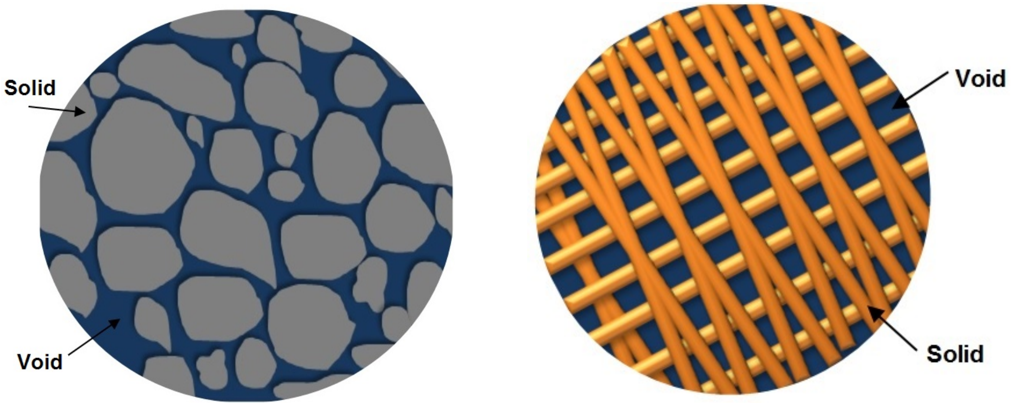

(a) Particulate porous media.

(b) Fibrous porous media.

Figure 1.1: Illustration of a sample volume element V in porous matrices: the solids/fibres are shown in grey/orange and the voids are designated by the blue colour.

While porosity and saturation are very informative non-dimensional parameters, strictly speaking, their knowledge is insufficient to describe liquid dispersion. Porosity does affect transport processes, but only indirectly. There is another important parameter, which is directly related with transport properties of porous media matrices - **permeability** of the porous materials.

1.1.2 Darcy's Law and Permeability

To understand the notion of permeability in porous materials, we consider the macroscopic models used to describe macroscopic liquid fluxes in porous media. As one can imagine, as we have already briefly discussed, the structure of porous materials is very complex. If we dig a small hole in the ground, one would see that even an ordinary soil consists of different granular particles mixed with complex organic material. Under high magnification of a microscope, the structure of ordinary papers or drapery looks like a jungle. Obviously, any practical description of this kind of complex systems should include some kind of averaging procedure to concentrate on essential, average properties and related parameters. We have already introduced two essential averaged parameters, porosity ϕ and saturation s characterising available void space and its filling with the liquid. Now, we turn our attention to the average description of liquid flows in porous matrices.

An indication of the possibility of such an average approach, in general, was the discovery of an empirical law relating liquid flux in porous media with the gradient of pressure, the Darcy's law formulated by a French engineer, Henry Darcy in 1856 (Brown 2002). Originally, the Darcy's law was an empirical relationship formulated on the basis of experimental observations in fully saturated porous media, which now-days takes a standard form assuming standard conditions under the action of the gravity force along the z-direction

$$\mathbf{q} = -\frac{\kappa}{\mu}\nabla(p + \rho g_0 z). \tag{1.1}$$

Here, $g_0 = 9.80665\,\mathrm{m/s^2}$ is the standard acceleration due to gravity on the Earth surface, ρ is the liquid density, μ is the liquid viscosity, p is the pressure in the liquid, $\mathbf{q}$ is the volumetric liquid flux density with dimensions $[q] = \frac{\mathrm{m}}{\mathrm{s}}$ and κ is the coefficient of permeability of the porous media with dimensions $[\kappa] = \mathrm{m}^2$. In the original formulation, the coefficient of permeability was assumed and experimentally found in homogeneous conditions to be a constant only depending on the nature of the porous materials. For example, permeability of common granite was found between $10^{-18}\,\mathrm{m}^2$ and $10^{-19}\,\mathrm{m}^2$ and permeability of sand between $10^{-12}\,\mathrm{m}^2$ and $10^{-15}\,\mathrm{m}^2$ (Bear 2013). A list of typical permeability values can be found in Table 1.2.

Material type	Coefficient of permeability (m^2)
Unconsolidated sand and gravel	
Clean gravel	$10^{-7} - 10^{-8}$
Clean sand or sand and gravel	$10^{-9} - 10^{-11}$
Very fine sand, silt, loess, loam	$10^{-12} - 10^{-15}$
Unconsolidated clay and organic	
Peat	$10^{-11} - 10^{-12}$
Layered clay	$10^{-13} - 10^{-15}$
Unweathered clay	$10^{-16} - 10^{-19}$
Consolidated rocks	
Oil rocks	$10^{-11} - 10^{-13}$
Sandstone	$10^{-14} - 10^{-15}$
Fresh limestone, dolomite	$10^{-16} - 10^{-17}$
Granite	$10^{-18} - 10^{-19}$

Table 1.2: Range of the typical coefficients of permeability in saturated regime of spreading.

In heterogeneous porous media, both porosity and permeability will be, obviously, functions of spatial coordinates, that is the points of observations. This is possible, if the averaging description is balanced, that is the averaging length scale (the size of the sample volume element V) is chosen properly to allow for slow variations of the porous media parameters.

If the liquid in the porous media is incompressible, as is practically always the case, in fully saturated regime assuming constant porosity

$$\nabla \cdot \mathbf{q} = \mathbf{0}. \tag{1.2}$$

The Darcy's law (1.1) then takes the form, which can be used in mathematical analysis

$$\nabla \cdot \left(\frac{\kappa}{\mu} \nabla (p + \rho g_0 z) \right) = 0. \tag{1.3}$$

In a one-dimensional case (along the z-axis), equation (1.3) represents a second order ordinary differential equation for pressure p, which can be integrated assuming constant liquid viscosity $\mu = const$ to obtain

$$\frac{dp}{dz} + \rho g_0 = C_0 \kappa^{-1}, \tag{1.4}$$

which can be further integrated to obtain distribution of pressure in the domain

$$p + \rho g_0 z = C_1 + C_0 \int_{z_1}^{z} \kappa^{-1} \, d\xi, \tag{1.5}$$

and via (1.1) distribution of the volumetric flux density q. Two free parameters C_0 and C_1 can be determined with the help of two boundary conditions, usually two values of pressure known at some points at the domain boundaries.

In a two- or a three-dimensional case, equation (1.3) belongs to the well-studied class of generalised Laplace equations, the Poisson's equation. It also requires certain types of the boundary conditions to obtain a unique solution (Evans 2010; Jost 2007). So, mathematically, the problem of defining the flow in fully saturated porous media is well defined and studied, and can be used in applications if the coefficient of permeability κ is known.

The situation becomes more complex in the case of unsaturated regimes of liquid dispersion.

1.2 Unsaturated Regime of Liquid Dispersion

Later on, the empirical Darcy's law has been derived using averaging techniques and generalised to the case of unsaturated regimes of liquid spreading, when the coefficient of permeability $\kappa = \kappa(s)$ becomes a function of the saturation s (Bear and Verruijt 1987, 2012; Koorevaar et al. 1983; Whitaker 1969).

Despite the fact that the Darcy's law is still in the form similar to that in equation (1.3)

$$\mathbf{q} = -\frac{\kappa(s)}{\mu}\nabla(p + \rho g_0 z) \tag{1.6}$$

with $\kappa = \kappa(s)$ and $s = s(z, t)$ the problem becomes mathematically slightly different. The incompressibility condition (1.2) is no longer fulfilled and instead, the mass conservation law should be used in full, so that the liquid content becomes a function of time and the point of observation. That is

$$\frac{\partial(\phi s)}{\partial t} + \nabla \cdot \mathbf{q} = 0. \tag{1.7}$$

If we designate $p + \rho g_0 z = H$, which is known as the 'head' in the literature (Koorevaar et al. 1983), then using (1.6) and (1.7), one arrives at

$$\frac{\partial(\phi s)}{\partial t} = \nabla \cdot \left(\frac{\kappa(s)}{\mu} \nabla H \right), \tag{1.8}$$

which can be also presented as

$$\frac{\partial(\phi s)}{\partial t} = \nabla \cdot (D \nabla s), \tag{1.9}$$

where

$$D(s) = \frac{\kappa(s)}{\mu} \frac{\partial H}{\partial s}$$

is the coefficient of non-linear diffusion or diffusivity.

Obviously, the new dependent variable is now saturation s, and one requires two additional relationships to complete the problem formulation. Namely, $H = H(s)$ and $\kappa = \kappa(s)$ have to be known. As a result, instead of a **linear** boundary value problem for a modified Laplace equation, we are facing analysis of a **non-linear** partial differential equation, a non-linear diffusion equation.

Non-linear diffusion equations have been studied mathematically in relation to different applications in biology, surface science and hydrology (Vázquez 2006) and (Vázquez 2007). They possess a constellation of properties, which are cardinally different from those of a linear diffusion equation. In particular, non-linear diffusion equations have a class of self-similar solutions with **compact** support and a boundary moving at finite speed (Barenblatt 2003; Vázquez 2014) and (Barenblatt 2014). The boundedness of the propagation velocity is characteristic of non-linear diffusion, since in linear diffusion processes the propagation is instantaneous.

1.2.1 Linear and Non-linear Diffusion

To understand main differences inherent in non-linear diffusion problems, consider a particular example of the so called porous medium equation (PME) in a one-dimensional case. Namely,

$$\frac{\partial u}{\partial t} = \frac{\partial}{\partial x}\left(u^m \frac{\partial u}{\partial x}\right), \quad t > 0, \quad m > 0, \quad x \in \mathbb{R}, \tag{1.10}$$

where t is time and x is the spatial coordinate.

To find a particular solution, let's first observe that the equation is invariant under the transformation

$$\begin{aligned} t &\to \epsilon t, \\ u &\to \epsilon^q u, \\ x &\to \epsilon^r x, \end{aligned} \tag{1.11}$$

where $\epsilon > 0$ is some real positive constant and q, r are some real constants.

Indeed, if we introduce new variables $\bar{t} = \epsilon t$, $\bar{u} = \epsilon^q u$, $\bar{x} = \epsilon^r x$ and substitute them into (1.10), then

$$\frac{\partial \bar{u}}{\partial \bar{t}} = \epsilon^{-qm+2r-1} \frac{\partial}{\partial \bar{x}} \left\{ \bar{u}^m \frac{\partial \bar{u}}{\partial \bar{x}} \right\}. \tag{1.12}$$

That is, when

$$2r - qm - 1 = 0 \tag{1.13}$$

we end up with exactly the same equation as that before the transformation.

Condition (1.13) is sufficient, and there is still freedom to choose one of the two parameters q or r.

Following the invariance property and introducing new variables

$$w(y) = \frac{u}{t^q}, \quad y = \frac{x}{t^r},$$

one can obtain a self-similar solution of one independent variable y choosing $r = -q$, that is $q = -1/(2+m)$,

$$w(y) = \left\{ C_1 - \frac{my^2}{2(2+m)} \right\}^{1/m}.$$

One constant of integration has been determined according to the symmetry condition

$$\left.\frac{dw}{dy}\right|_{y=0} = 0$$

assuming that the solution is bounded. One can immediately see that the solution has naturally compact support. Indeed, $w = 0$ at $y = y_0 = \pm\sqrt{\frac{2C_1(2+m)}{m}}$.

Returning to the original variables t, $x = yt^r$ and $u = wt^q$, one can see that

$$u(x,t) = t^{-\frac{1}{2+m}} \left\{ C_1 - \frac{mx^2}{2(2+m)t^{\frac{2}{2+m}}} \right\}^{1/m}.$$

Illustration of these self-similar solutions is shown in Fig.B.1 where the boundaries of the compact support $x_b(t)$ are moving with finite velocity as $x_b = \pm t^{\frac{1}{2+m}}|y_0|$.

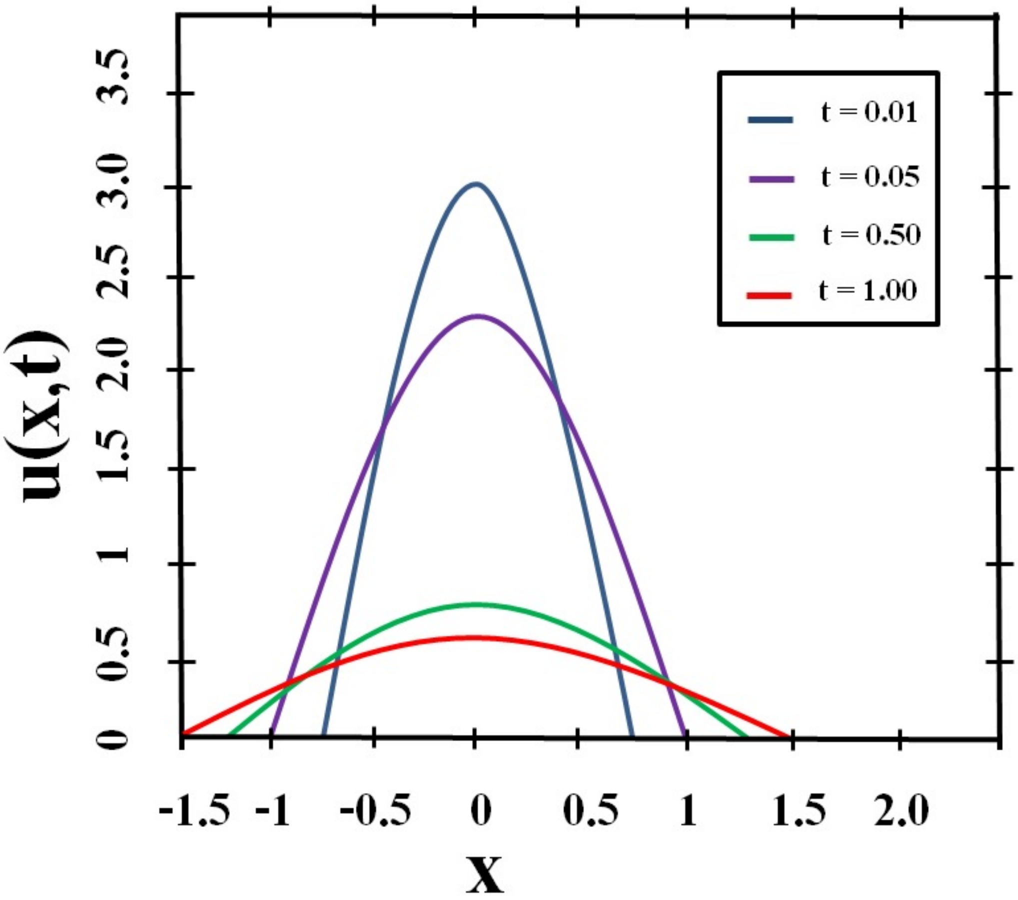

Figure 1.2: Illustration of the self-similar solutions $u(x,t)$ to the PME (1.10) at $m = 2$ and at different moments of observation $t > 0$.

In the case of the linear diffusion, analogous invariance arguments (at $m = 0$) give rise to the well-known self-similar solution obtained in an instantaneous (at $t = 0$) symmetric injection problem

$$u(x,t) = \frac{C}{\sqrt{4\pi t}} \exp\left(-\frac{x^2}{4t}\right),$$

which has no compact support and therefore has infinite propagation rate of the solution. So, contrary to our experience with the linear diffusion equation, nonlinear diffusion problems have a clearly defined moving boundary.

1.2.2 Macroscopic Models of Liquid Dispersion in Soils

In relation to mathematical simulations of unsaturated transport in soils, the permeability coefficient demonstrates very large variations as a function of saturation - by five-six orders of magnitude in the range $0.1 \leq s \leq 1$. Roughly, coefficient of permeability behaves as $\log_{10} \kappa \propto s$ in that range (Koorevaar et al. 1983).

There are no general analytical expressions available for $\kappa(s)$ and $H(s)$. Instead, several empirical models have been developed on the basis of numerous experimental observations, see, for example, (Millington and Quirk 1961; Mualem 1976; Van Genuchten 1980).

In the practical range of saturations $0.1 \leq s \leq 1$, the Van Genuchten model is the most popular, widely used and tabulated providing values of permeability coefficients $\kappa(s)$ and retention curves, that is $H = H(s)$ dependencies as functions of saturation s for practically every soil found on this planet (Montzka et al. 2017).

This would be instructive to consider a one-dimensional (in the x-direction), steady state problem associated with (1.9) assuming a general relationships $D(s)$. If the flux density is fixed and known, that is $q = q_0 = const$, then

$$q_0 = -D(s)\frac{ds}{dx}. \tag{1.14}$$

Hence, measuring $s(x)$ in an interval $s \in [s_1, s_2]$ one can deduce coefficient of diffusivity $D(s)$ as a function of saturation. As an example, consider PME with $m = 2$, that is $D(s) = s^2$. Integrating (1.14), one can get implicitly

$$s^3(x) = C - 3q_0x,$$

where the free constant C can be fixed by setting a certain value of saturation at some point in the domain. Therefore, if we consider the data $s = s(x)$, the dependence of the derivative on s (that is, in practice, plotting a graph of ds/dx as a function of s and finding a reasonable fit to the dependence)

$$\frac{ds}{dx} = -s^{-2}q_0,$$

can be recovered. Note, that instead of fixing the flux value, one can consider a boundary value problem fixing the value of saturation at the end points (the boundary) of the domain.

We will use this one-dimensional set-up later in the analysis of transport in fibrous materials, Chapter 2, to recover unknown coefficients of diffusivity. Here we mention that the analysis of transport in porous media has one complication, which is the effect of hysteresis observed in the dependence of the head $H = H(s)$ on s, (Koorevaar et al. 1983; Leverett et al. 1941; Mualem 1974).

The hysteresis phenomenon is closely related with the distribution of the pores with different sizes and the capillary pressure developed in them. In the next part, we consider the notion of capillary pressure, which plays a central role in the mechanism of liquid spreading in porous materials.

1.2.3 Retention Curves and Capillary Pressure

1.2.3.1 Surface Tension

Capillary pressure in liquids is generated due to the surface tension effect. In macroscopic approximation, surface tension manifests itself through the work done to change surface area without varying other thermodynamic parameters such as volume and temperature. For example, if initially spherical liquid drop is disturbed, so that its surface area is increased by ΔS, then at constant temperature and constant volume of the drop, the necessary amount of work ΔW to facilitate such a change is given by

$$\Delta W = \gamma \Delta S$$

where γ is known as the coefficient of surface tension (Miller and Neogi 2007; Shikhmurzaev 2007).

Physically, at the nanoscale, the origin of this effect is due to uncompensated inter-molecular forces at the interface. In the bulk of the liquid, the molecular forces are balanced at equilibrium, while at the interface, typically at the distance of a couple of nanometres, there is a strong net force acting on the particles in the perpendicular to the interface direction. At the free surface, the force is directed inwards the liquid bulk area, so that the effect of the surface tension tends to decrease the surface area. At liquid-solid interfaces, the direction is typically the opposite one, so that the surface area tends to increase - the effect known as the wetting of solid surfaces.

1.2.3.2 Surface Tension and Contact Angle

In another way, the wetting phenomena are described by the contact angle θ_c between the free surface of the liquid and the solid-liquid interface at the point of contact - the contact line, which is a function of surface tensions. The contact angle and the surface tensions are related by the Young equation, that is

$$\gamma \cos\theta_c = -\gamma_{LS} + \gamma_{GS},$$

where γ is the liquid-gas surface tension, γ_{LS} is the surface tension of the liquid-solid interface and γ_{GS} is the surface tension of the gas-solid interface at equilibrium (Miller and Neogi 2007; Shikhmurzaev 2007).

The value of the contact angle is informative and indicative of either wetting or non-wetting liquid-solid combinations. If $-\gamma_{LS} + \gamma_{GS} - \gamma > 0$ then $\theta_c = 0$, and a liquid drop placed on a solid substrate will eventually spread into a thin film. This regime is called complete wetting, that is the liquid wets available solid surface. When $0 < \theta_c < \pi/2$, the regime is called partial wetting, and above the critical value $\theta_c = \pi/2$, we are dealing with a non-wetting case. In these two cases, the liquid surface has a shape of a liquid drop, wetting partially the substrate.

1.2.3.3 Surface Tension and Capillary Pressure

If the liquid-gas interface is curved, the interface curvature creates a pressure difference Δp known as the Laplace pressure, which is given by

$$\Delta p = p_{in} - p_{out} = \gamma \left\{ \frac{1}{R_1} + \frac{1}{R_2} \right\} = \gamma \kappa_R. \tag{1.15}$$

Here, R_1 and R_2 are the principal radii of the surface at the point of observation, so that κ_R is the mean curvature of the interface. If the surface tension and the curvature are both positive, as is the case for liquid-gas interfaces ($\gamma > 0$) and spherical drops $\kappa_R > 0$, $p_{in} > p_{out}$. In the case of a meniscus in a cylindrical capillary, the curvature is negative in the wetting case, and therefore the pressure drop is also negative and serves as a **driving force** sucking the liquid into the capillary tubes. This wetting phenomenon is also the **driving force** of the liquid spreading in porous materials.

If the pore size is small, this can create relatively strong pressure. For example, in the case of water ($\gamma = 72.8\,\mathrm{mN/m}$ at the room temperature), $\Delta p \approx 1.4\,\mathrm{atm}$ at $R_1 = R_2 = 1\,\mu\mathrm{m}$ and $\Delta p \approx 144\,\mathrm{atm}$ at $R_1 = R_2 = 10\,\mathrm{nm}$. Therefore, if the amount of the available liquid is limited, as is the case in the unsaturated regime, the smaller pores or geometric structures possessing smaller length scale would always eventually win over the large geometry in the competition for the liquid during the spreading. On the other hand, resistance to the flow is larger in small capillaries.

These two effects, roughly speaking, lead to the origin of the hysteresis effect in porous materials during drainage and imbibition cycles. When the liquid is spreading through a dry material during imbibition, small pores can take part in creating the capillary pressure, on the other hand during drainage, small pores are already filled in and the pressure is defined by the larger length scale available. That is, the retention curves or capillary pressure - saturation relationships $H = H(s)$ are not single valued functions, but can have two or more brunches corresponding to imbibition and drainage phases of the wetting cycles, so that at the same level of saturation, capillary pressure may be different depending on the history of the processes involved.

1.3 Macroscopic Model of Liquid Dispersion at Low Saturation

The mathematical models developed in soil science and hydrology to describe liquid transport in unsaturated porous media are usually bounded from below by relatively high lower bounds, just about $s \approx s_c \approx 10\%$ or so. The lower limits of applicability of the models were partially dictated by the practical needs and, on the other hand, by the strong reduction of permeability at low saturation levels making direct experimental observations of the spreading phenomena difficult unless very persistent liquids were used. As a result, the dynamic phenomena in the low saturation region remained practically unexplored till recently (Lukyanov et al. 2012).

What happens exactly, when the saturation level drops down to $s_c \approx 10\%$ and below that critical level? As an example, we consider the process in **particulate porous media** like ordinary sand, Fig. 1.1, which has been studied experimentally and theoretically in (Lukyanov et al. 2012).

When the saturation levels reach $\approx 30\%$ from above, a percolation transition occurs when the largest cluster containing about 90% of the available liquid breaks down into complex structures formed around solid particles, such as trimers and pentamers, and the global connectivity of the liquid volumes disappears (Herminghaus 2005; Scheel et al. 2008a,b). With a further decrease of the saturation levels, at $s \approx s_c \approx 10\%$ all liquid is concentrated in the liquid bridges, so called **pendular rings,** formed at the points of particle contacts, Fig. 1.3, and in the grooves on the rough surfaces of the constituent particles. In literature, this liquid morphology is called the **pendular regime** of wetting.

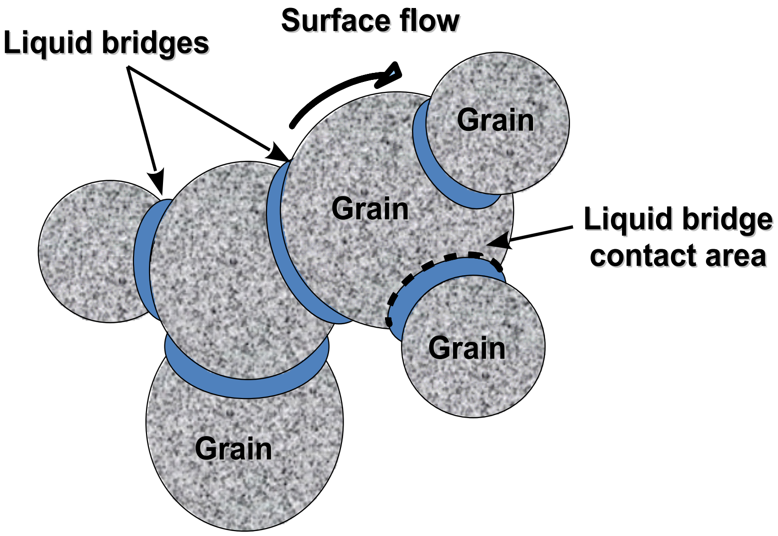

Figure 1.3: Illustration of the pendular rings - the liquid morphology at low saturation levels $s < 10\%$.

The formation of isolated liquid bridges, **pendular rings**, is the main characteristic feature of the pendular regime of wetting, when liquid volumes inside the porous matrix are only connected via liquid layers developed on rough surfaces of the particles, Fig. 1.3. The pendular regime of wetting in static and dynamic conditions was observed in experiments and computer simulations in a range of saturations $0.2\% \leq s \leq 10\%$ (Denoth 1999; Herminghaus 2005; Lukyanov et al. 2012; Melnikov et al. 2015, 2016; Scheel et al. 2008a,b).

Obviously, there exists clear separation of the length scales in the pendular wetting states. There are two characteristic length scales in the problem: the length scale related with the size of the particles, sand grains for example, that is their average radius R, which is also the length scale of the pendular rings, and a length scale associated with surface roughness δ_R. The surface roughness in sands has been studied in detail providing us with characteristic values involved (Alshibli and Alsaleh 2004). In typical sands, $100\,\mu\mathrm{m} < R < 800\,\mu\mathrm{m}$, while δ_R lies in a range of a few micrometers or even less $250\,\mathrm{nm} < \delta_R < 3\,\mu\mathrm{m}$, so that $\delta_R \ll R$ is always fulfilled. As a result, when the wetting front is moving into a dry porous area, the capillary pressure is mostly generated on the length scale of the surface roughness. The capillary pressure due to the surface roughness is the main driving force of the wetting in dry porous materials, while the pendular rings serve as variable-volume reservoirs.

In what follows, we consider formulation of a macroscopic model of liquid dispersion at low saturation values. In a similar way, as the macroscopic transport model was formulated in general in unsaturated regime, one requires the same main ingredients here, that is permeability coefficients and capillary pressure (or head) dependencies on the value of saturation. In the next part, we consider pressure-saturation relationships, that is the liquid morphology of the pendular rings and in the surface roughness grooves.

1.3.1 Morphology of Liquid Distributions at Low Saturation Levels and Capillary Pressure

The critical value of saturation s_c marks the beginning of the pendular regime of wetting when the liquid is contained only in the bridges formed at the points of particle contacts and on the rough surface of the particles themselves. As an approximation, we consider spherical (or nearly spherical) particles.

1.3.1.1 Liquid Distribution in Surface Roughness Grooves

The high negative capillary pressure generated by the surface irregularities of the smallest length scale $\approx 250\,\mathrm{nm}$ can be only observed at the moving front, basically within the layer of one particle diameter thick. In the bulk of the wet area, the capillary pressure is distributed, having much lower negative values. As a result, in the surface roughness grooves, the interface is expected to be mostly flat, that is its curvature $\kappa_R \ll \delta_R^{-1}$. Basically, the grooves can be assumed to be fully filled in due to the pinning of the contact line to the groove edges, as is shown in Fig. 1.4. Therefore, the liquid content in the surface roughness can be assumed in the first approximation to be constant.

To estimate the contribution made by the liquid contained within the surface roughness layer, consider an ensemble of identical spherical particles of radius R with the surface roughness layer described by only one parameter δ_R, its characteristic thickness. In any sample volume V, the total volume of the surface layers of thickness δ_R is

$$V_R = 3(1-\phi)V\frac{\delta_R}{R},$$

where ϕ is porosity.

Considering that only some part of the surface layer can be occupied by the liquid, the total liquid content due to the surface roughness is

$$V_R^L = 3\alpha_R(1-\phi)V\frac{\delta_R}{R}$$

where parameter $0 < \alpha_R < 0.5$ is the fraction of the surface (roughness) volume occupied by the liquid. Therefore, saturation due to the liquid in the surface layer s_0 (as if no pendular rings exist in the system) can be represented by

$$s_0 = 3\alpha_R\frac{(1-\phi)}{\phi}\frac{\delta_R}{R}. \tag{1.16}$$

Taking typical values $R = 500\,\mu\text{m}$, $\delta_R = 1\,\mu\text{m}$, $\phi = 0.3$ and $\alpha_r = 0.25$, one gets $s_0 \approx 0.35\%$. This implies that only at very small saturation levels the surface liquid content starts to contribute substantially.

1.3.1.2 Liquid Distribution in the Pendular Rings

We have estimated that liquid content due to the surface roughness in particulate porous media can be considered to be constant (independent of pressure) and contributes about $s_0 \approx 0.35\%$ in terms of saturation. The pendular rings, on the other hand, due to much larger length scale involved should demonstrate variations in the liquid content as pressure varies in the system.

Consider two spherical particles in contact, Fig. 1.5. The configuration of a liquid-gas interface at rest is described by the Young-Laplace equation, which relates the hydrostatic pressure difference across the interface to the local mean curvature κ_R and surface tension γ of the liquid. When the Bond number is small, that is $Bo = \frac{\rho g R^2}{\gamma} \ll 1$, where g is acceleration of gravity, ρ is liquid density and γ is the surface tension, the effects of gravity are negligible and the capillary pressure p and the mean curvature are practically uniform.

In general, the problem of determination of the shape of a constant-curvature surface is quite difficult and provides little opportunity to find analytical solutions. The analysis is much easier if the problem has some symmetry, for example in an axisymmetric case. In such a situation, using the setup in Fig. 1.5, the free surface profile $z = z(x)$ (of constant curvature) satisfies the Young-Laplace equation

$$2\kappa_R = \frac{d^2 z}{dx^2}\left(1+\left(\frac{dz}{dx}\right)^2\right)^{-3/2} + \frac{dz}{dx}\frac{1}{x}\left(1+\left(\frac{dz}{dx}\right)^2\right)^{-1/2} = const = \frac{p}{\gamma}. \quad (1.17)$$

The equation should be augmented with two boundary conditions, the contact angles θ_1 and θ_2 the interface makes with the solid surface of the particle and at the mid-plane between two particles (Orr et al. 1975). The particular case of two identical particles separated by distance $2D$ can be recovered at $\theta_2 = \pi/2$. Analytical expressions relating geometric properties of the surface, such as curvature, with the model parameters and the bridge size (angle ψ in Fig. 1.5) even in this simplified case were found to be very bulky. For example, in the case of negative capillary pressure, when the uniform-curvature interface has a shape of a nodoid, the non-dimensional mean curvature has an implicit form (Orr et al. 1975)

$$2\kappa_R R = A_1\left[A_2 - \phi_k^{-1}(E(\phi_2,\phi_k) - E(\phi_1,\phi_k)) + \frac{1-\phi_k^2}{\phi_k}(F(\phi_2,\phi_k) - F(\phi_1,\phi_k))\right]$$

where $A_1 = \frac{1}{D/R+1-\cos\psi}$, $A_2 = -\cos(\theta_1+\psi) - \cos\theta_2$, $\phi_1 = \pi/2 - \theta_1 - \psi$, $\phi_2 = \theta_2 - \pi/2$, $\phi_k = (1+c_k)^{-1/2}$, $c_k = 4\kappa_R^2 R^2 \sin^2\psi - 4\kappa_R R \sin\psi \sin(\theta_1+\psi)$ and F, E are incomplete elliptic integrals of the first and second kinds respectively (Abramowitz and Stegun 1970). Nevertheless, despite the apparent complexity of the analytical expressions, the capillary pressure dependence on the volume of the ring V_B (per particle) can be approximated at zero separation distance $D = 0$ and small contact angles θ_c with good accuracy, Fig. 1.6, as

$$p \approx p_0 \left\{ C_0 - C_1 \left(\frac{R^3}{V_B} \right)^{1/2} \right\}$$

where $C_0 = 3.7$, $C_1 = 1.3$, $p_0 = \frac{2\gamma}{R}\cos\theta_c$.

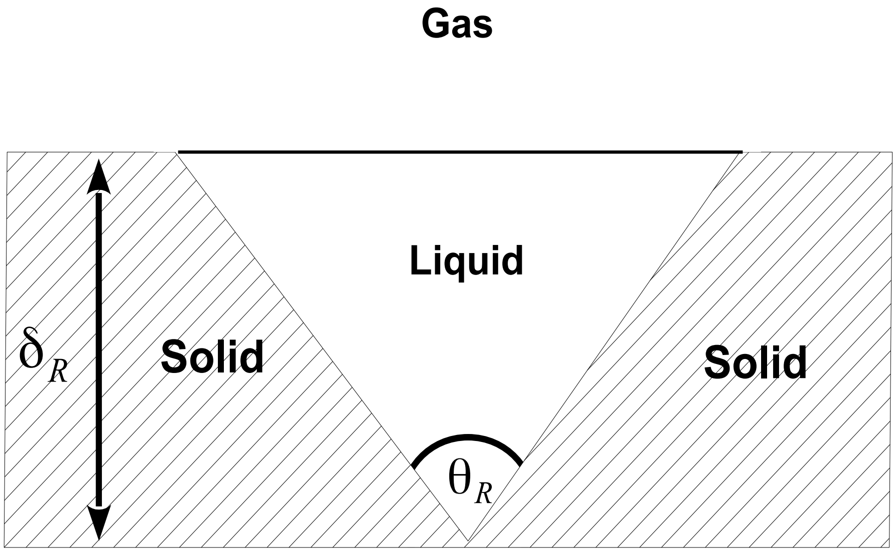

Figure 1.4: Illustration of the liquid morphology at low saturation levels $s < 10\%$ in the surface roughness grooves.

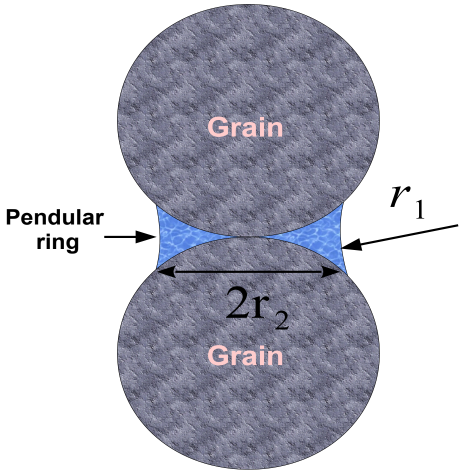

(a) Pendular ring between two particles.

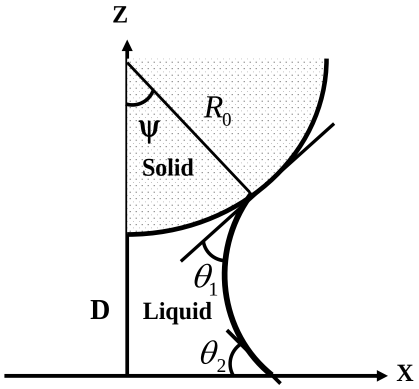

(b) Setup to obtain pressure-volume dependence.

Figure 1.5: Illustration of a pendular ring morphology setup.

Since in the pendular regime $s \ll 1$, that is $V_B R^{-3} \ll 1$, the pressure-saturation relationship can be further reduced to

$$p \approx -p_0 C_1 \left(\frac{R^3}{V_B}\right)^{1/2}. \tag{1.18}$$

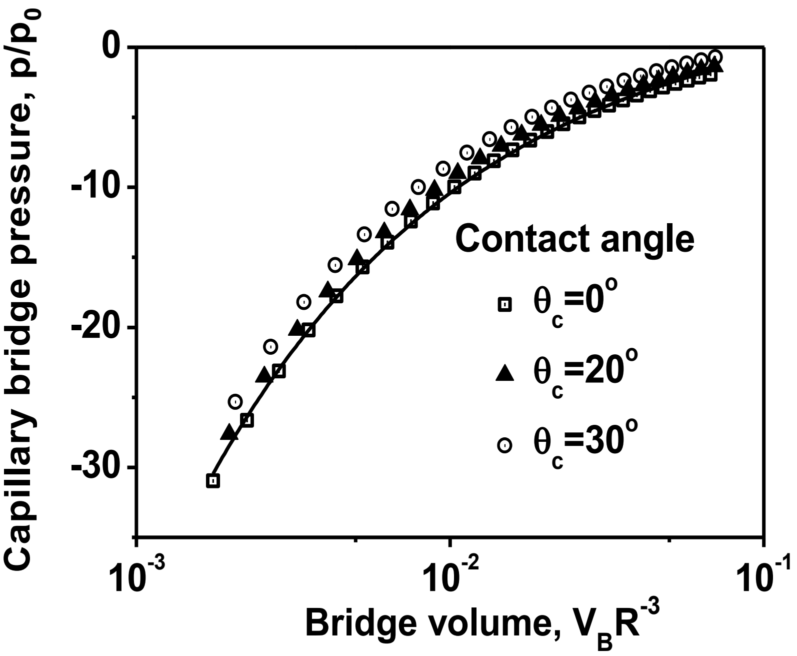

Figure 1.6: Reduced capillary bridge pressure p/p_0 in the case of two identical solid spheres in contact (zero separation distance $D = 0$) as a function of the reduced bridge volume V_B/R^3 at different contact angles θ_c. Symbols indicate exact solutions from (Orr et al. 1975) and the solid line is the fit $p/p_0 = C_0 - C_1(V_B R^{-3})^{-1/2}$ at $C_0 = 3.7, C_1 = 1.3$.

To express pressure-saturation law (1.18) in terms of saturation s, one can calculate the liquid content in sample volume element V containing many grain particles $N \gg 1$. Using similar procedure as that to get (1.16), one gets

$$s = s_0 + \frac{3}{4}\frac{1-\phi}{\phi}\frac{N_c}{\pi}\frac{\langle V_B\rangle^l}{R^3}, \tag{1.19}$$

where N_c is the coordination number, that is the average number of bridges per a particle, $\langle V_B \rangle^l$ is the average bridge volume, $\langle \ldots \rangle^l = V_l^{-1} \int_{V_l} ... d^3x$ is intrinsic liquid averaging (Whitaker 1969), V_l is liquid volume within the sample volume V. In experiments (Lukyanov et al. 2012), it has been found that $N_c \approx 7$.

Treating the bridge volume V_B as an average, using (1.18) and (1.19), the average capillary bridge pressure $P = \langle p \rangle^l$ in the volume element V can be presented as

$$P = -p_0 \frac{A_c}{(s - s_0)^{1/2}}, \quad A_c = C_1 \sqrt{\frac{3}{4} \frac{1 - \phi}{\phi} \frac{N_c}{\pi}}. \tag{1.20}$$

This would be instructive here to consider some simplified relations between the geometry of the liquid bridge and the capillary pressure (Herminghaus 2005; Willett et al. 2000), Fig. 1.5. When $V_B R^{-3} \ll 1$, the pressure is defined by the smallest radius of curvature r_1, Fig. 1.5, $p \approx -\gamma \cos \theta_c / r_1$, which is related with the second radius

$$r_1 \approx r_2^2 / 2R, \tag{1.21}$$

so that when $s \ll 1$, one has $r_2 \gg r_1$. One should note also that, r_2 defines the size of the area covered by the bridge.

If we have two particles of different radii, say R_1 and R_2, in contact, the size of the bridge area will be approximately the same $r_2^{(1)} \approx r_2^{(2)}$ at low saturation levels, $s \ll 1$ with the difference being proportional to r_1, that is

$$\frac{r_2^{(1)} - r_2^{(2)}}{\max(R_1, R_2)} = O\left(\frac{r_1}{\max(R_1, R_2)} \right). \tag{1.22}$$

1.3.2 Surface Diffusion and Microscopic Model

Consider now the local transport on the surface of particles, which is described by the average surface flux density $\mathbf{q}$. The quantity is defined by averaging the volumetric flux over a sample cross-section area of width δ_R containing many grooves and including areas of both solid and liquid. According to a study of liquid spreading on rough surfaces made of microscopic grooves of various shapes and dimensions (Or and Tuller 2000; Ransohoff and Radke 1988; Romero and Yost 1996; Rye et al. 1998), the flow on average obeys a Darcy-like law

$$\mathbf{q} = -\frac{\kappa_m}{\mu} \nabla \psi, \tag{1.23}$$

where μ is liquid viscosity, ψ is the averaged pressure within the surface roughness and κ_m is the effective coefficient of permeability, which is proportional to δ_R^2.

The fact that the local liquid dispersion on the surface of particulate elements can be described by the Darcy's law is important. In the approximation of constant liquid content in the surface layer

$$\nabla \cdot \mathbf{q} = 0,$$

and the local pressure obeys the Laplace-Beltrami equation defined on the surface Ω of the porous media elements

$$\Delta_\Omega \, \psi = 0. \tag{1.24}$$

This implies that, the analysis of the Laplace-Beltrami problem can serve to provide information about permeability of complex surface structures. This problem will be considered in Chapters 3-6 of the thesis.

Now, using the obtained pressure-saturation relationship and the local Darcy's law, one can formulate a macroscopic model of the liquid dispersion at low saturation levels.

1.3.3 Macroscopic Model

According to the spatial averaging theorem (Whitaker 1969), applying intrinsic liquid averaging $\langle \dots \rangle^l = V_l^{-1} \int_{V_l} \dots \, d^3x$ to (1.23),

$$-\frac{\kappa_m}{\mu}\left\{\nabla\langle\psi\rangle^l + V_l^{-1}\int_{S_l}\psi\,\mathbf{n}\,dS\right\} = \langle\mathbf{q}\rangle^l, \tag{1.25}$$

where S_l is the area of the liquid interface confined inside the volume element V and with normal vector $\mathbf{n}$. The surface integral in the creeping flow conditions, when the pressure variations across the liquid layer are insignificant, can be neglected $V_l^{-1}\int_{S_l}\psi\,\mathbf{n}\,dS \approx 0$ and as a result

$$-\frac{\kappa_m}{\mu}\nabla\langle\psi\rangle^l = \langle\mathbf{q}\rangle^l. \tag{1.26}$$

Thus, one can cast the continuity equation,

$$\frac{\partial \phi s}{\partial t} + \nabla\cdot\mathbf{Q} = 0,$$

into

$$\frac{\partial \phi s}{\partial t} = \nabla\cdot\left\{\frac{K}{\mu}\nabla P\right\}. \tag{1.27}$$

Here,

$$\mathbf{Q} = \frac{S_e}{S} \langle \mathbf{q} \rangle^l, \tag{1.28}$$

S is the surface area of the sample volume V with the effective area of entrances and exits S_e and coefficient of permeability $K = \kappa_m \frac{S_e}{S}$. It is assumed that in creeping flow conditions $P = \langle p \rangle^l \approx \langle \psi \rangle^l$. Note, that the ratio S_e/S is not strictly speaking just a geometric factor. It is an average quantity defined by (1.28), which incorporates connectivity and the shape of the surface elements. A priori, one can expect that $S_e/S \approx \delta_R/R$, that is it is proportional to the surface layer cross-section.

Assuming further that porosity ϕ is constant and using expression (1.20) for the average pressure, one can transform the governing equation (1.27) into a non-linear diffusion equation for the saturation $s(\mathbf{x}, t)$

$$\frac{\partial s}{\partial t} = \nabla \cdot \left\{ \frac{D_s \nabla s}{(s - s_0)^{3/2}} \right\}, \quad t > 0 \tag{1.29}$$

where

$$D_s = \frac{1}{2} \frac{K}{\mu} \frac{p_0 A_c}{\phi},$$

and

$$A_c = C_1 \sqrt{\frac{3}{4} \frac{1 - \phi}{\phi} \frac{N_c}{\pi}}.$$

where N_c is the coordination number.

In the case of a moving boundary-value problem with a smooth boundary $\partial\Omega$ moving with velocity $\mathbf{v}$, the super-fast diffusion equation (1.29) should be augmented with boundary conditions at the moving front

$$s|_{\partial\Omega} = s_f \ , \ s_f > s_0$$

and

$$\mathbf{v} \cdot \mathbf{n}|_{\partial\Omega} = -D_0 \ \frac{\mathbf{n} \cdot \nabla s}{s_f(s_f - s_0)^{3/2}}.$$

where $\mathbf{n}$ is the normal vector to the boundary $\partial\Omega$ and s_f is the boundary value of the saturation which is defined by the capillary pressure developed at the moving front. Note that, the requirement $s_f > s_0$ is equivalent to assume that liquid bridges always exist in the domain of spreading. This has been confirmed by direct experimental observations (Lukyanov et al. 2012).

1.3.4 Super-Fast Non-Linear Diffusion

The non-linear diffusion equation (1.29) is known to belong to the super-fast non-linear diffusion class (Vázquez 2006) due to the presence of a singular term $(s - s_0)^{-3/2}$. This is a very distinctive and characteristic feature of the model, which appears as the result of the characteristic pressure-saturation relationship. The singularity is formal in our case, since according to the experimental evidence (Lukyanov et al. 2012), the pendular rings always exists in the domain of the liquid spreading, and hence

$$s > s_0$$

is always the case. While the divergence is formal, nevertheless, the singular character of the diffusivity coefficient $(s-s_0)^{-3/2}$ makes the diffusion process relatively fast when saturation levels are approaching the minimal value s_0. Otherwise, the diffusion process would be much slower considering that the permeability coefficient in ordinary sands or gravels at low saturation is expected to be about

$$K \propto \delta_R^2 \frac{\delta_R}{R} \approx 10^{-15} - 10^{-16}\,\mathrm{m}^2$$

according to the scaling of $S_e/S \approx \delta_R/R$. This is very low, practically on the level of the permeability coefficients of the compressed clay, limestone or dolomite in the fully saturated matrix, Table 1.2. Note, those materials are always regarded as waterproof in soil science and hydrology.

1.3.5 Super-Fast Non-Linear Diffusion and Self-Similarity

The moving boundary-value problem to (1.29) has compact support, so that it is tempting to determine self-similar solutions to that problem. But, this is not the case here. The super-fast diffusion model does not demonstrate this universal behaviour. While initial distributions of saturation evolve with time to a distinctive saturation profile (Lukyanov et al. 2012), there was no true self-similar behaviour identified so far. Indeed, consider a simplified non-dimensional version of (1.29) in a one-dimensional domain $\Omega \subset \mathbb{R}$ with the boundary $\partial\Omega$ moving with velocity v

$$\frac{\partial u}{\partial t} = \frac{\partial}{\partial x}\left\{ \frac{1}{(u+u_0)^{\frac{3}{2}}} \frac{\partial u}{\partial x} \right\}, \quad x \in \Omega, \;\; t > 0$$

with

$$u|_{\partial\Omega} = 0 \tag{1.30}$$

and

$$v|_{\partial\Omega} = -s_f^{-1} u_0^{-\frac{3}{2}} \frac{\partial u}{\partial x}\bigg|_{\partial\Omega}, \tag{1.31}$$

where $u = s - s_f$ and $u_0 = s_f - s_0$. Consider again the one-parameter group of transformations (1.11) of the variables $t \to \epsilon t$, $u \to \epsilon^q u$ and $x \to \epsilon^r x$, which was used to obtain self-similar solutions, in particular the Barenblatt self-similar distribution profiles; $\epsilon > 0$. One can immediately see that the moving boundary value problem is not invariant under the group of transformations, that is one can not determine such q and m at $u_0 \neq 0$ so that to obtain an invariant equation **with invariant boundary conditions.**

The only way to get some kind of self-similarity is to scale the boundary conditions accordingly, that is $\bar{s}_f = \epsilon^q s_f$ and $\bar{u}_0 = \epsilon^q u_0$. In this case, a self-similar solution can be found if

$$2r - 1 + \frac{3}{2}q = 0.$$

Then, a symmetric around $x = 0$ solution is given by

$$u(x,t) = \frac{1}{t^2} \frac{1}{\left\{C_1 + \frac{3}{2}\frac{x^2}{t^4}\right\}^{2/3}}, \quad t > 0$$

but, it is impossible to satisfy the boundary condition $u|_{\partial\Omega} = 0$.

1.3.6 Super-Fast Non-Linear Diffusion and Surface Permeability

Another essential element of the model, which has to be determined in practical applications of the model, is the coefficient of permeability $K = K(s)$, which is expected to be some function of saturation.

Previously, the super-fast diffusion model (1.29) has been validated against experiments using a simplifying assumption that $K = const$ (Lukyanov et al. 2012). The study has demonstrated sufficiently good comparison, though it was understood that any enhancement of the model predictive power can be only achieved if the permeability coefficient K as a function of the liquid content (saturation s) is determined. This is the main topic of this study. Obviously, the curved shape of the particles should affect the ability of those surfaces to conduct the flow. In what follows, we will first generalise the macroscopic description to the case of fibrous porous materials, where the permeability coefficient can be recovered using a relatively simple network model. Then, we will analyse mathematical problems related with the definition of the coefficient permeability K in particulate porous media.

1.4 Thesis Overview

In this thesis, we will consider several aspects of mathematical modelling liquid dispersion processes at low saturation levels. After an introduction in Chapter 1, in Chapter 2, we deal with the macroscopic description of the low saturation regime of spreading in fibrous porous materials using a mesoscopic network model. We demonstrate how the macroscopic properties of fibrous materials (common paper would be a good example) and the super-fast non-linear diffusion model, initially developed to describe liquid dispersion in particulate porous media, can be recovered on the basis of a mesoscopic network description.

In Chapter 3 and 4, we return to the mathematical description of liquid dispersion in particulate porous media and examine surface transport over a single constituent element of the porous matrix to estimate effective coefficient of permeability, which in turn appears in the macroscopic super-fast diffusion model. We demonstrate that the permeability coefficient of an element can be accurately determined on the basis of the analysis of the Laplace-Beltrami boundary value problem set on the curved surface of the element. We analyse weak formulation of the problem and its approximation via surface finite element techniques including error analysis using appropriate norms.

In Chapter 5, we examine the surface transport and the Laplace-Beltrami problem over a set of coupled elements.

Finally, in Chapter 6, we apply the developed technique and its finite element realisation to consider a representative ensemble of randomly packed interconnected particles. We summarise the analysis and demonstrate how the results can be directly used in practical estimations of the permeability coefficients of particulate porous media at low saturation levels. In Chapter 7, we briefly discuss how the results can be generalised and transferred to different settings.

The main results presented in Chapter 4 have been **published** in (Sirimark et al. 2018a,b). The results obtained in a randomly packed particle ensemble, Chapter 6, have been **submitted** to a journal (Sirimark et al. 2019).

Chapter 2

Capillary Transport in Fibrous Porous Materials at Low Levels of Saturation

The problem of capillary transport in particulate porous materials, such as sand, at low levels of saturation can be simulated using a macroscopic mathematical model, the superfast non-linear diffusion (Lukyanov et al., 2012). The mathematical model is based on several characteristic features of the phenomenon. First of all, in particulate porous media at low saturation levels, the liquid is concentrated in the pendular rings formed at the point of contact of the constituent particles. The pendular rings are the reservoirs bounded by a constant-curvature interface, which has a characteristic pressure-volume relationship. At the same time, the flow predominantly occurs over the surface elements of the particles characterised by a constant saturation level s_0. Apparently, such separation of the functional elements can occur in other types of porous media. In this chapter, we will study the process of diffusion in one of those system, the fibrous porous materials, like textile or paper.

The structure of fibrous porous materials is quite different from that of particulate porous media (Alava and Niskanen 1994; Eichhorn and Sampson 2005; Herminghaus 2005; Niskanen and Alava 1994a; Rasi 2013; Sampson 2003). Yet, all the main elements of the super-fast diffusion model are present. At low saturation levels, the liquid is only located on the rough surfaces of the fibres (including intrafibre pores) and in the liquid bridges formed at the intersections of the fibres (Sauret et al. 2014, 2015; Soleimani et al. 2015). The microscopic surface roughness of the fibres generates the capillary pressure to drive the liquid flow through the network, where the liquid bridges, as in the case of particulate media, play the role of variable volume reservoirs. We further assume that the liquid at least partially wets the fibres, so that the contact angle on rough surfaces of the fibres would be small (close to zero) or zero.

2.1 Morphology of Liquid Distributions in Fibrous Materials.

The morphology of the liquid bridges formed between the crossing fibres in the wetting case is found to be in general more complex than that observed between the particles (Alava and Niskanen 1994; Eichhorn and Sampson 2005; Herminghaus 2005; Niskanen and Alava 1994a; Rasi 2013; Sampson 2003; Scheel et al. 2008a,b). The liquid volume at the crossing of two rigid fibres can take under the action of surface tension forces several distinct morphologies depending on the amount of the liquid V_B, the separation distance and the angle between the fibres θ_f: a long liquid column, a mixed morphology state that consists of a drop on one side together with a small amount of liquid on the other side and a drop or a compact hemispherical drop or a pendular ring (Sauret et al. 2014, 2015; Soleimani et al. 2015). In general, the elongated liquid columns are only formed at small angles $\theta_f \leq 20^\circ$ between the crossing fibres (Sauret et al. 2015).

2.2 Pressure-Saturation Law

So, the predominant shape of the liquid volumes in randomly oriented fibrous materials appears to be either a drop or a pendular ring at small volumes $V_B R^{-3} \ll 1$ with the capillary pressure scaled as

$$p \approx -p_0 \left(\frac{R^3}{V_B} \right)^{\gamma_f}, \quad \gamma_f \approx 1/2, \tag{2.1}$$

where R is the characteristic fibre thickness and $p_0 = \frac{4\gamma \cos\theta_c}{R}$. In what follows, (2.1) is taken as the main pressure scaling law in capillary bridges at fibre crossings in our model. The pressure law is similar to that observed at low saturation levels in the pendular rings formed between the particles in particulate porous media leading to almost constant capillary forces acting between the fibres (Sauret et al. 2015).

2.3 The Structure of Fibrous Porous Materials and the Macroscopic Model.

The porosity of fibrous materials ϕ is highly variable (one can easily change paper porosity by applying moderate mechanical pressure to a sample), and in general it is much higher than that of particulate porous media. The typical porosity values for most paper grades are found to be around $\phi = 0.7$ (sand porosity, in comparison, is around $\phi = 0.3$) (Rasi 2013). The larger porosity values imply that overlapping (coalescence) of the liquid volumes attached to different crossings, the effect observed in particulate porous media (Herminghaus 2005; Scheel et al. 2008b), may only occur at much larger values of saturation.

It is well known that the structure of fibrous materials is effectively two-dimensional, that is the fibres are roughly oriented in the paper sheet plane. The main characteristics of the paper materials are therefore also two-dimensional, such as the total length of fibres L_q per unit area of a paper sheet. Typically, it takes the values in between $200 \leq L_q \leq 400\,\mathrm{mm}^{-1}$ at the characteristic paper thickness around $50\,\mu\mathrm{m}$ (Alava and Niskanen 1994). Given the characteristic fibre thickness R in the range $4\,\mu\mathrm{m} \leq R \leq 10\,\mu\mathrm{m}$, one can define the total length of fibres L_q per unit area in a layer of thickness R, which is expected in the range of $16 \leq L_e \leq 80\,\mathrm{mm}^{-1}$. The so obtained typical range is consistent with the typical paper porosity levels. Indeed, $\phi = \frac{V_E}{V}$, that is $\phi = 1 - \pi L_e R/4$ in a sample volume V of thickness R assuming circular fibre cross-section area $\pi R^2/4$. The estimate then gives $\phi \approx 0.7$, if we take parameters in the middle of their expected, estimated intervals, that is $L_e = 50\,\mathrm{mm}^{-1}$ and $R = 7\,\mu\mathrm{m}$. This implies that parameters ϕ, L_e and R characterising porous network are interrelated.

To characterise liquid distributions macroscopically, an average coordination number, that is the average number of crossings per unit volume N_c is to be defined. The value of L_e in a random paper network allows to estimate the mean distance l_f between the nearest fibre crossings $l_f \approx \frac{2}{\pi L_e}$ (Alava and Niskanen 1994). That is typical values of l_f are expected in the range $8\,\mu\text{m} \leq l_f \leq 13\,\mu\text{m}$. Using $R = 7\,\mu\text{m}$ and $L_e = 50\,\text{mm}^{-1}$, one can obtain an estimate of the coordination number with a typical value $N_c = \frac{\pi L_e^2}{2R} \approx 5.6 \times 10^5\,\text{mm}^{-3}$. Note the dimension of $[N_c] = L^{-3}$.

To parametrize saturation, we split, as before, average liquid content in a sample volume $V = S_0 R$ of thickness R and surface area S_0 into two parts: the liquid contained on the rough surface of fibres and in the intrafibre pores of volume $V_r = L_e S_0 \delta_R^2$ and the liquid contained in the capillary bridges at the fibre crossings $V_c = \langle V_B \rangle^l N_c V$, where $\langle ... \rangle^l = V_l^{-3} \int_{V_l} d^3x$ designates, as before, intrinsic averaging over the liquid volume V_l within the sample volume element V. Here parameter δ_R has the dimension of length and can be interpreted as the characteristic length scale of the surface roughness (intrafibre pore size), which may be regarded as a fitting parameter of the model. We further assume that the rough surface of the fibres is fully saturated (Rye et al. 1998), such that the amount of the liquid stored on the surface and in the intrafibre pores is independent of the liquid pressure, that is constant.

Combining both contributions, saturation

$$s = \frac{V_c + V_r}{\phi V}$$

can be presented as

$$s = \langle V_B \rangle^l V_0^{-1} + s_0, \quad s_0 = \frac{L_e \delta_R^2}{\phi R}, \quad V_0 = \frac{\phi}{N_c}.$$

Then, the average capillary bridge pressure $P =< p >^l$

$$P = -p_0 \left(\frac{R^3}{V_0} \right)^{1/2} \frac{1}{(s - s_0)^{1/2}}, \tag{2.2}$$

where $< ... >^l = V_l^{-1} \int_{V_l} d^3x$ is again the intrinsic liquid averaging. Using $L_e = 50\,\mathrm{mm}^{-1}$, $\delta_R = 1\,\mu\mathrm{m}$, $R = 7\,\mu\mathrm{m}$ and $\phi = 0.7$ as the typical parameters, one can estimate that $s_0 \approx 10^{-2}$, that is about 1%. This estimate is not far from the value of the similar quantity $s_0 \approx 0.35\%$ in the particulate porous media.

2.3.1 Local Transport in Fibres.

We know from previous studies of liquid spreading along rough surface grooves of various shapes and dimensions, (Rye et al. 1998), that the surface average volumetric flux density obeys a Darcy's Law. That is,

$$\mathbf{q} = -\frac{\kappa_m}{\mu} \nabla u, \tag{2.3}$$

here, as before, q is average flux density, u is a local pressure, μ is liquid viscosity and κ_m is the effective coefficient of permeability. As a matter of fact, a similar law would be observed in the process of wetting of a solid rod (Quere 1999). So in general, this kind of dependence is expected when the liquid is spreading in fibrous media. We note here that fibrous materials, as any porous structure, may have a hierarchy of different length scales. For example, a single fibre may consist of much thinner fibres packed together. In our model here, we take into account only the largest length scale available, assuming that smaller length scales are fully saturated. Basically, we treat smaller fibres as roughness of the larger fibre. Such an approach can be justified at low saturation considering the characteristic times involved in the process of spreading. Obviously, liquid spreading involving smaller length scale should be taking more time, that is being slower than that at the larger length scales due to the strong reduction of the permeability coefficient with the length scale. For example, in particulate porous media we have observed that $K \propto \delta_R^2 \frac{\delta_R}{R}$. So here, we use this separation of length scale to obtain a macroscopic model.

This would be instructive to estimate permeability of a fibre using some basic, simplified geometry, for example permeability of a section of an axisymmetric rod of radius R and length L_0, where the flow takes place in the surface layer of thickness δ_R, Fig. 2.1. If the pressure difference Δp is applied to the rod ends uniformly, the problem is one-dimensional so that the total flux Q_f is given by

$$Q_f = -2\pi R \delta_R \frac{\kappa_m}{\mu} \frac{\Delta p}{L_0}, \tag{2.4}$$

where $\kappa_m \propto \delta_R^2$. So, overall, the rod permeability is expected to be $\propto \delta_R^3/R$, similar to the permeability in the case of particulate porous media.

2.3.2 Macroscopic Model.

If we follow the same procedure as that in the particulate porous media using the spatial averaging theorem (Whitaker 1969) and applying intrinsic liquid average $\langle \ldots \rangle^l = V_l^{-1} \int_{V_l} \ldots d^3x$, one gets

$$-\frac{\kappa_m}{\mu} \nabla \langle u \rangle^l = \langle \mathbf{q} \rangle^l. \tag{2.5}$$

The non-linear super-fast diffusion equation can be recovered from (2.5) applying conservation of mass principle in a divergence form, that is,

$$\frac{\partial(\phi s)}{\partial t} + \nabla \cdot Q = 0, \tag{2.6}$$

$$Q = \frac{S_e}{S} < q >^l = -\frac{S_e}{S} \frac{\kappa_m}{\mu} \nabla \langle u \rangle^l.$$

Here, as before, S is the surface area of the sample volume V with the effective area of exists and entrances S_e and the global coefficient permeability $K = \kappa_m \dfrac{S_e}{S}$ (Lukyanov et al. 2012).

That is using a reasonable assumption that $P \approx \langle u \rangle^l$ and the pressure-saturation relationship (2.2), assuming that porosity ϕ is constant,

$$\frac{\partial s}{\partial t} = \nabla \cdot \left\{ \frac{D_0 \nabla s}{(s - s_0)^{3/2}} \right\}, \tag{2.7}$$

where

$$D_0 = \frac{1}{2} \frac{K}{\mu} \frac{p_0}{\phi} \left(\frac{R^3}{V_0} \right)^{1/2}.$$

In the case of a moving boundary-value problem with a smooth boundary $\partial\Omega$

moving with velocity $\mathbf{v}$, the super-fast diffusion equation (2.7) should be, as before in particulate porous media augmented with boundary conditions

$$
\begin{aligned}
& s|_{\partial\Omega} = s_f \ , \ s_f > s_0 \\
\text{and} \quad & \mathbf{v} \cdot \mathbf{n}|_{\partial\Omega} = -D_0 \, \frac{\mathbf{n} \cdot \nabla s}{s_f (s_f - s_0)^{3/2}} .
\end{aligned}
$$

where $\mathbf{n}$ is the normal vector to the boundary $\partial\Omega$ and s_f is the boundary value of the saturation which is defined by the capillary pressure developed at the moving front.

As is in the case of particulate porous media, the superfast diffusion model in fibrous materials requires the knowledge of the permeability coefficient K. Obviously, this coefficient can be only obtained by means of a model based on a lower level of description, which is called here the microscopic model. We will utilise a network model for this purpose, which is the subject of the next section. This way, we can not only determine the coefficient of permeability, but also validate the whole macroscopic model.

2.4 Microscopic Model

The idea of the microscopic network model is quite simple and almost straightforward, Fig. 2.1. First of all, we replace the actual fibres by straight transport links of given permeability (2.4) connecting nodal points of a network. The nodal points represent the capillary bridges of given capacity V_B, which is a function of local pressure given by the relationship (2.2). The initial distribution of the liquid in the network then evolves with time, such that on each 'small' time step

δt a certain amount of the liquid is transported between the nodes according to the permeability of the links and the pressure difference between the nodes. After that, the nodal pressure values are updated according to the amount of the liquid transported (assuming conservation of mass, of course) and the system evolves in time. This network design is similar to (Bronkhorst 2003; Corte and Kallmes 1962; Sampson 2003; Sauret et al. 2015) and (Niskanen and Alava 1994b), but essentially differs by the nodal capacity properties, which are characteristic to the super-fast diffusion phenomena, that is, for example, given by relationship (2.2).

The network model is two-dimensional reflecting the properties of fibrous materials simulating one layer of the fibres of the width R. To validate the macroscopic model and calculate the permeability coefficient, we consider a steady state one-dimensional representative problem (1.14) with the Dirichlet boundary conditions. Varying the network properties, we study the influence of microscopic parameters on the macroscopic properties.

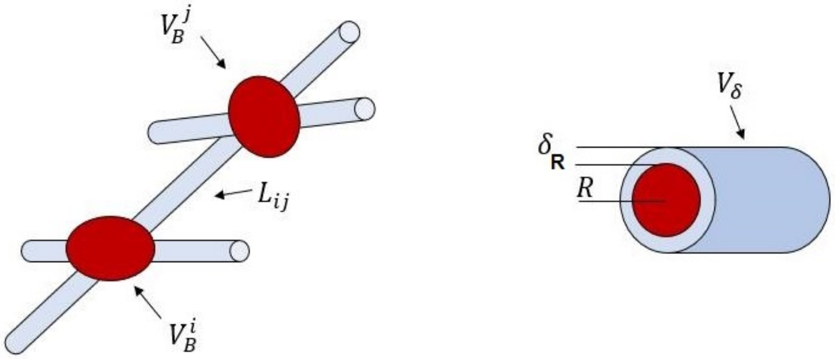

Figure 2.1: Illustration of the microscopic network.

2.4.1 Network Construction

The first step in the developing of our network model is to create a random distribution of nodes, the fibre crossings, connected by the links. In principle, every node can be connected to many neighbouring nodes, but in our analysis, we focus on mostly common situations observed in paper-like materials, when each node is only connected with three or four other nodes. The method of the mesh generation in our study is based on the properties of the the Delaunay triangulation, introduced in 1934 by Boris Delaunay (Enríquez-Cervantes and Rodríguez-Dagnino 2015), is characterised by an empty circumcircle property. The circumcircle of a triangle is an unique circle that passes through the three points of the triangle, see Fig. 2.2.

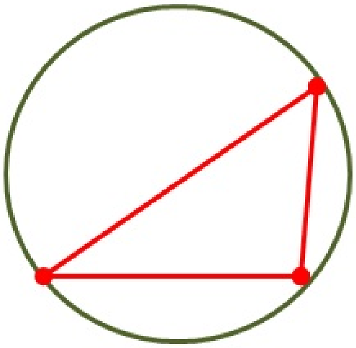

Figure 2.2: Illustration the circumcircle of a triangle.

Definition 2.1. *(Enríquez-Cervantes and Rodríguez-Dagnino 2015)*
A triangulation of a finite point set $P \in R^2$ *is called a Delaunay Triangulation, if the circumcircle of every triangle does not contain other points of* P *in its interior, that is, the circumcircle is empty.*

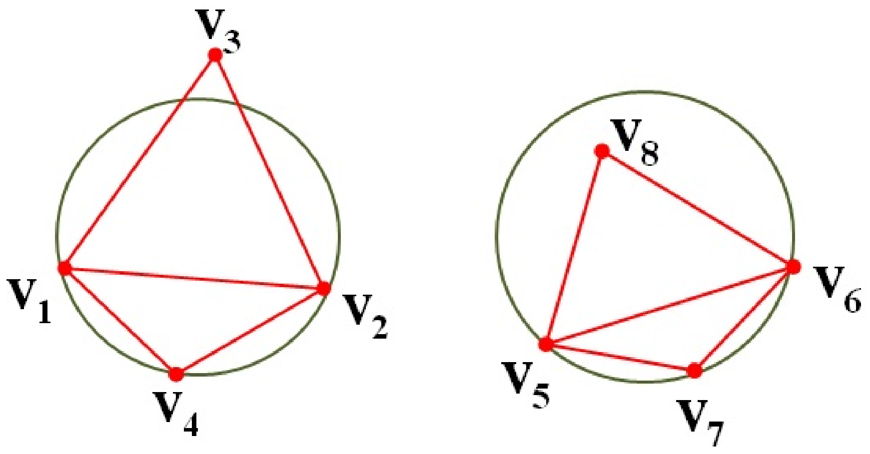

(a) (b)

Figure 2.3: Illustration of the Delaunay triangulation and the empty circumcircle criterion.

This is illustrated in Fig. 2.3. Some part of the Delaunay triangulation is shown in Fig. 2.3a, where the circumcircle does not contain a point in its interior. On the other hand, in Fig. 2.3b the circumcircle contains a point V_8 in its interior. Consequently, the second example does not represent the Delaunay triangulation.

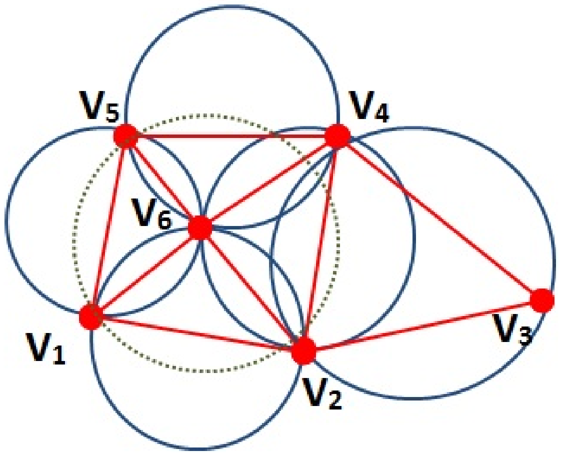

Figure 2.4: Illustration of a Delaunay triangulation with six points.

The example of the picture 2.4 is a Delaunay triangulation of a set of six points. The circumcircles of all five triangle satisfy an empty circumcircle property. However, the green dashed circle is not empty but it is not circumcircle of any triangle. So that is fine.

In case of four points in convex position, there are two possibility triangles which in general there is only one of them can be Delaunay, see Fig. 2.5

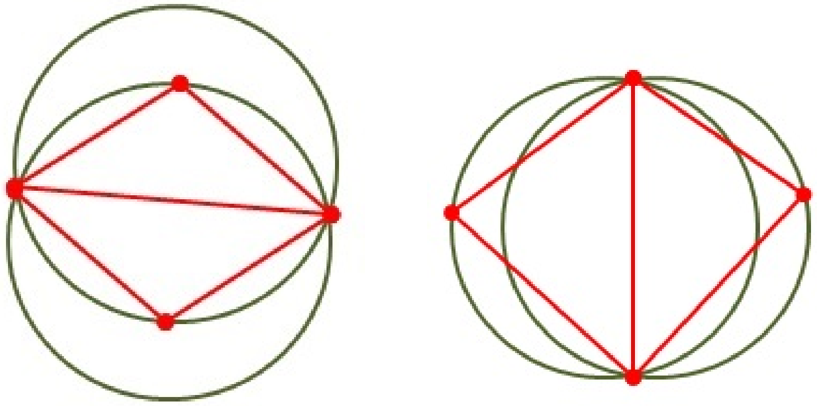

(a) Non-Delaunay triangulation (b) Delaunay triangulation

Figure 2.5: Illustration of the triangulations for four points in convex position.

If every points are on a edge of circle which is empty, so both of triangles are Delaunay, see Fig. 2.6

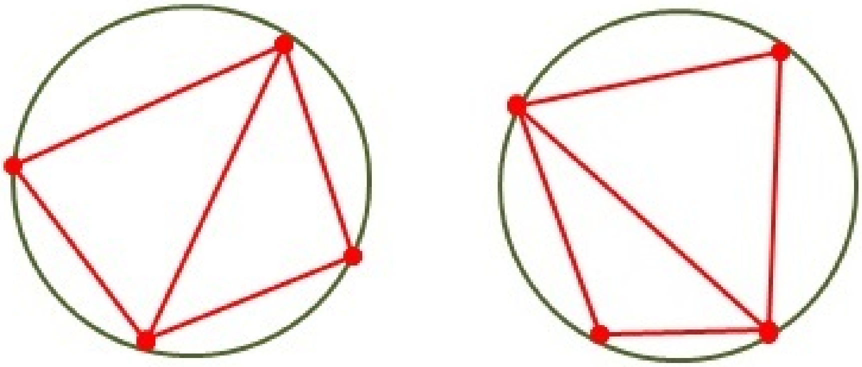

Figure 2.6: Illustration of the Delaunay triangulation.

Proposition 2.2. *Given P is a set of four points, $P \subset R^2$. If the point are in convex position but no co-circular, then set P has one Delaunay triangulation.*

Proof. The proof is in (Gärtner and Hoffmann 2014 page 59). □

These are the basic ideas to construct the Delaunay triangulation, which is generated in our study using Matlab 2018. More the details can be found in (Gärtner and Hoffmann 2014) and (Shewchuk et al. 2016).

We now generate the network model by considering the example Delaunay triangulation Fig. 2.4. The node inside each Delaunay triangulation has been created by using the property of barycentre such that each node has three neighbours, see Fig. 2.7.

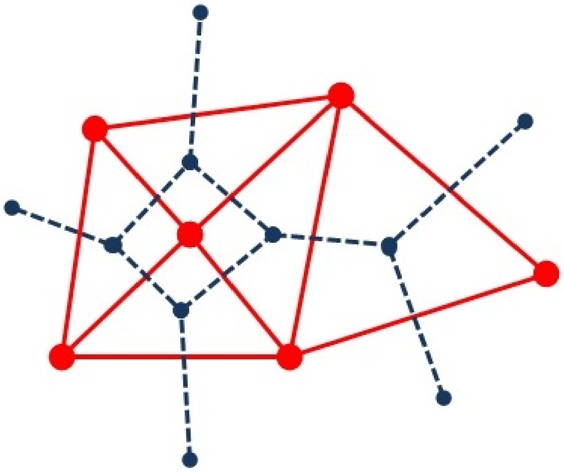

(a) Delaunay triangulation (red) with the connecting lines between barycentres (blue) of the triangles representing the crossing points in porous media.

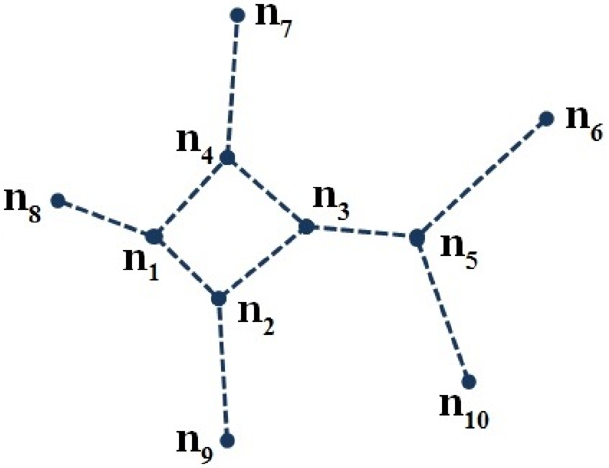

(b) Network model

Figure 2.7: Illustration of the resultant microscopic network model for 10 nodes.

Note that, the microscopic network model consisting of quadrilaterals can be constructed by combining two triangles.

2.4.2 Network Evolution: Time Steps and Liquid Transport

The volume capacity of each node of the network is designated by V_B^i at, say, node i and the liquid content in the fibre roughness will be ignored, since it is constant and can be added a posteriori, if necessary. In what follows in this chapter, unless otherwise stated explicitly, we use non-dimensional variables considering the fibre radius R as the characteristic length scale, capillary pressure $p_0 = \frac{4\gamma\cos\theta_c}{R}$ as the characteristic pressure, $I_0 = 2\pi\delta_R\kappa_m p_0\mu^{-1}$ as the characteristic flux along the fibre links, $q_0 = I_0/R^2 = 2\pi\frac{\delta_R}{R^2}\frac{\kappa_m p_0}{\mu}$ as the characteristic flux density and $t_0 = \frac{R}{q_0}$ as the characteristic time. In non-dimensional form, the nodal pressure-volume relationship takes the form

$$p^i = -\left(\frac{1}{V_B^i}\right)^{1/2}, \tag{2.8}$$

where for simplicity we used the same notation as for the dimensional variables.

At non-equilibrium, the liquid flux between the network nodes connected by the links is defined by the pressure difference. That is the volumetric flux between two nodes, i and j for example, connected by the filament of length L_{ij} is proportional to the pressure difference between the nodes

$$I_{ij} = -\alpha_{ij}\,\frac{p_j - p_i}{L_{ij}}, \tag{2.9}$$

where an additional parameter, a coefficient α_{ij} was introduced to generate models with different properties of the links. For example, when simulating porous media with nearly identical fibres (all links would be of cylindrical shape of diameter R having a uniform liquid layer of thickness δ_R carrying the liquid flux), one can set $\alpha_{ij} = 1$, on the other hand, in a more realistic scenario, one should regard the parameter α_{ij} as a random number distributed, somehow, between 0 and 1. In particular, we consider uniform distribution in the unit interval.

The macroscopic parameter, saturation (disregarding the capacity of the links) can be calculated by means of averaging over a sample area element S_0

$$s = \frac{\sum_i V_B^i}{\phi S_0 R} \tag{2.10}$$

where the summation is over all nodes within the surface element.

2.5 Liquid Spreading: a Steady State Problem

At non-equilibrium, the liquid distribution in the network evolves in time with a time step δt chosen such that to achieve numerical stability. After each time step the total amount of the liquid at every node is calculated according to the mass balance, that is the mass change due to the total flux through the links connected to the node and the amount at the previous time step.

To validate the macroscopic model and determine permeability, we use one-dimensional set-up, as is shown in Fig. 2.8.

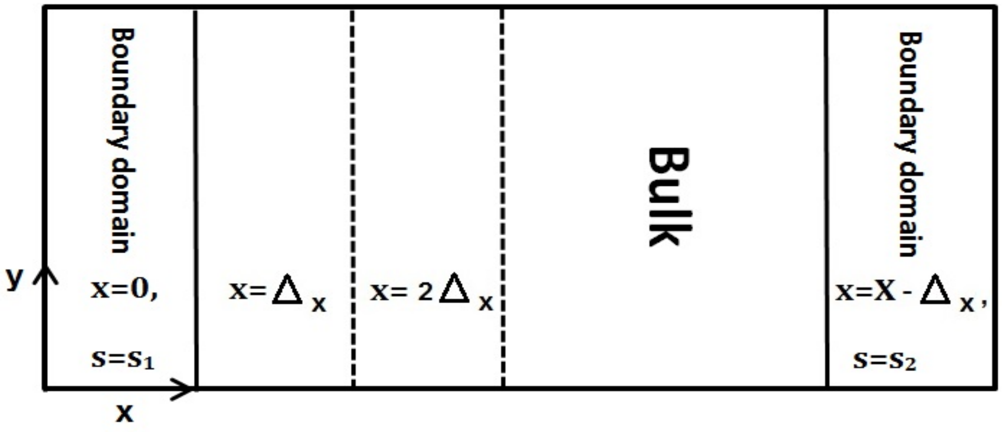

Figure 2.8: Illustration of the flow domain in the one-dimensional problem setup.

2.5.1 Setup for Averaging and the Macroscopic Boundary Conditions

The two-dimensional flow domain is a square area with a side size X, which is divided into equidistant strips in the x-direction of a fixed width Δ_x to facilitate averaging procedure (Δ_x is the averaging length scale) in the comparison with macroscopic results. The nodes in the first and in the last strip are kept at a fixed liquid volume to emulate Dirichlet boundary conditions with fixed boundary values of saturation. In the y-direction there are no explicitly imposed conditions, so naturally, the zero flux condition should be observed.

2.5.2 The Steady State Problem

The network nodes are distributed randomly but uniformly, so that the equivalent steady-state macroscopic problem is one-dimensional and can be formulated, similar to (1.14), in non-dimensional form as follows

$$\frac{\partial}{\partial x}\Big\{D(s)\frac{\partial s}{\partial x}\Big\} = 0, \quad x \in (0, X), \quad s > 0 \tag{2.11}$$

where the coefficient of diffusivity is expected at least to be proportional to $s^{-3/2}$. That is, using $q_0 = 2\pi\frac{\delta_R}{R^2}\frac{\kappa_m p_0}{\mu}$ as the characteristic flux density

$$D(s) = \frac{D_0(s)}{s^{3/2}}, \quad D_0(s) = \frac{1}{4\pi\phi}\frac{S_e}{S}\frac{R}{\delta_R}\left(\frac{R^3}{V_0}\right)^{1/2}. \tag{2.12}$$

Parameter $\left(\frac{R^3}{V_0}\right)^{1/2}$ represents the inverse number of fibre crossing in a volume element R^3, which is practically $\left(\frac{R^3}{V_0}\right)^{1/2} \approx 1$ considering that the non-dimensional parameter $\bar{N}_c = N_c R^3 = \frac{8}{\pi}(1-\phi)^2$. So the factor D_0 represents the scaling of S_e/S with $\frac{\delta_R}{R}$ and porosity ϕ. Basically, if we can determine D_0, then one gets the S_e/S scaling.

The diffusion equation should be augmented with the boundary conditions

$$s(0) = s_1 \ \text{ and } \ s(X) = s_2.$$

Obviously, in a steady state the flux density should be constant in the domain if its structure is homogeneous. That is equation (2.11) is equivalent to

$$D(s)\frac{\partial s}{\partial x} = \frac{q}{q_0} = \bar{q}. \tag{2.13}$$

Now we can run the network setup to reach a steady state as is described in appendices A - B and obtain the distribution of saturation to determine the functional form $D = D(s)$. The steady state is reached when the flux density distribution is uniform and is not evolving with time anymore.

2.6 Liquid Spreading: Numerical Results

We consider several representative sets of parameters. First, we will vary the resolution of the network model, that is the density of the nodes, which is directly related with the porosity of the samples. We consider two cases: $\bar{N}_c = 0.23$ corresponding to $\phi = 0.7$ and $\bar{N}_c = 0.64$ corresponding to $\phi = 0.5$ according to $\bar{N}_c = \frac{8}{\pi}(1-\phi)^2$.

Secondly, we vary the properties of the links using either constant coefficients $\alpha_{ij} = 1$ or more realistic parameter values randomly distributed between 0 and 1, such that $\langle \alpha_{ij} \rangle = 0.5$. We will also analyse two kinds of the networks. In the first type, each node has three neighbours, and in another one there are four neighbours.

2.6.1 Distribution of Pressure

The reduced size of the domain was chosen to be $X/R = 100$ in the simulations. This should be sufficient to accommodate $N_d = 2300$ nodes at $\phi = 0.7$ and $N_d = 6400$ nodes at $\phi = 0.5$ and to obtain statistically meaningful results after the averaging. Each strip in the domain, Fig. 2.8, should have at least 60 nodes, so that the relative error due to fluctuations is expected to be at 12%.

To study the boundary-value problem (2.11) in the range of low saturation values, we augment it with the boundary conditions

$$s_1 = 10^{-3}, \qquad s_2 = 0.2,$$

which have been fixed throughout the simulations.

Then we set an initial distribution of the mass at every node i according to a linear distribution of the saturation

$$s(x) = s_1 + x(s_2 - s_1)/100, \quad x \in (0, 100)$$

and let the system evolve to a steady state. The details of the algorithm, that is how the calculations are performed step-by-step, can be found in appendices A and B.

First, we consider the networks with each node having only three neighbours. We consider distribution of nodes with two characteristic densities $\bar{N}_c = 0.64$, $\phi = 0.5$ and $\bar{N}_c = 0.23$, $\phi = 0.7$. In each case, we run simulations with identical link permeabilties, $\alpha_{ij} = 1$, and with permeability values uniformly distributed in the interval $[0, 1]$, that is $\langle \alpha_{ij} \rangle = 0.5$.

The steady state was achieved at $t/t_0 \approx 100$, that is after approximately 10^7 times steps at $\delta t = 10^{-5}$ to be comfortably within the stability window, Fig. 2.9. With increasing the step size, the network evolution eventually becomes numerically unstable, as is expected. The steady state is illustrated in Fig. 2.10, for numerical values see Table 2.1, where the results have been averaged over five statistically independent experiments. We will use this averaging procedure throughout this chapter. One can observe in Fig. 2.10, that the flux fluctuations measured in the boxes are within the expected range of 12%. One can also observe that flux density increases as the nodal density $\bar{N}_c$ increases and, consequently the porosity ϕ decreases. This trend is expected, since with the increase of the nodal density there would be more pathways available to transport the liquid at a given value of the pressure difference, that is at the fixed boundary values of the saturation. One can notice another interesting trend that when the link permeabilities are randomly distributed, there exists strong reduction in the flux density values. While on average the link permeability is changed twofold, there is a threefold reduction in the density flux value. The fluctuations of the link permeability emulate the presence of inhomogeneities in the porous matrix, that is the presence of an additional length scale. Obviously, due to the non-linear character of the expected diffusion mechanism, the response function should also be non-linear - the effect, which is clearly observed.

The distribution of average pressure is shown in Fig. 2.11 The dependence of pressure is expected to be a power law monomial $s^{-1/2}$ according to our macroscopic analysis, equation (2.2), which is in non-dimensional form, ignoring contribution from the liquid stored in the links s_0,

$$\bar{P} = \left(\frac{\bar{N}_c}{\phi}\right)^{1/2} \frac{1}{s^{1/2}}. \tag{2.14}$$

This behaviour is clearly seen in the obtained dependencies if we fit them with $|P|/p_0 = \frac{A_f}{s^{1/2}}$, Fig. 2.11. As it might be expected, the distribution of pressure is insensitive to the distribution of the link permeabilities α_{ij}, but is a function of $\bar{N}_c$ or porosity ϕ. If we compare the prefactor $A_f^M = \left(\frac{\bar{N}_c}{\phi}\right)^{1/2}$ in the analytical expression of the macroscopic model (2.14) with the parameter A_f of the fitting function, then a very good agreement is also observed. Indeed, at $\bar{N}_c = 0.64$, $\phi = 0.5$, the obtained value of $A_f = 1.14 \pm 0.03$, while $A_F^M = 1.13$ is expected, and at $\bar{N}_c = 0.23$, $\phi = 0.7$, the obtained value of $A_f = 0.57 \pm 0.03$, while $A_f^M = 0.57$ is expected. That is, the network model turned out to be able to reproduce the macroscopic behaviour of the capillary pressure with excellent accuracy.

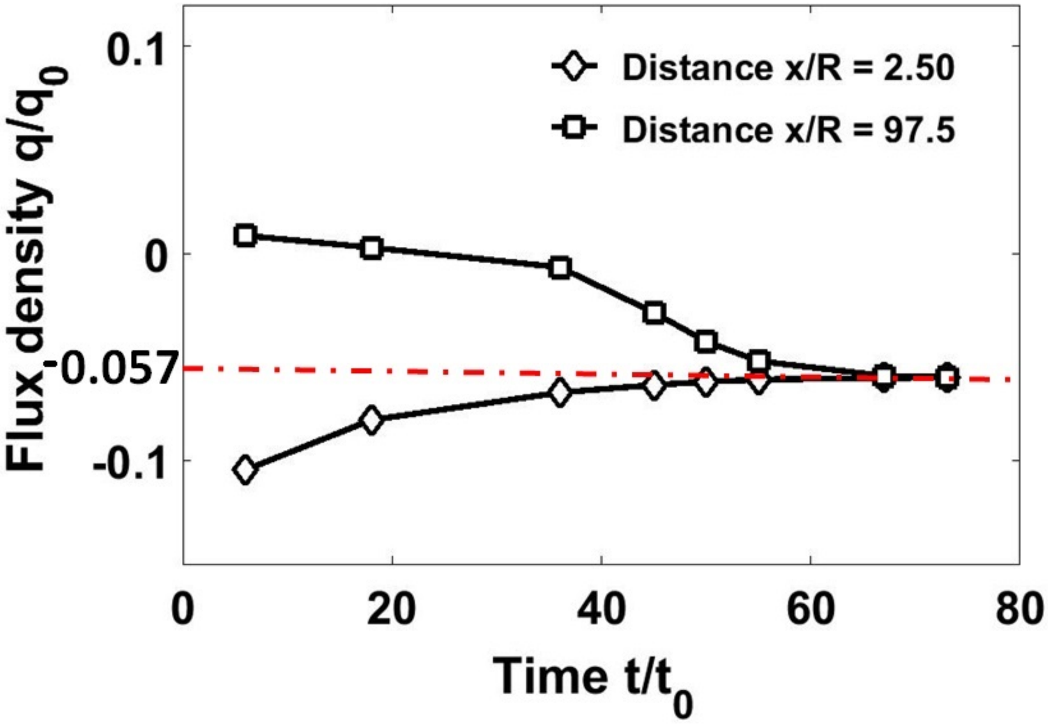

Figure 2.9: Averaged reduced flux density q/q_0 as a function of time t/t_0 in the setup with three nodal neighbours at $s_1 = 0.001$ and $s_2 = 0.2$ and random distributions of α_{ij} at $x/R = 2.5$ and $x/R = 97.5$. Here $\bar{N}_c = 0.64$ and $\phi = 0.5$.

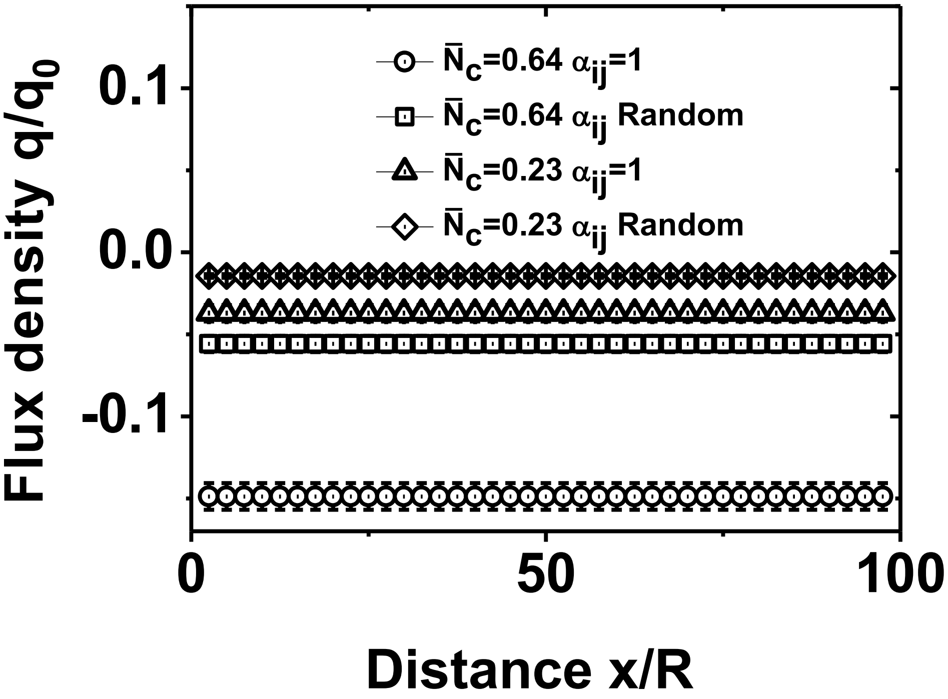

Figure 2.10: Averaged reduced flux density q/q_0 as a function of the reduced distance x/R in the setup with three nodal neighbours at $s_1 = 0.001$ and $s_2 = 0.2$ and different values of $\bar{N}_c$, and ϕ, $\bar{N}_c = 0.64$, $\phi = 0.5$ and $\bar{N}_c = 0.23$, $\phi = 0.7$, and different distributions of α_{ij}.

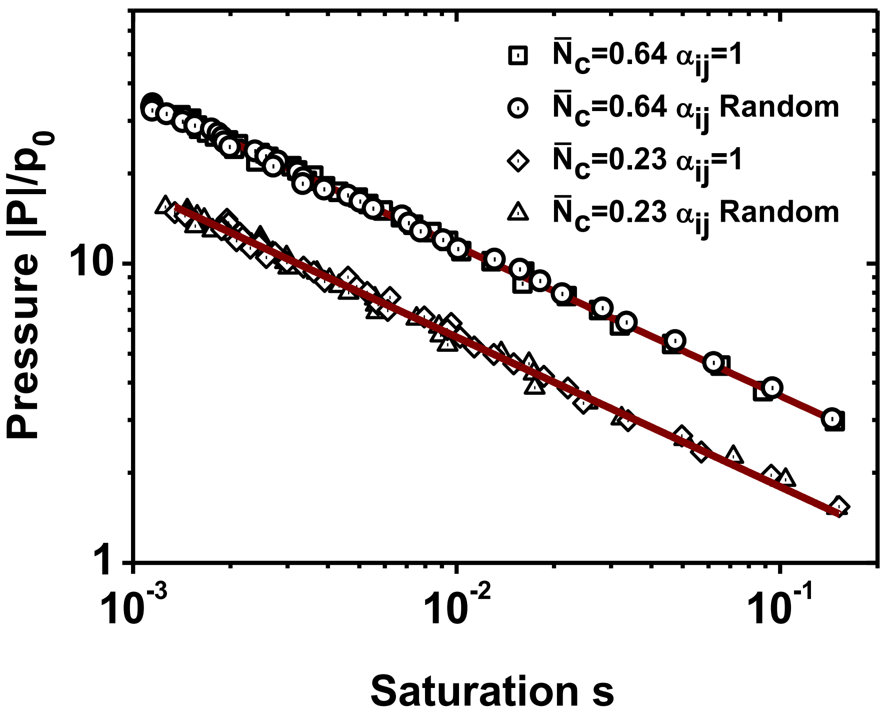

Figure 2.11: Averaged reduced capillary pressure $|P|/p_0$ as a function of saturation s in the setup with three nodal neighbours at $s_1 = 0.001$ and $s_2 = 0.2$ and different values of $\bar{N}_c$, and ϕ, $\bar{N}_c = 0.64$, $\phi = 0.5$ and $\bar{N}_c = 0.23$, $\phi = 0.7$, and different distributions of α_{ij}. The numerical data are shown by symbols and the solid lines (brown) indicate the fitting function $|P|/p_0 = \frac{A_f}{s^{1/2}}$.

2.6.2 Distribution of Saturation and Permeability of the Porous Network.

Consider now distribution of saturation. When all links in the network are identical, that is $\alpha_{ij} = 1$, the permeability of the network is not expected to depend on the saturation distribution, and one can anticipate that parameter $D_0 = const$ would be simply a constant. In this case, equation (2.11) can be easily integrated to obtain after applying the boundary conditions, we have the distribution of saturation

$$s^{-1/2} = -\frac{\bar{q}}{2D_0}x + s_1^{-1/2}, \tag{2.15}$$

and $s_2^{-1/2} = s_1^{-1/2} - \frac{\bar{q}}{2D_0}100$.

To facilitate the comparison, we plot function $s^{-1/2}$ versus the reduced distance x/R. The result is shown in Fig. 2.12. One can readily observe that the data indeed collapse on a linear dependence given by a fitting function $s^{-1/2} = A_s + B_s x$ at $A_s = 29.2 \pm 0.2$ and $B_s = -0.27 \pm 0.004$. This behaviour is characteristic and independent of the nodal density $\bar{N}_c$. It is very interesting to observe that the trend is also independent of the nature of the network link permeability. While with identical links, such behaviour is expected, randomly distributed links could have generated some dependence on the distribution of saturation. To the large extent, this effect is not observed. Some deviation can be possibly detected only at small saturation values, close to s_1. Now, the coefficients of the linear fit function allow to estimate the permeability coefficient. From the first coefficient, one can obtain $s_1 = 0.00117$, which is close to the specified value at the boundary $s_1 = 0.001$. The observed deviation is within the expected error of 12%. From the second coefficient, B_s, one can obtain that

$$\frac{\bar{q}}{2D_0} = -0.27.$$

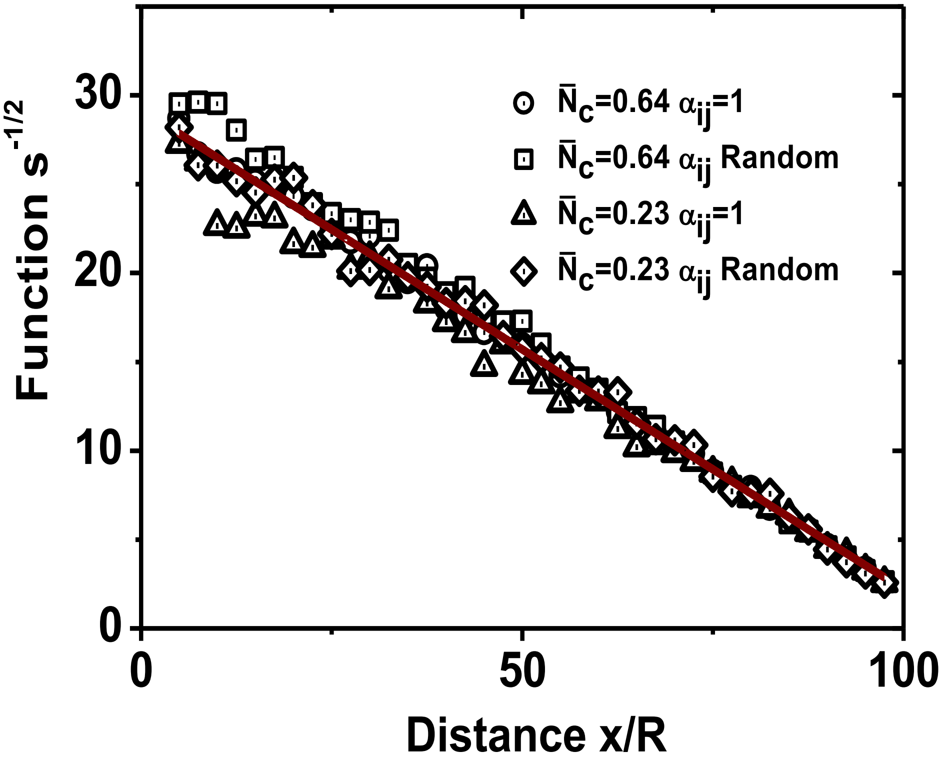

Figure 2.12: Averaged saturation $s^{-1/2}$ as a function of the reduced distance x/R in the setup with three nodal neighbours at $s_1 = 0.001$ and $s_2 = 0.2$ and different values of $\bar{N}_c$, and ϕ, $\bar{N}_c = 0.64$, $\phi = 0.5$ and $\bar{N}_c = 0.23$, $\phi = 0.7$, and different distributions of α_{ij}. The numerical data are shown by symbols and the solid line (brown) indicates the fitting function $s^{-1/2} = A_s + B_s x$ at $A_s = 29.2 \pm 0.2$ and $B_s = -0.27 \pm 0.004$.

That is, given flux density and porosity ϕ (or nodal density $\bar{N}_c$), one can estimate the scaling of S_e/S from (2.12). The results are summarised in Table 2.1.

Parameters	Nodes = 2300		Nodes = 6400	
	$\alpha = 1$	α - Random	$\alpha = 1$	α - Random
ϕ	0.7	0.7	0.5	0.5
$\bar{N}_c$	0.23	0.23	0.64	0.64
A_f	0.57	0.57	1.14	1.14
$\bar{q} \cdot 10^2$	-3.8 ± 0.6	-1.5 ± 0.1	-15 ± 0.8	-5.6 ± 0.5
D_0	0.07 ± 0.01	0.028 ± 0.002	0.28 ± 0.015	0.1 ± 0.009
$\frac{S_e}{S}$	$\frac{\delta_r}{R}$	$0.4\frac{\delta_r}{R}$	$1.5\frac{\delta_r}{R}$	$0.55\frac{\delta_r}{R}$

Table 2.1: Parameters of the microscopic network model with triangle tessellation and macroscopic parameters. All data has been averaged over five independent simulations.

Consider now the microscopic network model with four neighbours. Simulations with a similar set of parameters as that in the network with three nodal neighbours have shown qualitatively similar results, which are demonstrated in Figs. 2.13-2.14. One may notice larger flux densities in general due to the larger number of pathways available in the case of four-neighbour nodal points, Table 2.2. At the same time, as is expected, the distribution of pressure is identical including its variations with $\bar{N}_c$, Fig. 2.14.

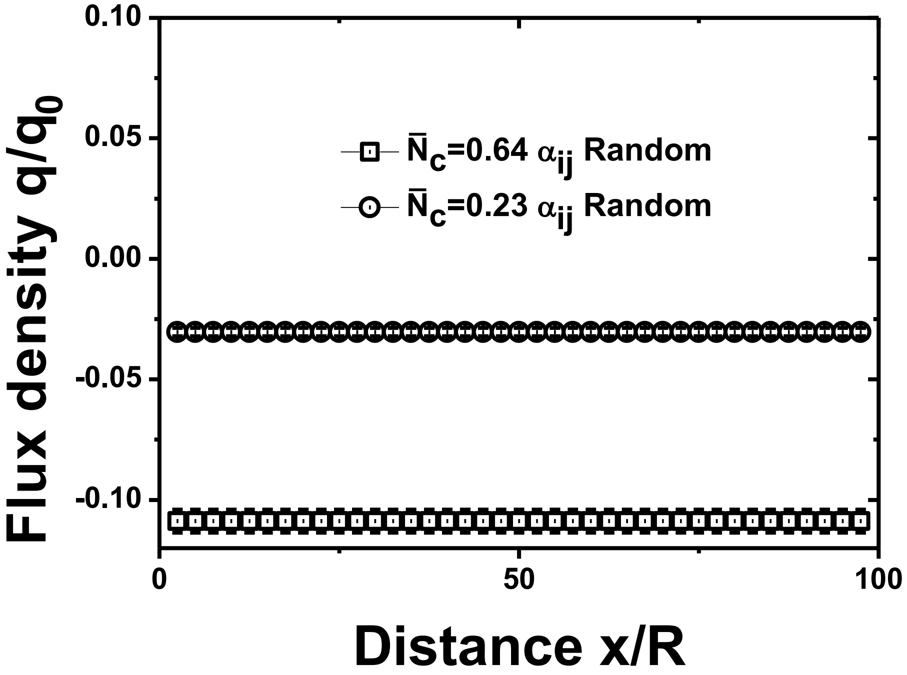

Figure 2.13: Averaged reduced flux density q/q_0 as a function of the reduced distance x/R in the setup with four nodal neighbours at $s_1 = 0.001$ and $s_2 = 0.2$ and different values of $\bar{N}_c$, and ϕ, $\bar{N}_c = 0.64$, $\phi = 0.5$ and $\bar{N}_c = 0.23$, $\phi = 0.7$.

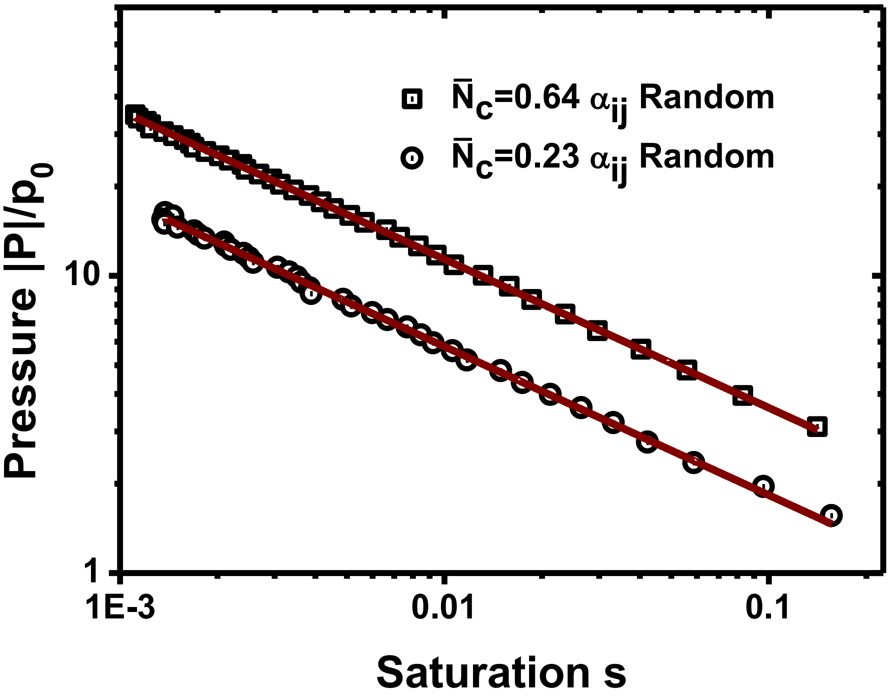

Figure 2.14: Averaged reduced capillary pressure $|P|/p_0$ as a function of saturation s in the setup with four nodal neighbours at $s_1 = 0.001$ and $s_2 = 0.2$ and different values of $\bar{N}_c$, and ϕ, $\bar{N}_c = 0.64$, $\phi = 0.5$ and $\bar{N}_c = 0.23$, $\phi = 0.7$. The numerical data are shown by symbols and the solid lines (brown) indicate the fitting function $|P|/p_0 = \frac{A_f}{s^{1/2}}$.

The results are summarised in Table 2.2.

Parameters	Nodes = 2300		Nodes = 6400	
	$\alpha = 1$	α - Random	$\alpha = 1$	α - Random
ϕ	0.7	0.7	0.5	0.5
$\bar{N}_c$	0.23	0.23	0.64	0.64
A_f	0.57	0.57	1.14	1.14
$\bar{q} \cdot 10^2$	-7.5 ± 0.4	-3 ± 0.2	-27 ± 1	-11 ± 0.5
D_0	0.14 ± 0.007	0.056 ± 0.004	0.5 ± 0.019	0.2 ± 0.009
$\frac{S_e}{S}$	$2.2\frac{\delta_r}{R}$	$0.86\frac{\delta_r}{R}$	$2.8\frac{\delta_r}{R}$	$1.1\frac{\delta_r}{R}$

Table 2.2: Parameters of the microscopic network model with quadrilateral tessellation and macroscopic parameters. All data has been averaged over five independent simulations.

This would be instructive to compare results obtained in the four-neighbour network with random distribution of nodes and in a regular network, for example in the network as is shown in Fig. 2.15, when the network consists of squares with the nodal points being in their vertices. If we calculated the flux density corresponding to the similar pressure difference as that with $s_1 = 10^{-3}$ and $s_2 = 0.2$ at the interval ends, then we would find that $\bar{q}_r = 0.08$ at $\bar{N}_c = 0.23$ and $\bar{q}_r = 0.27$ at $\bar{N}_c = 0.64$. As one can see, those values are very close to the results obtained with random distribution of nodes, Table 2.2, but identical links. So, in quadrilateral case, the regular analogue of the network should provide a good model to study the processes.

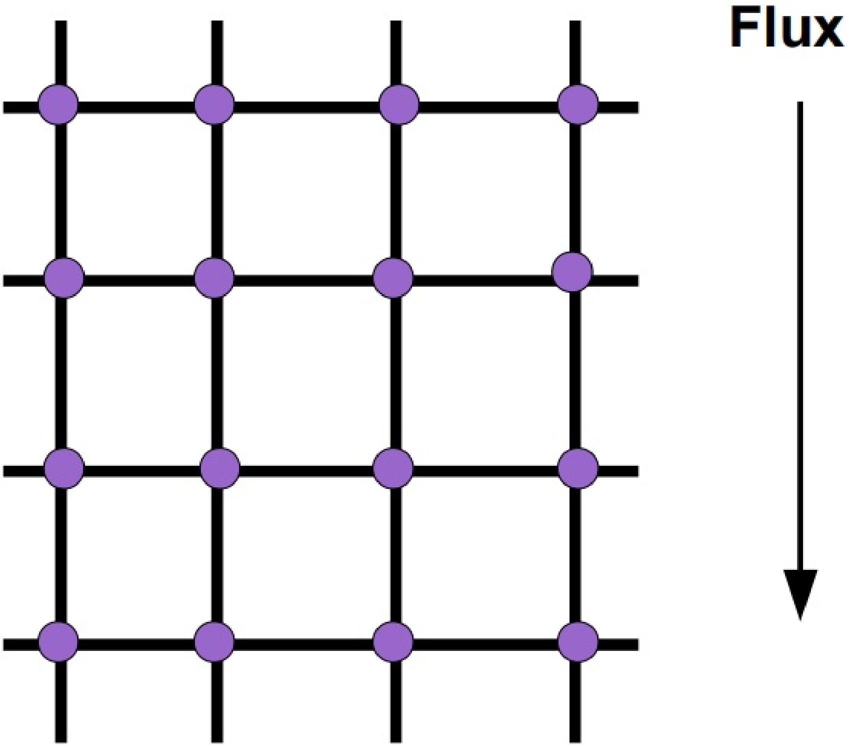

Figure 2.15: Illustration of a regular network with regular positions of the nodes.

In conclusion, the network model for liquid transport at low saturation levels we have developed was shown to be capable of reproducing macroscopic dynamics with high accuracy. Potentially, this model can be used to study complex phenomena by varying the model parameters such as the link permeability, fibre crossing density to simulate porous media with different non-uniform distribution of properties. The numerical scheme is shown to handle very well the peculiar character of the super-fast diffusion. The non-trivial behaviour is clearly observed when the link properties are distributed, which makes the model irreplaceable to study permeability properties in the case of complicated porous media compositions.

Chapter 3

The Laplace-Beltrami Equation and Permeability of Surface Elements

In this chapter, we return to the problem of capillary transport in particulate porous media. We have argued previously that to use the super-fast diffusion model (1.29) in practice, one needs to determine the permeability coefficient of the surface elements. It has been established that in the approximation of low capillary pressure, the surface roughness is saturated with the liquid and the transport process can be described by the Laplace-Beltrami equation (1.24). We first consider surface permeability of just one constituent element of the porous matrix. We demonstrate how the permeability coefficient of the element can be determined on the basis of solutions to the Laplace-Beltrami Dirichlet boundary value problem. We will generalise the method into a cluster of interconnected particles. In general, it is not feasible to find analytical solutions to the Laplace-Beltrami boundary value problems, so that their numerical treatment will be addressed in the next chapter. Here, we consider some special cases to determine analytical solutions to the problem. Based on the exact solutions, we consider how surface permeability can be incorporated into the macroscopic description.

Before considering the Laplace-Beltrami equation, we briefly introduce main notions, which are taken from (Dziuk and Elliott 2013). The details can be found in the following section.

3.1 Basic Notions

To begin with, we introduce a few concepts, which will be used in the context of the finite element method in Chapter 4. Let $\Omega \subset \mathbb{R}^3$ be a domain and $\Gamma \subset \Omega$ be a smooth surface in $\mathbb{R}^3$ and Ω_t be a neighbourhood of the surface Γ with normal coordinates $\nabla d(x)$ as is shown in Fig. 3.1.

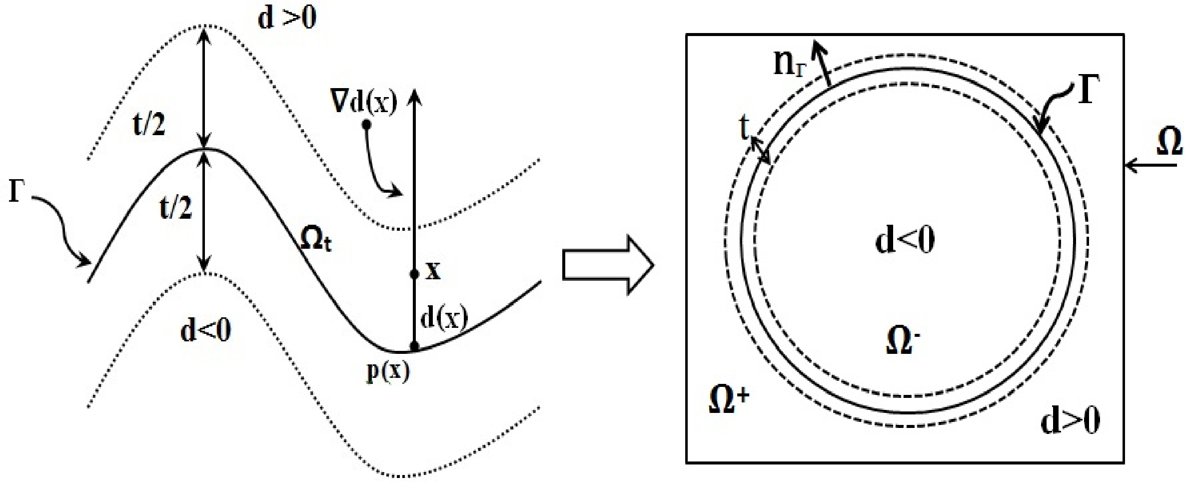

Figure 3.1: Neighbourhood Ω_t around the surface Γ and normal coordinates $\mathbf{x} = \mathbf{p}(\mathbf{x}) + d(\mathbf{x})\nabla d(\mathbf{x})$. Here n_Γ is a normal vector.

Consider a smooth surface shown in Fig. 3.1. The shortest distance from a point $\mathbf{x} \in \Omega_t$ to Γ can be defined as follows.

Definition 3.1. Signed Distance Function

Suppose that $\Gamma \subset \mathbb{R}^{n+1}$ be a compact smooth connected surface and contained by Ω_t, where n=1 or 2 (Dziuk and Elliott 2013). The sign distance function d for Γ is the shortest distance from a point $x \in \Omega_t$ to Γ which is defined by,

$$\begin{aligned} &d(x) < 0 \quad in \quad \Omega^- \\ &d(x) = 0 \quad on \quad \Gamma \\ &d(x) > 0 \quad in \quad \Omega^+. \end{aligned}$$

Here the domain Ω is split into an exterior open region Ω^+, an interior open region Ω^- and the boundary between them Γ, $\Omega = \Omega^+ \cup \Omega^- \cup \Gamma$.

In 2017, Cenanovic et al. described the neighbourhood around surface Γ. The detail is in the following theorem.

Theorem 3.2. *The neighbourhood around surface* Γ*, see Fig. 3.1 can be defined by*

$$\Omega_t = \{x \in \mathbb{R}^{n+1} : |d(\mathbf{x})| < t/2\},$$

and with $|\nabla d(\mathbf{x})| = 1$*, we have that* $\nabla d(x_\Gamma) = \mathbf{n}(x_\Gamma)$.

For every point $x \in \Omega_t$, the normal vector to Γ coincides with $\nabla d(\mathbf{x})$, thus we may introduce the nearest point projection map $p : \Omega_t \to \Gamma$, such that

$$\mathbf{p}(\mathbf{x}) = \mathbf{x} - d(\mathbf{x})\nabla d(\mathbf{x}). \tag{3.1}$$

We will get the Jacobian matrix by differentiating $\mathbf{p}(\mathbf{x})$. The first component, for example, yields

$$\frac{\partial p_1}{\partial x_1} = 1 - \frac{\partial}{\partial x_1}\left(d(\mathbf{x})\frac{\partial d(\mathbf{x})}{\partial x_1}\right) = 1 - \frac{\partial d(\mathbf{x})}{\partial x_1}\frac{\partial d(\mathbf{x})}{\partial x_1} - d(\mathbf{x})\frac{\partial^2 d(\mathbf{x})}{\partial x_1^2}.$$

The derivative in the matrix form is given by

$$D\mathbf{p} = \mathbb{I} - \nabla d(\mathbf{x}) \otimes \nabla d(\mathbf{x}) - d(\mathbf{x})D^2 d(\mathbf{x}).$$

Here $\mathbb{I}$ is a 3×3 identity matrix, $\otimes$ is the outer tensor product $(A \otimes B)_{ij} = A_i B_j$

and

$$D^2 d(\mathbf{x}) = \begin{bmatrix} \dfrac{\partial^2 d(\mathbf{x})}{\partial x_1^2} & \dfrac{\partial^2 d(\mathbf{x})}{\partial x_2 \partial x_1} & \dfrac{\partial^2 d(\mathbf{x})}{\partial x_3 \partial x_1} \\ \dfrac{\partial^2 d(\mathbf{x})}{\partial x_1 \partial x_2} & \dfrac{\partial^2 d(\mathbf{x})}{\partial x_2^2} & \dfrac{\partial^2 d(\mathbf{x})}{\partial x_3 \partial x_2} \\ \dfrac{\partial^2 d(\mathbf{x})}{\partial x_1 \partial x_3} & \dfrac{\partial^2 d(\mathbf{x})}{\partial x_2 \partial x_3} & \dfrac{\partial^2 d(\mathbf{x})}{\partial x_3^2} \end{bmatrix}.$$

For $\forall\, \mathbf{x} \in \Gamma$ we have $d(\mathbf{x}) = 0$, so that $d(\mathbf{x}) D^2 d(\mathbf{x}) = 0$ on surface.

Consequently for $\forall\, \mathbf{x} \in \Gamma$, we have the linear projector onto the tangent plane at $\mathbf{p}(\mathbf{x})$

$$D\, \mathbf{p}(\mathbf{x}) = \mathbf{I} - \nabla d(\mathbf{x}) \otimes \nabla d(\mathbf{x}) := P_\Gamma(\mathbf{x}).$$

Definition 3.3. Tangential Gradients

For a given function $u : \Gamma \to \mathbb{R}$ we can define its tangential gradient on Γ by

$$\nabla_\Gamma u = P_\Gamma \nabla u = \nabla u - (\nabla u \cdot \mathbf{n}_\Gamma)\mathbf{n}_\Gamma,$$

where P_Γ is the projection onto the tangent space and $\mathbf{n_\Gamma}$ is the normal vector (Dziuk and Elliott 2007).

3.2 Laplace-Beltrami Equation and Surface Permeability.

Let $\Omega_R \subset \mathbb{R}^3$ be a domain and $\Gamma \subset \Omega_R$ be a smooth surface in $\mathbb{R}^3$. Locally, on the surface of the porous matrix elements, such as sand grains, the transport is described by the Laplace-Beltrami equation over a generic manifold Ω

$$\Delta_{\Omega}\, u = 0, \tag{3.2}$$

where u is the liquid pressure.

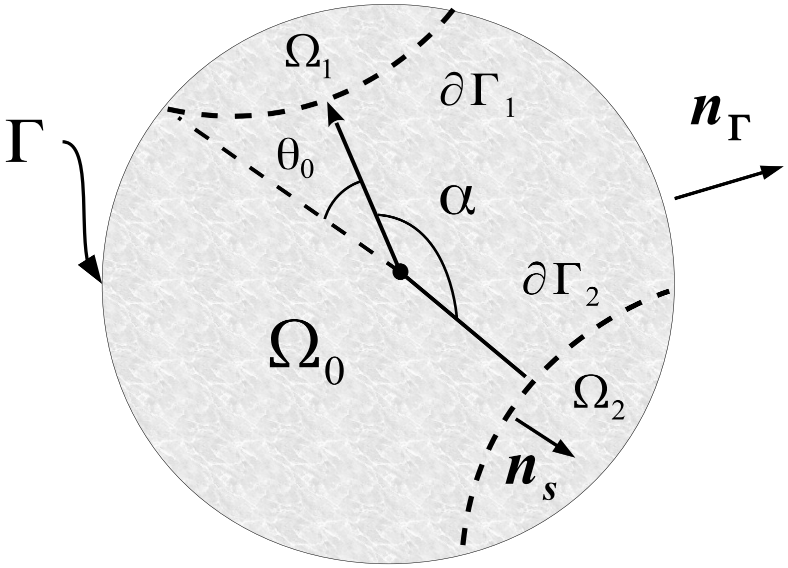

Figure 3.2: Illustration of the physical domains of the problem Ω_0, Ω_1 and Ω_2 with the boundaries $\partial\Gamma_1$ and $\partial\Gamma_2$ defined on Γ. Here, $\mathbf{n}_{\Gamma}$ is the unit outward normal vector to the surface Γ and $\mathbf{n}_s$ is the tangential outward normal vector to the boundaries $\partial\Gamma_{1,2}$.

On each element, one can distinguish at least two characteristic areas: some parts of the element surface are covered by the liquid being part of the bridge and other parts of the particle surface are saturated with the liquid, but it is only present in the surface roughness grooves. We note that there could be some dry areas on the particle surface. In the first approximation, we ignore their existence.

The surface area disposition is schematically illustrated in Fig. 3.2 when there are only two areas covered by the bridges on the surface, and hence there are three domains to consider Ω_0, Ω_1 and Ω_2. The transport described by (3.2) is only taking place in Ω_0. The character of the liquid flow is different in Ω_0, Ω_1 and Ω_2. The groove size $\delta_R \approx 1\,\mu$m is much smaller than that of the bridge, so that the grooves have much stronger resistance to the flow than the areas covered by the liquid bridges. The pressure difference over the bridge, that is in the domains Ω_1 and Ω_2 is thus expected to be negligible in comparison to that in Ω_0. Accordingly, we presume that the pressure is roughly constant in the bridges and on the boundary of the domains Ω_1 and Ω_2, that is on $\partial\Gamma_1$ and $\partial\Gamma_2$ respectively. Another plausible assumption, to simplify problem formulation and analysis is that $\delta_R = const$. As a result, the Laplace-Beltrami problem can be set solely in Ω_0, that is

$$\Delta_{\Omega_0} u = 0, \tag{3.3}$$

with Dirichlet boundary conditions on $\partial\Gamma_1$ and $\partial\Gamma_2$

$$u|_{\partial\Gamma_1} = U_1 = const \tag{3.4}$$

and

$$u|_{\partial\Gamma_2} = U_2 = const. \tag{3.5}$$

3.2.1 Permeability and the Laplace-Beltrami Boundary-Value Problem on a Single Particle Surface

Let $\Omega_R \subset \mathbb{R}^3$ be a domain and $\Gamma \subset \Omega_R$ be a smooth surface in $\mathbb{R}^3$ with the outward unit normal vector $\mathbf{n}_\Gamma$, see Fig. 3.2. We are going to consider the following partial differential equation on a subset Ω_0 of Γ with continuously differentiable boundaries $\partial\Gamma_j$

$$-\Delta_{\Omega_0} u = 0 \quad \text{on } \Omega_0, \tag{3.6}$$

where u is an unknown function that may represent the distribution of pressure on Ω_0. The Laplace - Beltrami operator on the surface Ω_0 is defined in the usual way by means of the tangential surface gradient and the outward normal vector $\mathbf{n_{\Omega_0}}$

$$\nabla_{\Omega_0} = \nabla - \mathbf{n}_{\Omega_0}(\mathbf{n_{\Omega_0}} \cdot \nabla),$$

such that

$$\Delta_{\Omega_0} = \nabla_{\Omega_0} \cdot \nabla_{\Omega_0}.$$

The partial differential equation (3.6) is augmented with Dirichlet boundary conditions

$$u|_{\partial\Gamma_1} = U_1 = const \tag{3.7}$$

and

$$u|_{\partial\Gamma_2} = U_2 = const, \tag{3.8}$$

where u_1 and u_2 are some constants.

For a smooth enough manifold, the problem (3.6) - (3.8) has a unique (weak) solution (Pigola et al. 2005). If a solution is found, one can determine the total flux Q_T passing through the boundary elements $\partial\Gamma_1$ and $\partial\Gamma_2$. Accordingly, we can then define the permeability of the single element K_1 by

$$Q_T = -R^2 \frac{K_1}{\mu} \frac{U_2 - U_1}{R}, \tag{3.9}$$

where R is the characteristic length scale of the element, the radius of the particle. Note, the total flux can be found according to (1.23)

$$Q_T = \delta_R \frac{\kappa_m}{\mu} \oint_{\partial\Gamma_1} \frac{\partial u}{\partial n_s}\, dl = -\delta_R \frac{\kappa_m}{\mu} \oint_{\partial\Gamma_2} \frac{\partial u}{\partial n_s}\, dl,$$

where $\mathbf{n}_s$ is the outward tangential normal vector to the boundaries $\partial\Gamma_j$ and operator $\frac{\partial}{\partial n_s} = \mathbf{n}_s \cdot \nabla$.

The problem (3.6) - (3.8) will be the first one, which we consider in the study in detail. Further in this chapter, we obtain some analytical solutions if Γ is a sphere and Ω_0 is a truncated sphere such that $\partial\Gamma_j$ are simply circles and the system has azimuthal symmetry. In a general case, there is little hope to obtain analytical solutions to the problem, so in Chapter 4 we consider how the problem can be solved numerically using a surface finite element technique.

3.2.2 Permeability and the Laplace-Beltrami Boundary-Value Problem for a System of Two Coupled Particles

However informative the surface permeability of a single particle is, in porous media, however, the particles are coupled via liquid bridges forming complex clusters of interconnected elements. In this case, the problem formulation is slightly different. As an example and as the first step, we consider the problem of two particles coupled through the "common" boundaries $\partial\Gamma_1^{(2)}$ and $\partial\Gamma_2^{(2)}$, as is shown in Fig. 3.3.

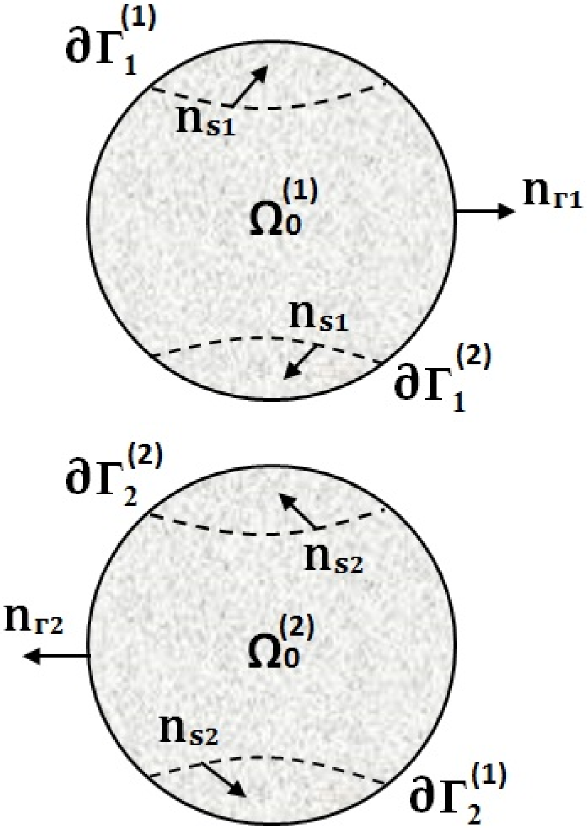

Figure 3.3: Illustration of the domains of two coupled (via a liquid bridge) particles. The flow domains are designated by $\Omega_0^{(1)}$ and $\Omega_0^{(2)}$ with the smooth boundary contours $\partial\Gamma_1^{(1)}$, $\partial\Gamma_1^{(2)}$, $\partial\Gamma_2^{(1)}$ and $\partial\Gamma_2^{(2)}$. Here, $\mathbf{n}_{\Gamma_j}$ are the outward unit normal vectors to Γ_j and $\mathbf{n}_{s_j}$ are the outward unit tangential normal vectors to the boundary contours on $\Omega_0^{(1)}$ and $\Omega_0^{(2)}$ respectively.

The two boundaries $\partial\Gamma_1^{(2)}$ and $\partial\Gamma_2^{(2)}$ belong to the same bridge coupling the particles. Liquid pressure variation in the bridges is negligible in slow, creeping flows in comparison to that in the surface flow domains $\Omega_0^{(k)}$. To put this differently, resistance to the flow of the bridge is much lower that that of the surface rough area. So from the physical point of view, we should require that the pressure is constant over $\partial\Gamma_1^{(2)}$ and $\partial\Gamma_2^{(2)}$ and is continuous. That is, if we designate pressure in $\Omega_0^{(1)}$ as u_1 and subsequently pressure in $\Omega_0^{(2)}$ as u_2

$$u_1|_{\partial\Gamma_1^{(2)}} = u_2|_{\partial\Gamma_2^{(2)}} = const.$$

Obviously, due to the conservation of mass in the absence of any sources or sinks of the liquid, one must require continuity of the total flux through the boundary contours as well, that is

$$\oint_{\partial\Gamma_1} \nabla u_1 \cdot \mathbf{n}_{s_1}|_{\partial\Gamma_1^{(2)}}\, dl = -\oint_{\partial\Gamma_2} \nabla u_2 \cdot \mathbf{n}_{s_2}|_{\partial\Gamma_2^{(2)}}\, dl,$$

where $\mathbf{n}_{s_1}$ and $\mathbf{n}_{s_2}$ are outward tangential normal vectors to the boundary contours.

To summarise, in the case of two coupled by a bridge particles, we are solving the following Laplace - Beltrami problem

$$-\Delta_{\Omega_0^{(1)}} u_1 = 0 \tag{3.10}$$

and

$$-\Delta_{\Omega_0^{(2)}} u_2 = 0, \tag{3.11}$$

with Dirichlet boundary conditions

$$u_1|_{\partial\Gamma_1^{(1)}} = U_1 \quad \text{and} \quad u_2|_{\partial\Gamma_2^{(1)}} = U_2$$

and two continuity conditions

$$u_1|_{\partial\Gamma_1^{(2)}} = u_2|_{\partial\Gamma_2^{(2)}} = const \tag{3.12}$$

and

$$\oint_{\partial\Gamma_1} \nabla u_1 \cdot \mathbf{n}_{s_1}|_{\partial\Gamma_1^{(2)}}\, dl = -\oint_{\partial\Gamma_2} \nabla u_2 \cdot \mathbf{n}_{s_2}|_{\partial\Gamma_2^{(2)}}\, dl, \tag{3.13}$$

where U_1 and U_2 are some constants. The two Dirichlet boundary conditions, as in the case of a single particle, set the pressure difference to create finite flux through the system. By calculating the total flux Q_T, one can then define the coefficient of permeability of the system of two coupled particles. The problem (3.10)-(3.13) will be analysed in detail further in this chapter. Numerically, the coupled particles problem will be considered in Chapter 5.

3.2.3 Permeability and the Laplace-Beltrami Boundary-Value Problem for a System of Many Interconnected Particles

Let's briefly discuss here a generalisation of the two coupled particle problem into a system of many particles, as is shown in Fig. 3.4. As in the previous cases, in this case, one needs to distinguish between surface areas covered by the liquid in bridges Ω_{ij} and the flow domains $\Omega_0^{(k)}$. Since in practice this problem is to define permeability of porous media, we only need to consider a finite, but representative, macroscopic set of particles. Therefore, sub-domains Ω_{ij} could be classed as internal, that is where the continuity boundary conditions are set, and external, that is where the Dirichlet boundary conditions are required to create surface flux through the system.

On the boundary of the external sub-domain, the pressure u is set to a constant value, while on the boundary of the internal sub-domain, we have continuity of pressure and the total flux.

That is, on each sub-domain $\Omega_0^{(k)}$ one has the Laplace - Beltrami problem, which can be written as

$$-\Delta_{\Omega_0^{(k)}} u = 0.$$

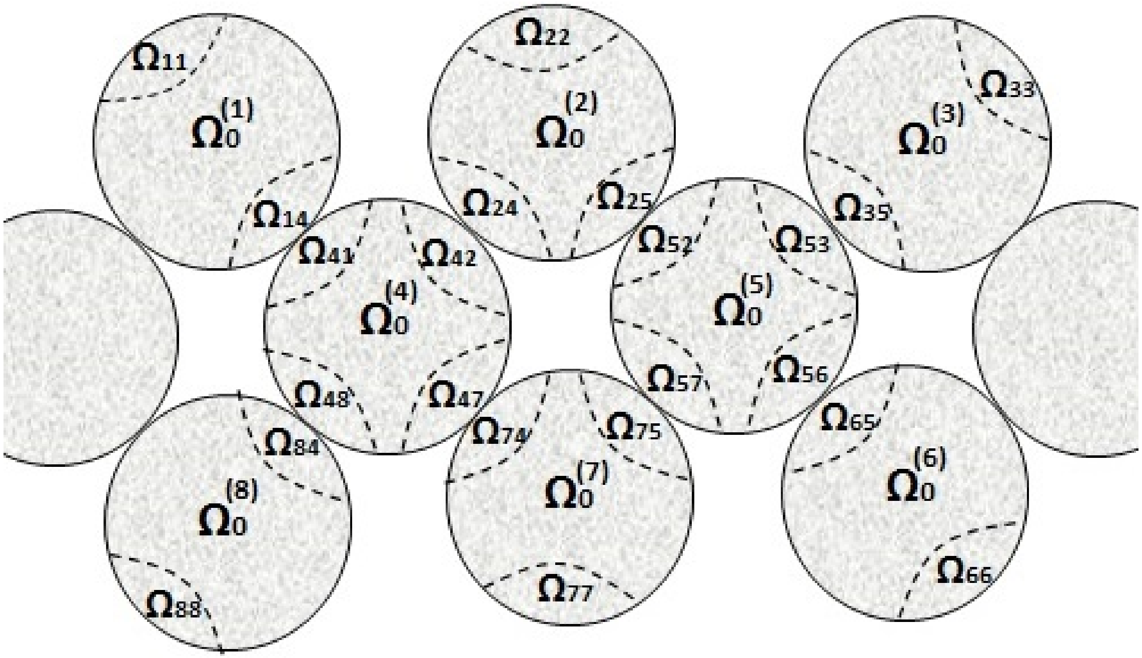

Figure 3.4: Illustration of the domains for the multi-particle connected problem

Consequently, the boundary conditions can be expressed for the internal sub-domains as

$$u|_{\partial\Gamma_{kj}} = u|_{\partial\Gamma_{jk}} = \text{constant},$$

$$\oint_{\partial\Gamma_{kj}} \nabla u \cdot \mathbf{n}_s|_{\partial\Gamma_{kj}}\, dl = -\oint_{\partial\Gamma_{jk}} \nabla u \cdot \mathbf{n}_s|_{\partial\Gamma_{jk}}\, dl,$$

and on the boundaries of the external sub-domains as

$$u|_{\partial\Gamma_{kk}} = \quad U_k \quad = \text{constant}.$$

We will consider this problem numerically in Chapter 6 to determine permeability of particulate porous media and now turn to some special cases admitting analytical solutions.

3.2.4 Analytical Solutions of the Laplace-Beltrami Boundary-Value Problem in Azimuthally Symmetric Case

The Laplace-Beltrami boundary-value problem does not admit analytical solutions in a general case on arbitrary surfaces with arbitrary boundary contours. To analyse general problems, we consider surface finite element techniques in Chapter 4. Here, we will analyse a few cases when analytical treatment is possible and the results are easily observable.

First of all, let's restrict our analysis to spherical particles, that is we consider first a single spherical particle of radius R, as is shown in Fig. 3.2. In the azimuthally symmetric case, the boundary contours are circles located in the opposite poles of the sphere.

We solve problem (3.6) in a spherical coordinate system with its origin at the particle centre and the polar angle θ counted from the axis of symmetry passing through the centre of the circular contours.

The domain is split into 3 sub-domains Ω_0, Ω_1 and Ω_2 with the boundaries $\partial\Gamma_1$ and $\partial\Gamma_2$. The size of the boundary circle is fixed and is defined by the value of the polar angle on the boundary circle. We consider a situation when there are two boundaries characterised by θ_0 and θ_1. Due to the symmetry, the solution is a function of only one variable, the polar angle θ, and the Laplace-Beltrami problem is simplified to

$$\frac{1}{\sin\theta}\frac{\partial}{\partial\theta}\left(\sin\theta\frac{\partial u}{\partial\theta}\right) = 0, \qquad \theta_0 \le \theta \le \pi - \theta_1 \tag{3.14}$$

with the Dirichlet boundary conditions

$$u_{\theta=\theta_0} = U_1 \quad \text{and} \quad u_{\theta=\pi-\theta_1} = U_2. \tag{3.15}$$

Equation (3.14) can be easily integrated twice to obtain after applying the boundary conditions (3.15)

$$u = \Psi_0(U_2 - U_1)\ln\left\{\frac{\sin\theta}{\sin\theta_0}\frac{1+\cos\theta_0}{1+\cos\theta}\right\} + U_1, \tag{3.16}$$

where

$$\Psi_0 = \frac{1}{\ln\left\{\frac{\sin\theta_1}{\sin\theta_0}\frac{1+\cos\theta_0}{1-\cos\theta_1}\right\}}.$$

One can now calculate total flux and define permeability of a spherical particle K_1

$$Q_T = -\frac{K_1}{\mu} D(U_2 - U_1) = -2\pi \sin\theta_0 \delta_R \frac{k_m}{\mu} \left. \frac{\partial u}{\partial \theta} \right|_{\theta=\theta_0} \tag{3.17}$$

$$= -(U_2 - U_1) 2\pi \delta_R \Psi_0 \frac{k_m}{\mu}, \tag{3.18}$$

where D is the characteristic length scale of the problem, κ_m is local permeability of the surface layer, δ_R is the layer width and μ is liquid viscosity.

So that, taking simply $D = 2R$,

$$K_1 = \pi \Psi_0 \frac{\delta_R}{R} k_m. \tag{3.19}$$

One can see that, if we take $\theta_1 = \theta_0$, the permeability coefficient K_1 is divergent at $\theta_0 = \pi/2$, as is expected, when the two contours move closer to each other and, at the same time, their radius $R \sin\theta_0$ increases, that is

$$K_1 = \frac{\delta_L}{2R} \frac{\pi \kappa_m}{\left(\frac{\pi}{2} - \theta_0\right)} + \mathcal{O}\left(\frac{\pi}{2} - \theta_0\right), \quad \theta_0 \to \frac{\pi}{2}$$

In the opposite limit, at $\theta_0 = 0$, when the two contours move further away from each other and their radius decreases, the permeability coefficient tends to zero, that is

$$K_1 = \frac{\delta_L}{2R} \frac{\pi \kappa_m}{|\ln\theta_0|} + o\left(\frac{1}{|\ln\theta_0|}\right), \quad \theta_0 \to 0. \tag{3.20}$$

Parametrically, the coefficient of permeability (3.19) is inversely proportional to the particle radius R, so that larger particles create stronger resistance to the flow. Noticeably, the coefficient demonstrates strong dependence on the surface layer thickness δ_R, that is $K_1 \propto \delta_R^3$ since it is anticipated that $k_m \propto \delta_R^2$, so that evaluation of this parameter in applications is crucial for the accurate estimates of the liquid dispersion rates.

How does the result affect the super-fast diffusion model (1.29), and basically how can it be incorporated into the main diffusion equation? First, we approximate the permeability coefficient K by K_1 obtained in the azimuthally symmetric case at $\theta_1 = \theta_0$. Secondly, we use an approximate relationship between the radius of curvature $R \sin\theta_0$ of the boundary contour $\partial\Gamma_1$ and the pendular ring volume V_B at $\theta_0 \ll 1$ or $(s - s_0^e) \ll 1$, see more details in (Herminghaus 2005),

$$R \sin\theta_0 \approx R\theta_0 = R\left(\frac{V_B}{R^3}\right)^{1/4},$$

to get

$$\theta_0(s) = (s - s_0)^{1/4}. \tag{3.21}$$

That is, from (3.20) and (3.21)

$$K_1 = \frac{\delta_L}{R}\frac{\pi\kappa_m}{|\ln(s - s_0)|}. \tag{3.22}$$

So, finally, (1.29) using (3.22) becomes

$$\frac{\partial s}{\partial t} = \nabla \cdot \left\{ \frac{D_0 \, \nabla s}{|\ln(s - s_0)|(s - s_0)^{3/2}} \right\}. \tag{3.23}$$

The model now includes a logarithmic correction to the non-linear coefficient of diffusion due to the specific permeability of spherical particles. This is the main result of this part. To some extent, this is an approximation, since we have used permeability of only one, single particle. To understand the accuracy of this assumption, our next step is to analyse the coupled particle problem. We note, also, that the obtained analytical solution represents a good benchmarking problem to test the numerical procedure implemented in Chapter 4. The character of the correction term $\propto \frac{1}{|\ln(s-s_0)|}$ will serve to provide a benchmark case to compare results obtained in Chapter 6.

3.2.5 Analytical Solution in the Case of Azimuthal Symmetry for the System of Two Coupled Particles

Consider two identical spherical particles (of radii R) coupled via a liquid bridge. In this case, the problem domain consists of two truncated spheres, Fig. 3.3, with functions representing distribution of pressure on each domain $\Omega_0^{(1,2)}$ designated by u_1 and u_2 respectively. We consider a slightly less general case, which is usually well observed in porous media, when the boundary contours are roughly of the same size due to slow variation of pressure in the system. Using again spherical coordinates on each domain $\Omega_0^{(k)}$ with polar angle θ and assuming azimutal symmetry (independence of distributions on the azimutal angle), the system of the Laplace - Beltrami equations (3.10)-(3.13) can be written as follows

$$\frac{1}{\sin\theta}\frac{\partial}{\partial\theta}\left(\sin\theta\frac{\partial u_1}{\partial\theta}\right) = 0 \quad , \quad \theta_0 \leq \theta \leq \pi - \theta_0 \tag{3.24}$$

and

$$\frac{1}{\sin\theta}\frac{\partial}{\partial\theta}\left(\sin\theta\frac{\partial u_2}{\partial\theta}\right) = 0 \quad , \quad \theta_0 \leq \theta \leq \pi - \theta_0, \tag{3.25}$$

but with a slightly different set of the boundary conditions

$$u_1 \,|_{\theta=\theta_0} = U_1, \tag{3.26}$$

$$u_2 \,|_{\theta=\pi-\theta_0} = U_2, \tag{3.27}$$

$$u_1 \,|_{\theta=\pi-\theta_0} = u_2\big|_{\theta=\theta_0} \tag{3.28}$$

and

$$\left(\sin\theta\frac{\partial u_1}{\partial\theta}\right)\bigg|_{\theta=\pi-\theta_0} = \left(\sin\theta\frac{\partial u_2}{\partial\theta}\right)\bigg|_{\theta=\theta_0}. \tag{3.29}$$

Obviously, equations (3.24) and (3.25) can be integrated twice, similar to the previous problem of a single particle (3.14), to obtain

$$u_1 = C_0 \ln\frac{\sin\theta}{1+\cos\theta} + C_1, \tag{3.30}$$

$$u_2 = B_0 \ln\frac{\sin\theta}{1+\cos\theta} + B_1, \tag{3.31}$$

where C_1 and B_1 are free constant parameters to be found from the boundary conditions, and θ_0 defines the size of the bridge footprint on the particle surface. Since we assumed, for simplicity, that all bridges are roughly identical, we have only one parameter θ_0 to describe the bridge size.

It is not difficult to see from (3.29), that one has $C_0 = B_0$ implying continuity of the contact flux. Applying the remaining boundary conditions (3.26)-(3.28), from (3.30) and (3.31)

$$u_1 = \Psi_0^{(2)}(U_2 - U_1)\ln\left(\frac{\sin\theta}{1+\cos\theta}\frac{1+\cos\theta_0}{\sin\theta_0}\right) + U_1, \tag{3.32}$$

$$u_2 = \Psi_0^{(2)}(U_2 - U_1)\ln\left(\frac{\sin\theta}{1+\cos\theta}\frac{1-\cos\theta_0}{\sin\theta_0}\right) + U_2, \tag{3.33}$$

where

$$\Psi_0^{(2)} = \frac{1}{2\ln\left(\frac{1+\cos\theta_0}{1-\cos\theta_0}\right)}.$$

One can now calculate total flux and define permeability of the coupled spherical particles K_2

$$\begin{aligned} Q_T = -\frac{K_2}{2\mu}D(U_2 - U_1) &= -2\pi\sin\theta_0\delta_R\frac{k_m}{\mu}\left.\frac{\partial u_1}{\partial\theta}\right|_{\theta=\theta_0} \\ &= -(U_2 - U_1)2\pi\delta_R\Psi_0^{(2)}\frac{k_m}{\mu}, \end{aligned}$$

where D is the characteristic length scale of the cross-section in the problem, κ_m is local permeability of the surface layer, δ_R is the layer width and μ is liquid viscosity.

So that, taking simply $D = 2R$,

$$K_2 = 2\pi\Psi_0^{(2)}\frac{\delta_R}{R}k_m. \tag{3.34}$$

3.2.6 Analytical Solution in the Case of Azimuthal Symmetry for the System of Three (and More) Particles

Consider three identical spherical particles (of radii R) coupled via a liquid bridge. In this case, the problem domain consists of three truncated spheres, Fig. 3.5, with functions representing distribution of pressure on each domain $\Omega_0^{(1,2,3)}$ designated by u_1, u_2 and u_3 respectively. As in the previous example, consider a slightly less general case, when the boundary contours are roughly of the same size due to slow variation of pressure in the system.

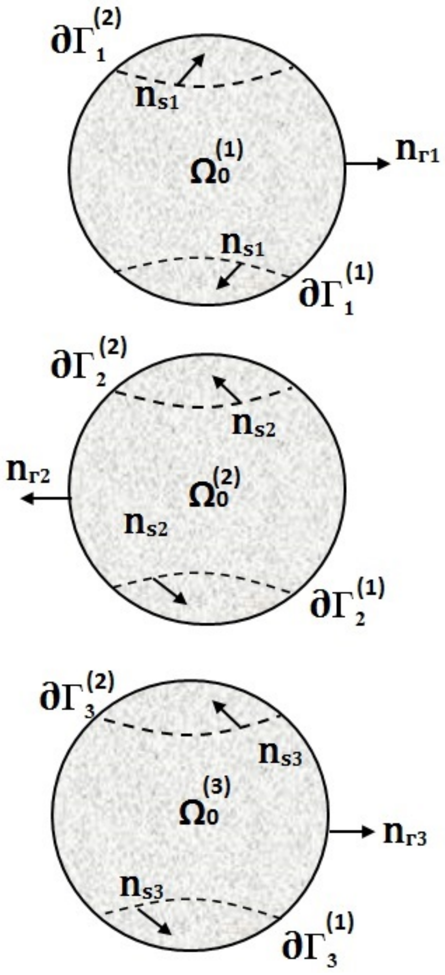

Figure 3.5: Illustration of the domains of the three linked (via a liquid bridge) particles. The flow domains are designated by $\Omega_0^{(1)}$, $\Omega_0^{(2)}$ and $\Omega_0^{(3)}$ with the smooth boundary contours $\partial\Gamma_1^{(1)}$, $\partial\Gamma_1^{(2)}$, $\partial\Gamma_2^{(1)}$, $\partial\Gamma_2^{(2)}$, $\partial\Gamma_3^{(1)}$ and $\partial\Gamma_3^{(2)}$. Here, $\mathbf{n}_{\Gamma_j}$ are the outward unit normal vectors to Γ_j and $\mathbf{n}_{s_j}$ are the outward unit tangential normal vectors to the boundary contours on $\Omega_0^{(1)}$, $\Omega_0^{(2)}$ and $\Omega_0^{(3)}$ respectively.

Using again spherical coordinates on each domain $\Omega_0^{(k)}$ with polar angle θ and assuming azimutal symmetry (independence of distributions on the azimutal angle), the system of the Laplace - Beltrami equations for three truncated spheres can be written as follows

$$\frac{1}{\sin\theta}\frac{\partial}{\partial\theta}\left(\sin\theta\frac{\partial u_1}{\partial\theta}\right)=0 \quad , \quad \theta_0 \le \theta \le \pi-\theta_0, \tag{3.35}$$

$$\frac{1}{\sin\theta}\frac{\partial}{\partial\theta}\left(\sin\theta\frac{\partial u_2}{\partial\theta}\right)=0 \quad , \quad \theta_0 \le \theta \le \pi-\theta_0 \tag{3.36}$$

and

$$\frac{1}{\sin\theta}\frac{\partial}{\partial\theta}\left(\sin\theta\frac{\partial u_3}{\partial\theta}\right)=0 \quad , \quad \theta_0 \le \theta \le \pi-\theta_0, \tag{3.37}$$

with the set of the Dirichlet and continuity boundary conditions

$$u_1\Big|_{\theta=\theta_0} = U_1 \quad \text{and} \quad u_3\Big|_{\theta=\pi-\theta_0} = U_3 \tag{3.38}$$

$$u_1\Big|_{\theta=\pi-\theta_0} = u_2\Big|_{\theta=\theta_0} \quad \text{and} \quad u_2\Big|_{\theta=\pi-\theta_0} = u_3\Big|_{\theta=\theta_0} \tag{3.39}$$

$$\sin\theta\,\frac{\partial u_1}{\partial\theta}\Bigg|_{\theta=\pi-\theta_0} = \sin\theta\,\frac{\partial u_2}{\partial\theta}\Bigg|_{\theta=\theta_0} \text{ and } \sin\theta\,\frac{\partial u_2}{\partial\theta}\Bigg|_{\theta=\pi-\theta_0} = \sin\theta\,\frac{\partial u_3}{\partial\theta}\Bigg|_{\theta=\theta_0} \tag{3.40}$$

The analytical solutions are given by

$$u_1 = A_0 \ln\frac{\sin\theta}{1+\cos\theta} + A_1, \tag{3.41}$$

$$u_2 = B_0 \ln\frac{\sin\theta}{1+\cos\theta} + B_1, \tag{3.42}$$

$$u_3 = C_0 \ln\frac{\sin\theta}{1+\cos\theta} + C_1. \tag{3.43}$$

where $A_{0,1}, B_{0,1}$ and $C_{0,1}$ are free constants, and θ_0 as before defines the size of the bridge footprint on the particle surface.

It is not difficult to see from (3.40), that one has $A_0 = B_0 = C_0$ implying continuity of the flux at the contacts. Applying the remaining boundary conditions (3.38)-(3.39), from (3.41)- (3.43), one gets a particular solution

$$u_1 = \Psi_0^{(3)}(U_3 - U_1)\ln\left(\frac{\sin\theta}{1+\cos\theta}\frac{1+\cos\theta_0}{\sin\theta_0}\right) + U_1, \tag{3.44}$$

$$u_2 = \Psi_0^{(3)}(U_3 - U_1)\ln\left(\frac{\sin\theta}{1+\cos\theta}\frac{1+\cos\theta_0}{\sin\theta_0}\right) + \frac{2}{3}U_1 + \frac{1}{3}U_3, \tag{3.45}$$

$$u_3 = \Psi_0^{(3)}(U_3 - U_1)\ln\left(\frac{\sin\theta}{1+\cos\theta}\frac{1-\cos\theta_0}{\sin\theta_0}\right) + U_3, \tag{3.46}$$

where

$$\Psi_0^{(3)} = \frac{1}{3\ln\left(\frac{1+\cos\theta_0}{1-\cos\theta_0}\right)}.$$

The total flux and permeability can be calculated in a similar way as in the case of two spheres

$$\begin{aligned} Q_T &= -\frac{K_3}{3\mu}D(U_3 - U_1) = -2\pi\sin\theta_0\delta_R\frac{k_m}{\mu}\frac{\partial u_1}{\partial\theta}\Big|_{\theta=\theta_0} \\ &= -(U_3 - U_1)2\pi\delta_R\Psi_0^{(3)}\frac{k_m}{\mu}, \end{aligned} \tag{3.47}$$

where as before D is the characteristic length scale of the cross-section in the problem, κ_m is local permeability of the surface layer, δ_R is the layer width and μ is liquid viscosity.

So that, taking $D = 2R$, one obtains

$$K_3 = 3\pi\Psi_0^{(3)}\frac{\delta_R}{R}k_m. \tag{3.48}$$

3.2.7 Permeability of a System of Particles in a Symmetrical Case

Basically, summarising, from (3.19), (3.34), (3.34) and (3.48), one can see that the permeability of a system of two coupled particles K_2 is identical to that of a single particle,

$$\frac{K_2}{K_1} = \frac{2\Psi_0^{(2)}}{\Psi_0} = 1 \tag{3.49}$$

and the permeability of a system of three particles K_3 is also identical to that of a single particle,

$$\frac{K_3}{K_1} = \frac{3\Psi_0^{(3)}}{\Psi_0} = 1. \tag{3.50}$$

It is not difficult to discern by deduction that in a general case of N coupled particles in a chain

$$K_N = \pi N \Psi_0^{(N)} \frac{\delta_R}{R} k_m = K_1, \tag{3.51}$$

where

$$\Psi_0^{(N)} = \frac{1}{N \ln\left(\frac{1+\cos\theta_0}{1-\cos\theta_0}\right)}.$$

Note, experimentally, the setup of many beads coupled by liquid bridges is often used in microfluidics to create flexible water channels (Chen et al. 2016).

In conclusion, surface permeability of porous matrix elements is shown to be evaluated on the basis of the Laplace-Beltrami boundary value problem. A correction to the global permeability coefficient of the porous matrix is discussed using analytically treatable symmetric cases. It is interesting, and important, that for a system of coupled spherical particles arranged in a chain, the line permeability is given by permeability of a single spherical particle with azimuthally symmetric boundaries. A chain of particles is still an approximation to real configurations of particulate porous media. One can expect effects of tortuosity. This will be investigated in Chapter 6, where we use random packing configuration and study their characteristic permeability.

Chapter 4

Weak Formulation and Numerical Solution of the Laplace Beltrami Problem

The goal of this chapter is twofold. First of all, it is to consider numerically a weak formulation of a problem, closely related to (3.2), but without complications emerging from the boundaries on the surface element. This is to benchmark the main numerical method in the study, the surface finite element technique applied to weak formulations of the Laplace-Beltrami problems. Once the weak formulation and the implementation of the numerical procedure was thoroughly verified, we proceed with the second goal, which is to consider the main problem (3.2) now with domain boundaries and with Dirichlet boundary conditions.

4.1 The Surface Finite Element Method

In this section, we will consider the following Laplace-Beltrami type equation on the closed surface Γ:

$$-\Delta_\Gamma u + cu = f \quad \text{on } \Gamma, \tag{4.1}$$

which we will use for benchmarking. We suppose that $f \in L^2(\Gamma)$ is a given source term and we will examine the cases when the constant $c > 0$ or when $c = 0$ and $\int_\Gamma f dA = 0$.

We now consider the solution of the Laplace-Beltrami equation in weak form which involves the use of weak derivative and surface Sobolev spaces as stated in the following definition.

Definition 4.1. Surface Sobolev Space

Assume that $p \in [1, \infty]$ *and let* m *be a non-negative integer (Hebey 2000). We define the Sobolev space of order* m *as*

$$W_p^m(\Omega) = \{u \in L^p(\Omega) : D^n u \in L^p(\Omega), \forall\, |n| \leq m\},$$

where D^n *is the tangential derivative of order* n *and the natural* m *is the order of the Sobolev space.(Dziuk and Elliott 2013.)*

The Sobolev norm is then

$$\|u\|_{W_p^m(\Omega)} = \left(\sum_{|n|\leq m} ||D^n u||^p_{L^p(\Omega)} \right)^{1/p} \qquad \text{when } 1 \leq p < \infty,$$

and

$$\|u\|_{W^m_\infty(\Omega)} = max \sum_{|n|\leq m} ||D^n u||_{L^\infty(\Omega)} \qquad \text{when } \ p = \infty.$$

We also consider the semi-norms as follows

$$|u|_{W^m_p(\Omega)} = \left(\sum_{|n|=m} ||D^n u||^p_{L^p(\Omega)} \right)^{1/p} \qquad \text{when } \ 1 \leq p < \infty,$$

and

$$|u|_{W^m_\infty(\Omega)} = max \sum_{|n|=m} ||D^n u||_{L^\infty(\Omega)} \qquad \text{when } \ p = \infty.$$

Note that, in case of $p = 2$, the space $W^m_2(\Omega)$ is **a Hilbert space.**

The above definition, now we can define a weak formulation of 4.1: For all $\phi \in H^1(\Gamma)$, find the solution $u \in H^1(\Gamma)$ such that

$$\int_\Gamma \nabla_\Gamma u \cdot \nabla_\Gamma \phi \, dA + c \int_\Gamma u\phi \, dA = \int_\Gamma f\phi \, dA. \tag{4.2}$$

where dA is the surface measure. In case $c = 0$ we must impose the additional constraint

$$\int_\Gamma u \, dA = 0.$$

We can rewrite the equation 4.2 into a bilinear form $a : H^1(\Gamma) \times H^1(\Gamma) \to \mathbb{R}$ and a linear form $l : H^1(\Gamma) \to \mathbb{R}$. Find $u \in H^1(\Gamma)$ such that

$$a(u, \phi) = l(\phi), \tag{4.3}$$

where,

$$a(u, \phi) = \int_{\Gamma} \nabla_{\Gamma}\phi \cdot \nabla_{\Gamma} u dA + \int_{\Gamma} cu\phi dA$$

and

$$l(\phi) = \int_{\Gamma} f\phi dA$$

for all $u, \phi \in H^1(\Gamma)$.

Theorem 4.2. *(Well-posedness) There exists a unique weak solution* $u \in H^1(\Gamma)$ *satisfying 4.3 (Ranner 2013), such that*

$$||u||_{H^1(\Gamma)} \leq c||f||_{L^2(\Gamma).} \tag{4.4}$$

Next, we will describe a partitioning (approximating) of the problem domain into finite elements, triangles in our case.

4.1.1 Triangulated Surface and the Finite Element Space

Consider a smooth surface Γ, which is approximated by a piecewise polynomial surface Γ_h, in the simplest case the approximating surface Γ_h is a space consisting of triangles in T. The approximation surface Γ_h is a Lipschitz surface and lies in Ω_t (Dziuk and Elliott 2013)

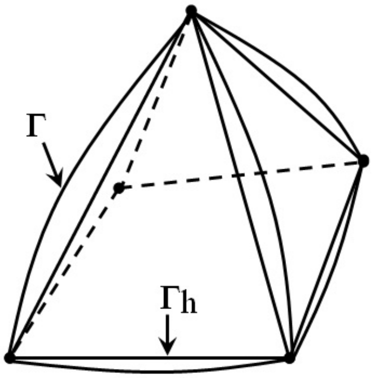

Figure 4.1: Approximation Γ_h of a smooth surface Γ.

Suppose that the discrete triangulate surface Γ_h has the following properties, (Guzman et al. 2018) :

1. Γ_h is the nonempty set of all triangles, such that

$$\bigcup_{T \in \mathfrak{T}_h} T,$$

   where $\mathfrak{T}_h$ is the set of all triangles T.

2. All vertices belong to Γ.
3. Two triangles $T_i, T_j \in \mathfrak{T}_h$, we have $T_i \cap T_j = \emptyset$ whenever $i \neq j$.
4. For two neighbours triangles T_i and T_j should share a common edge.

To realise the triangulation we have made use of the software GMSH (Geuzaine and Remacle 2006). We use this to generate a coarse surface Γ_h and then refine by projecting the new degrees of freedom onto the surface to finer approximations, as illustrated in Figure 4.2.

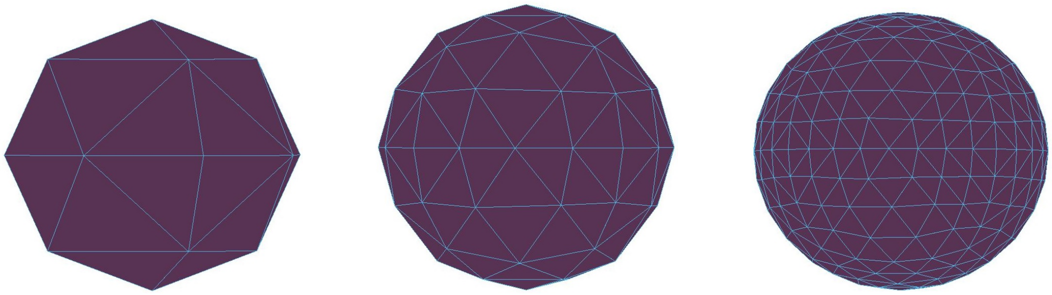

(a) No refinements, $N = 18$.

(b) 1^{st} refinements, $N = 66$.

(c) 2^{nd} refinements, $N = 258$.

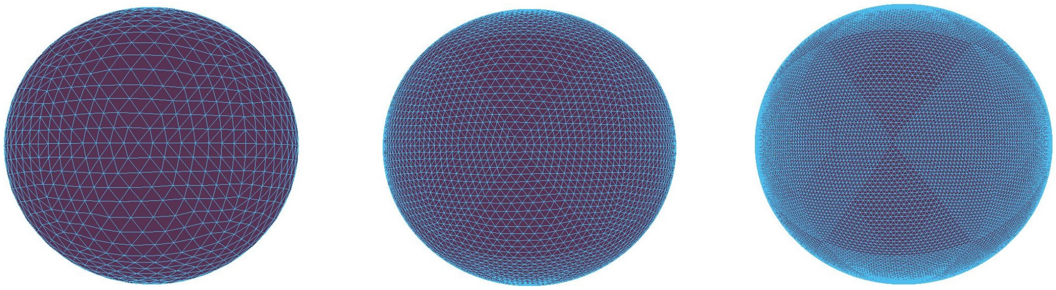

(d) 3^{rd} refinements, $N = 1026$.

(e) 4^{th} refinements, $N = 4098$.

(f) 5^{th} refinements, $N = 16386$.

Figure 4.2: Illustration examples of refinements of the surface with a sphere, where N is number of nodes.

Now, we are in a position to approximate the solution of the Laplace-Beltrami equation over the discrete surface. We begin by recalling the definition of the tangential gradient from the definition 3.3 as

$$\nabla_\Gamma u = P \nabla u.$$

If we construct and analytically treat an approximation of the smooth surface Γ

by the discrete surface Γ_h which is defined by the union of the set of all triangles

$$\bigcup_{T \in \mathfrak{T}_h} T,$$

then will obtain the tangential gradient on the discrete surface in a piecewise sense as follows

$$\nabla_{\Gamma_h} u = P_h \nabla u$$

where $(P_h)_{ij} = \delta_{ij} - \mathbf{n}_{hi}\mathbf{n}_{hj}, \quad$ (i,j=1,2,3,...,n).

Next, we set up the surface finite element method on discrete surface for solving the Laplace-Beltrami Equation. Since the approach is quite transparent, firstly we will treat the piecewise linear finite element on the discrete surface and then approximate the solution of the Leplace-Beltrami equation.

We have the definition of the piecewise linear finite element space on the discrete surface as (Dziuk and Elliott 2013):

$$V_h := \{\phi_h \in C^0(\Gamma_h) \Big| \ \phi_h\big|_T \ \text{ is a linear function for each } T \in \mathfrak{T}_h\}.$$

The space above is spanned by the nodal basis $\chi_1, \chi_1, ...\chi_N$, that is, $V_h = span(\chi_i)$. Furthermore, we have that

$$\chi_j \in V_h$$

and for nodal values X_k over Γ_h

$$\chi_j(X_k) = \delta_{jk},$$

where $j, k = 1, 2, 3, ..., N$.

Since $\{\chi_i\}$ forms a basis of V_h we have that every function $U_h \in V_h$ can be written as

$$U_h(x) = \sum_{j=1}^{N} \alpha_j \chi_j(x), \qquad (x \in \Gamma_h)$$

for some real constants α_j, $j = 1, 2, 3, ..., N$.

4.1.2 The Discrete Variational Equation

Next, the finite element method can be defined by the problem 4.2 which consists of the following discrete version of the weak formulation :

Definition 4.3. *Let $V_h \subset H^1(\Gamma)$ then the finite element approximation is the unique function $U_h \in V_h$ such that*

$$\int_{\Gamma_h} \nabla_{\Gamma_h} \phi_h \cdot \nabla_{\Gamma_h} U_h dA_h + \int_{\Gamma_h} cU_h \phi_h dA_h = \int_{\Gamma_h} F_h \phi_h dA_h, \quad \forall \phi_h \in V_h. \tag{4.5}$$

As in the continuous case when $c = 0$ we impose the additional constraint that

$$\int_{\Gamma_h} U_h \phi_h dA_h = 0.$$

We can rewrite the equation 4.5 by modifying the bilinear and linear forms used in the continuous case, that is consider $a_h : V_h \times V_h \to R$ and $l_h : V_h \to R$ be defined through:

$$a_h(u, \phi) = \int_{\Gamma_h} \nabla_{\Gamma_h} \phi \cdot \nabla_{\Gamma_h} u dA_h + \int_{\Gamma_h} cu\phi dA_h$$

and

$$l_h(\phi) = \int_{\Gamma_h} f \phi dA_h.$$

The problem then becomes to find $U_h \in V_h$ such that

$$a_h(U_h, \phi_h) = l_h(\phi_h) \text{ for all } \phi_h \in V_h. \tag{4.6}$$

Theorem 4.4. *(Well-posedness, Ranner 2013). There exists a unique solution $U_h \in V_h$ to 4.5 that satisfies:*

$$||U_h||_{H^1(\Gamma_h)} \leq c||f||_{L^2(\Gamma).} \tag{4.7}$$

To practically compute the finite element approximation we notice that the equation 4.5 is actually a linear system for the solution $U_h = \sum\limits_{j=1}^{N} \alpha_j \chi_j$ and is equivalent to

$$\sum_{j=1}^{n} (\ K_{kj} + M_{kj})\ \alpha_j = F_k, \ \ (k = 1, 2, 3, ...N),$$

here the **stiffness matrix**

$$K_{kj} = \int_{\Gamma_h} \nabla_{\Gamma_h} \chi_k \cdot \nabla_{\Gamma_h}\ \chi_j dA_h \quad (k, j = 1, ..., N),$$

the **mass matrix**

$$M_{kj} = c \int_{\Gamma_h} \chi_k \chi_j dA_h, \quad (k, j = 1, ..., N)$$

and

$$F_k = \int_{\Gamma_h} F_h \chi_k dA_h.$$

Therefore, the linear system reads

$$(K + M)\alpha = F,$$

for $\alpha = (\alpha_1, \alpha_2, \alpha_3, ..., \alpha_N)$.

Note that this is a square symmetric system. To assemble the stiffness matrix and mass matrix, the computational of the surface derivative on the triangulate surface is require. The details of the finite element method are describe in appendix C.

4.2 Benchmarking

To test the implementation of the surface finite element procedure, we first consider a problem similar to the Laplace-Beltrami boundary value problem (3.2), but on a closed surface Γ in $\mathbb{R}^3$ without boundaries, that is presuming $\partial\Gamma = \emptyset$. The closed surface Γ is assumed to be smooth with a well-defined outward unit normal vector $\mathbf{n}_\Gamma$. In the first tests, we will find weak solutions to

$$-\Delta_\Gamma u + cu = f \quad \text{on } \Gamma \tag{4.8}$$

where u is an unknown function and Δ_Γ is the Laplace-Beltrami operator, which is defined on Γ in the usual way by means of the **tangential surface gradient**

$$\nabla_\Gamma = \nabla - \mathbf{n}_\Gamma(\mathbf{n}_\mathbf{\Gamma} \cdot \nabla)$$

such that

$$\Delta_\Gamma = \nabla_\Gamma \cdot \nabla_\Gamma.$$

In (4.8), $c \geq 0$ and f is a given source term, so that the equation represents a more general case of **a reaction-diffusion equation**, but on the other hand without boundaries on the surface, which may cause unnecessary complications in the numerical implementations. Note, in case c is identically zero, one needs to add more conditions to guarantee well-posedness of the problem (Olshanskii et al. 2012).

4.2.1 Numerical Examples

To benchmark our code written in Matlab, we pose a set of problems with known exact solutions. Note, all simulations were performed on a cluster. We have solve the finite element method on the surface and the errors. When approximating the partial difference equation using finite element method which the finite element subspace consisting of linear function. Since the functions is used for numerical, the approximation space completely linear over individual elements. Consequently we can choose an interpolation Iu_h that is matches the true solution at each nodes (Ern and Guermond 2013), the error $E(h)$ is calculated in H^1 semi-norm defined as follows

$$E(h) = ||\nabla_{\Gamma_h}(u - Iu_h)||_{L^2(\Gamma_h)} \tag{4.9}$$

where u is the exact solution and Iu_h be the interpolant of u.

We will have the error estimate in the first order derivative of the error which associate with the interpolant as follows

Theorem 4.5. *Let $u \in H(\Gamma)$ and let $Iu \in V_h$ be an interpolant of u , then*

$$||\nabla_{\Gamma_h}(u - Iu_h)||_{L^2(\Gamma_h)} \leq ch|u|_{H^2(\Gamma_h)} \tag{4.10}$$

Proof. The proof is in theorem 0.1 of Tuncer 2013 □

From that, we determine another quantity, which is useful in the comparisons, the so-called experimental order of convergence (EOC).

Definition 4.6. Experimental order of convergence (Jackaman et al. 2019) *Given two sequences $E(h_i)$ and $h_i \searrow 0$. The experimental order of convergence (EOC) can be defined by comparing two errors $E(h_i)$ and $E(h_{i-1})$ at different mesh size h_i and h_{i-1}*

$$EOC(i) = \frac{\log(E(h_i)/E(h_{i-1}))}{\log(h_i/h_{i-1})}. \tag{4.11}$$

Example 1 Our first example is to consider the problem

$$\Delta_\Gamma u + cu = f \tag{4.12}$$

on the unit sphere: $\Gamma = \{(x, y, z) \in \mathbb{R}^3 | x^2 + y^2 + z^2 = 1\}$.

As we have already mentioned before, we assume that there is no boundaries $\partial\Gamma = \emptyset$ on Γ. To obtain an exact solution, we set $c = 1$ and $f = 13xyz$. Then, it is not difficult to discern that the exact solution is given by $u = xyz$ (Olshanskii et al. 2012).

We start our tests with a relatively low resolution of just 66 node approximation of Γ gradually increasing the number of nodes to a maximum value 262146 to observe numerical convergence of the procedure. For each resolution, we define the largest value of the mesh size h. The results are summarised in Table 4.1 and are illustrated in Fig. 4.3 and Fig. 4.4.

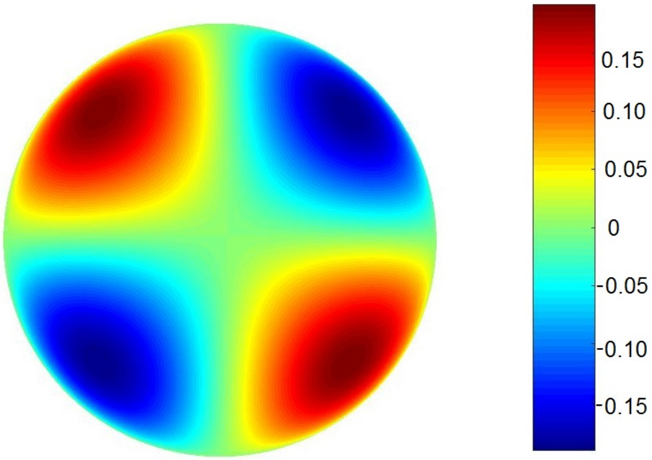

Figure 4.3: Distribution of non-dimensional pressure on the surface at 262146 node resolution. The colour bar presents the value of the reduced non-dimensional pressure.

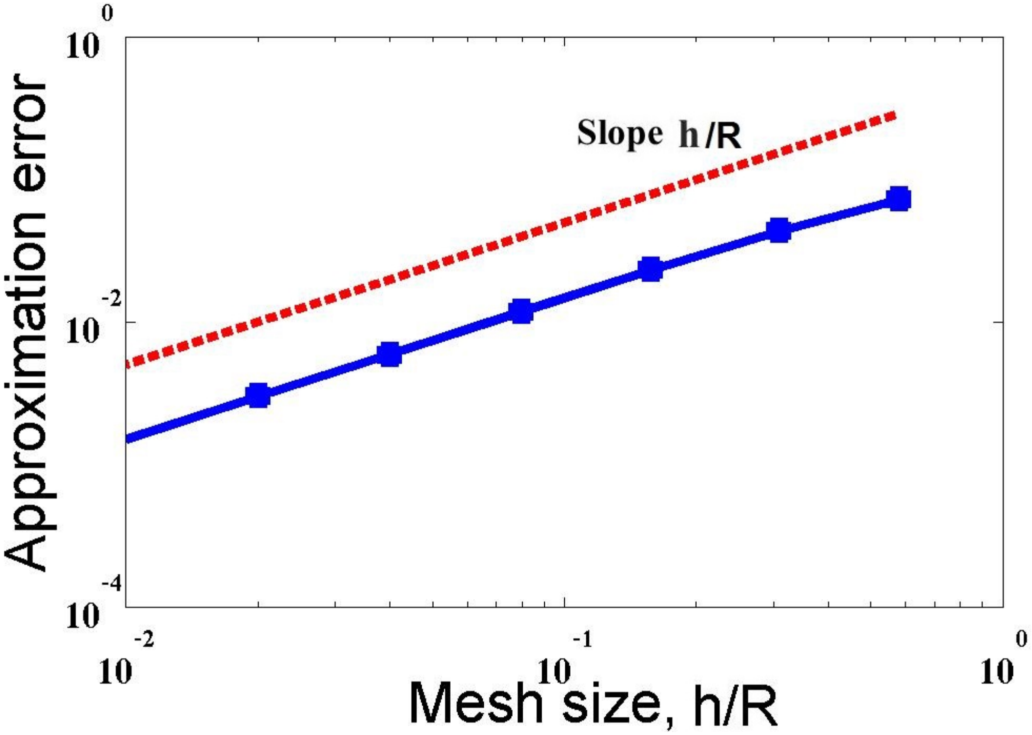

Figure 4.4: A log-log plot of the approximation error in H^1 semi-norm as a function of the non-dimensional mesh size h/R. The numerical data are shown by symbols and the dashed line is the slope error $\propto h/R$ shown for comparison.

i	n	h/R	$E(h)$	EOC
1	66	0.5792	0.0728	-
2	258	0.3088	0.0436	0.8140
3	1026	0.1577	0.0231	0.9435
4	4098	0.0795	0.0118	0.9867
5	16386	0.0399	0.0059	0.9983
6	65538	0.0200	0.0030	1.0010
7	262146	0.0100	0.0015	1.0012

Table 4.1: Results of the problem (4.12) benchmarking. Here, i is the refinement step, n is number of nodes, h/R is the non-dimensional mesh size, $E(h)$ is the error in H^1 semi-norm, see formula 4.9 and EOC is the experimental order of convergence, see formula 4.11. Notice that the results clearly show that the method is first order accurate in the H^1 semi-norm, as is also verified by theorem 4.5.

Example 2 In the second numerical example, we consider problem (4.12) but at $c = 0$. In this case

$$-\Delta_\Gamma u = f. \tag{4.13}$$

Since

$$\int_\Gamma u \, dA = 0,$$

to obtain a well-posed problem, an additional condition

$$\int_\Gamma f \, dA = 0$$

should be imposed and satisfied to guarantee existence and uniqueness of u.

For the purpose of benchmarking, we select a particular solution

$$u = \sin(\pi x)\sin(\pi y)\sin(\pi z)$$

which requires

$$f = -\nabla_\Gamma \cdot \mathbf{v}, \;\; \mathbf{v} = \nabla_\Gamma u = \nabla u - (\nabla u \cdot \mathbf{n})\mathbf{n}$$

and

$$\nabla_\Gamma \cdot \mathbf{v} = \nabla \cdot \mathbf{v} - \sum_{i=1}^{3} (\nabla v_i \cdot \mathbf{n})\mathbf{n}_i$$

where the normal vector to the surface is obviously

$$\mathbf{n}(x, y, z) = \frac{(x, y, z)}{\sqrt{x^2 + y^2 + z^2}}.$$

The results are summarised in Table 4.2 and are illustrated in Figs. 4.5 and 4.6.

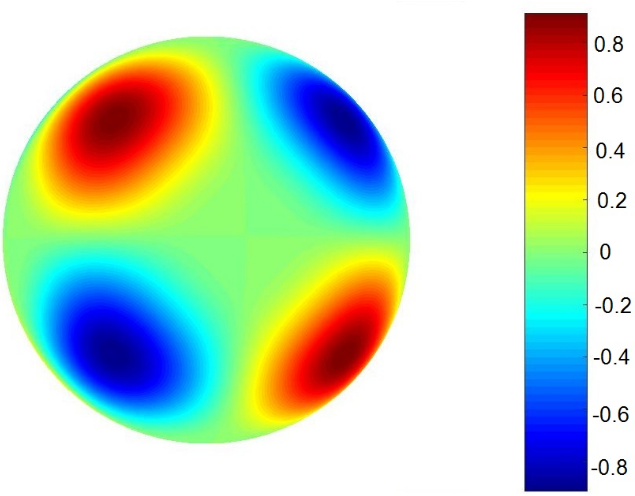

Figure 4.5: Distribution of non-dimensional pressure on the surface at 262146 nodes. The colour bar presents the value of the reduced non-dimensional pressure.

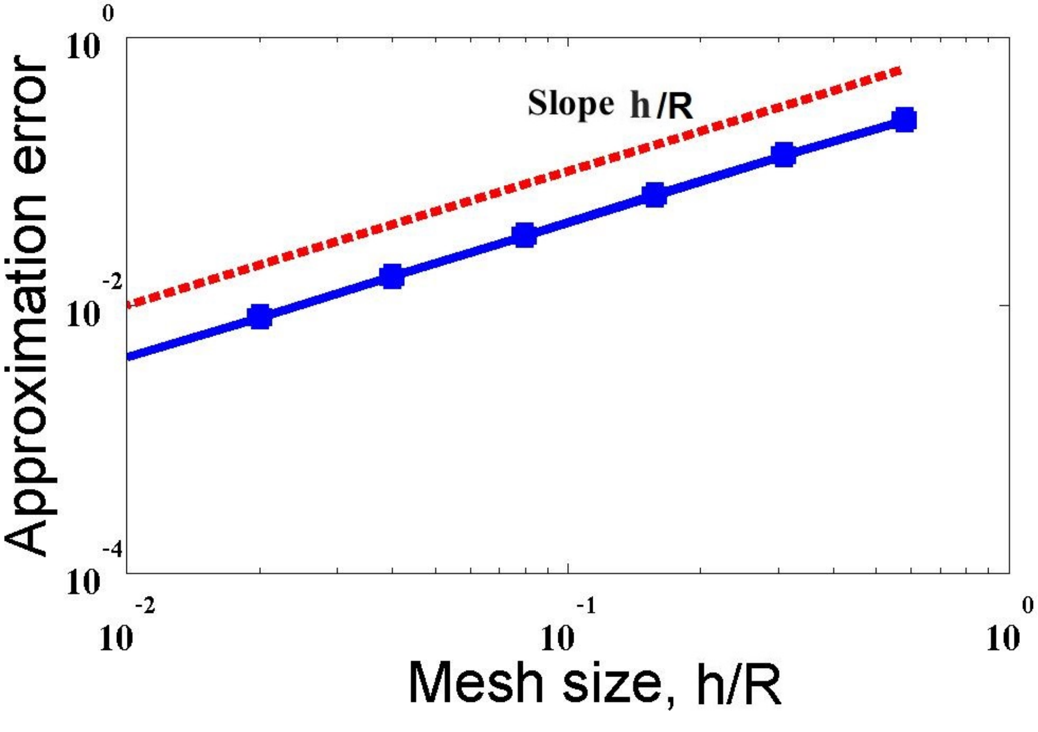

Figure 4.6: A log-log plot of the approximation error in H^1 semi-norm as a function of the non-dimensional mesh size h/R. The numerical data are shown by symbols and the dashed line is the slope error $\propto h/R$ shown for comparison.

i	n	h/R	$E(h)$	EOC	$\int_{\Gamma_h} f dA$	$\int_{\Gamma_h} u dA$
1	66	0.5792	0.2390	-	0.7300	0.0179
2	258	0.3088	0.1305	0.9622	0.1839	0.0051
3	1026	0.1577	0.0661	1.0118	0.0453	0.0013
4	4098	0.0795	0.0329	1.0200	0.0114	0.0003
5	16386	0.0399	0.0163	1.0141	0.0028	0.0001
6	65538	0.0200	0.0081	1.0077	0.0007	0.0000
7	262146	0.0100	0.0041	1.0039	0.0001	0.0000

Table 4.2: Results of the problem (4.13) benchmarking. Here, i is the refinement step, n is number of nodes, h/R is the non-dimensional mesh size, $E(h)$ is the error in H^1 semi-norm, see formula (4.9) and EOC is the experimental order of convergence, see formula 4.11. Notice that the results clearly show that the method is first order accurate in the H^1 semi-norm, as is also verified by theorem 4.5.

In conclusion, we have shown the performance of the surface finite element method by the illustration of two numerical examples. The accuracy of the method is observed by the error in H^1 semi-norm that we have as expected the first order convergence. The approximation error plots in the log-log scale are presented in Fig. 4.4 and 4.6. The results showed the approximate solutions converge accurately to the analytic solutions as the mesh size, h/R is refined. We have also computed the experimental order of convergence and show that it approaches the proven values.

Moreover, the performance of the numerical scheme will be used in the boundary value problem for the Laplace-Beltrami equation (3.2) which the detail is in the following section to determine permeability.

4.3 Dirichlet Boundary Value Problem for the Laplace–Beltrami Equation

In this section, we consider the Dirichlet boundary value problem for the Laplace–Beltrami Equation on a truncated sphere which is come from cutting a close sphere with a planes. Consequently the shape of the obtained boundary is circle with the radius $R \sin \theta_0$, R is the radius of sphere, see Fig. 4.7. For more information is given in the topic 3.2

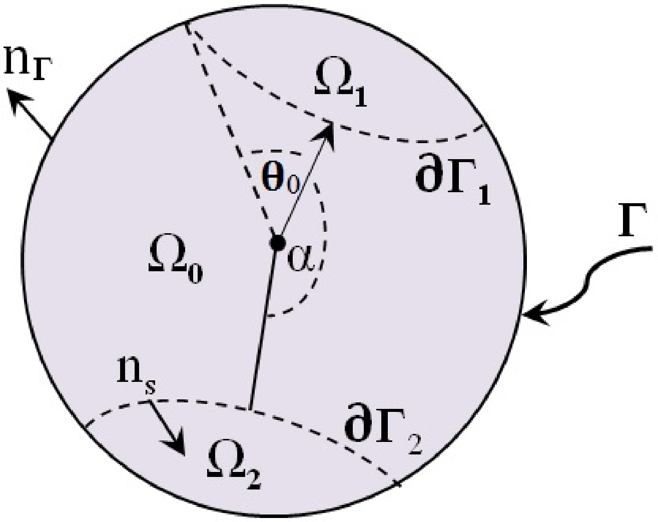

Figure 4.7: Illustration of the physical domains of the problem Ω_0, Ω_1 and Ω_2 with the boundaries $\partial\Gamma_1$ and $\partial\Gamma_2$ defined on Γ. Here, $\mathbf{n}_\Gamma$ is the unit outward normal vector to the surface Γ and $\mathbf{n}_s$ is the tangential outward normal vector to the boundaries $\partial\Gamma_{1,2}$.

This problem implies that $\partial\Gamma \neq \emptyset$. We also suppose that $c \equiv 0$ and a the source term $f \equiv 0$, that is

$$-\Delta_{\Omega_0} u = 0 \qquad \text{on } \Omega_0 \tag{4.14}$$

subject to the Dirichlet boundary conditions

$$u|_{\partial\Gamma_1} = u_1 = const \tag{4.15}$$

and

$$u|_{\partial\Gamma_2} = u_2 = const. \tag{4.16}$$

The numerical procedure to approximation weak formulation of the Laplace-Beltrami boundary value problem is expected to be similar to that applied to the benchmark problems, though the weak formulation itself needs some amendments.

4.3.1 The Laplace-Beltrami Boundary Value Problem: Weak Formulation

In this section, we are going to formulate weak forms of the Laplace-Beltrami problem (4.14) set on a truncated sphere, Fig. 4.7.

To obtain a weak form, equation (4.14) is multiplied by a test function $v \in H_0^1(\Omega_0)$ $(v|_{\partial\Gamma_1 \cup \partial\Gamma_2} = 0)$ and is integrated over the domain of the definition to obtain

$$-\int_{\Omega_0} (\Delta_{\Omega_0} u) v \, dA = 0. \tag{4.17}$$

Using the product rule for divergence and gradient operators

$$\nabla \cdot (v\nabla_{\Omega_0} u) = (\nabla_{\Omega_0} v) \cdot (\nabla_{\Omega_0} u) + v\nabla \cdot (\nabla_{\Omega_0} u), \tag{4.18}$$

(4.17) can be rewritten as follows

$$-\int_{\Omega_0} v\nabla_{\Omega_0} \cdot (\nabla_{\Omega_0} u)\, dA = \int_{\Omega_0} \Big(\nabla_{\Omega_0} v \cdot \nabla_{\Omega_0} u - \nabla_{\Omega_0} \cdot (v\nabla_{\Omega_0} u)\Big)\, dA. \tag{4.19}$$

We now apply the Green theorem to the second term on the right-hand side of the equation to obtain

$$-\int_{\Omega_0} v\nabla_{\Omega_0} \cdot (\nabla_{\Omega_0} u)\, dA = \int_{\Omega_0} \nabla_{\Omega_0} v \cdot \nabla_{\Omega_0} u\, dA - \int_{\partial\Gamma_1 \cup \partial\Gamma_2} (v\nabla_{\Omega_0} u) \cdot \mathbf{n}_{s_1}\, dl. \tag{4.20}$$

Therefore, (4.17) becomes

$$\int_{\Omega_0} \nabla_{\Omega_0} v \cdot \nabla_{\Omega_0} u\, dA - \int_{\partial\Gamma_1 \cup \partial\Gamma_2} (v\nabla_{\Omega_0} u) \cdot \mathbf{n}_{s_1}\, dl = 0. \tag{4.21}$$

The second term of (4.21) vanishes because of the choice of the test functions, so that as a net result

$$\int_{\Omega_0} \nabla_{\Omega_0} v \cdot \nabla_{\Omega_0} u\, dA = 0. \tag{4.22}$$

We then apply the boundary condition (4.15) - (4.16) to approximate the solutions by using the finite element method.

4.3.2 Numerical Examples

In the case of Dirichlet boundary conditions, we approximate the solution of the Laplace - Beltrami equation

$$\Delta_{\Omega_0} u = 0, \tag{4.23}$$

on a truncated sphere, see Fig. 4.7. We have used the Dirichlet boundary conditions ;

$$u|_{\partial\Gamma_1} = u_1 \quad \text{and} \quad u|_{\partial\Gamma_2} = u_2. \tag{4.24}$$

The results for the pressure u are presented in Fig. 4.8. In order to show the convergence of the finite element approximation, we also show the error measured in the H^1 semi-norm, see Fig. 4.9 and Table 4.3.

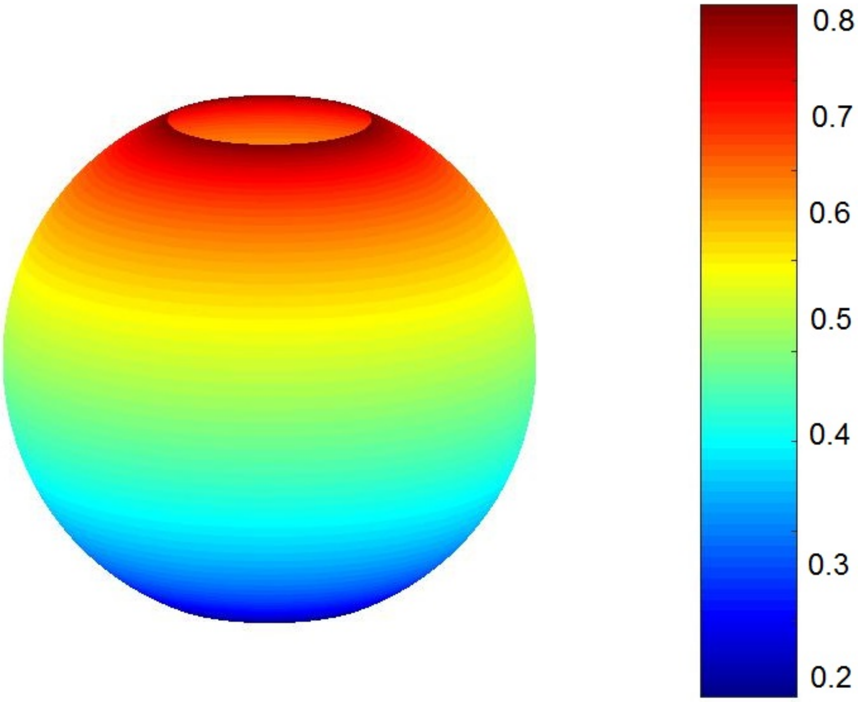

Figure 4.8: Distribution of non-dimensional pressure u/u_0 plotted on surface at 592960 nodes. The angle $\alpha = 180°$, $\theta_0 = 22.5°$. The colour bar presents value of non-dimensional pressure. Here, $u_0 = \frac{2\gamma}{R}\cos\theta_c$, θ_c is the contact angle and γ is the coefficient of the surface tension.

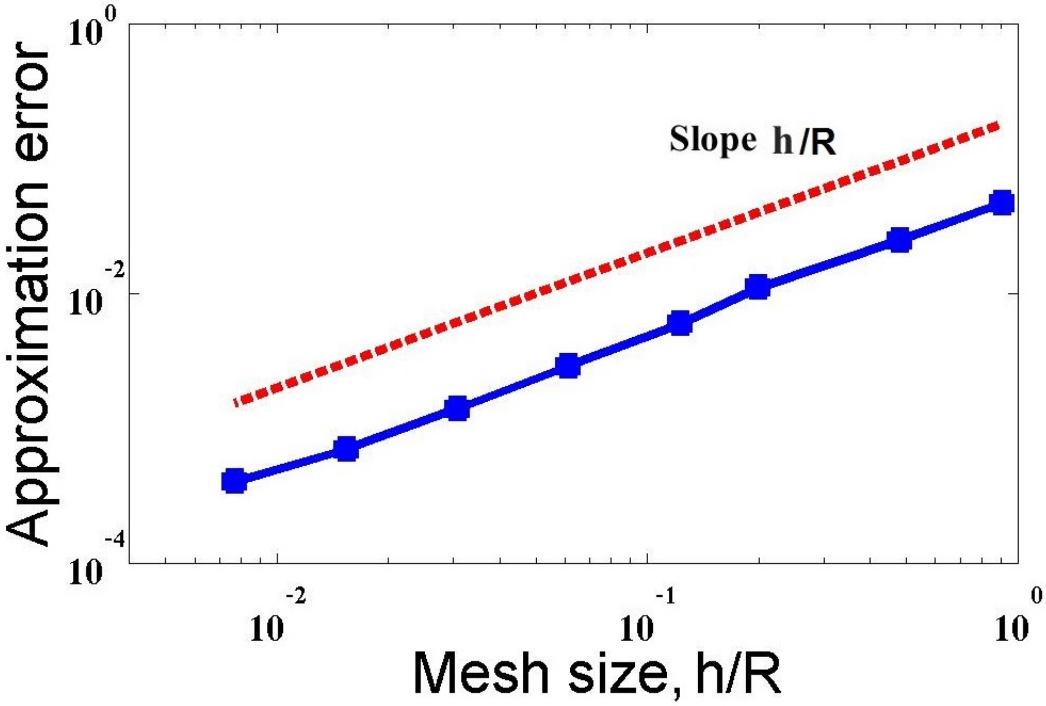

Figure 4.9: A log-log plot of the approximation error in H^1 semi-norm as a function of the mesh size h/R. The numerical data are shown by symbols and the dashed line is the slope error $\propto h/R$ shown for comparison.

i	Number of Nodes	h/R	$E(h)$	EOC
1	40	0.9078	0.0466	-
2	144	0.4815	0.0248	0.9947
3	672	0.1996	0.0110	0.9232
4	2368	0.1226	0.0059	1.2781
5	9152	0.0611	0.0029	1.0199
6	37252	0.0307	0.0014	1.0581
7	148496	0.0154	0.0007	0.9619
8	592960	0.0077	0.0004	0.9985

Table 4.3: Results for the bench-marking of one sphere problem with non-dimensional pressure on the boundaries $u_1/u_0 = 0.8$ and $u_2/u_0 = 0.2$. Here, $u_0 = \frac{2\gamma}{R}\cos\theta_c$, θ_c is the contact angle and γ is the coefficient of the surface tension, h/R is the non-dimensional mesh size, $E(h)$ is the error in H^1 semi-norm, see formula (4.9) and EOC is the experimental order of convergence, see formula (4.11). Notice that the results clearly show that the method is first order accurate in the H^1 semi-norm, as is also verified by theorem 4.5.

In this practice, the convergence of the H^1 errors as a function of the mesh size h is illustrated in Table 4.3. One can see, that the errors converge optimally, that is $EOC \approx 1$, as is expected from the order of the numerical method. One can also see in Figure 4.9, that the approximation errors in the H^1 semi norm are in decline to zero when the mesh size is decreased. Moreover, the experimental order of convergence is observed, which the values correspond to the standard norm in the error analysis. These mean that the surface finite element method is a very efficient from a computational the solutions of the Laplace-Beltrami equation.

Next, we will approximate the total flux and the surface permeability for one particle.

4.4 Surface Permeability of a Single Particle

We have used this section to demonstrate how the coefficient of permeability can be approximated by the solutions of the Laplace - Beltrami equation. In this part of our study, we consider the truncated spherical domain in case of arbitrary oriented boundaries and the arbitrary particle shapes. One can distinguish two cases. First, when the particle still has a spherical shape but the azimuthal symmetry is lost, that is the boundaries are oriented arbitrary to each other. Secondly, the particle shape may differ from the spherical shape, which is commonly the case in natural materials like sand.

4.4.1 Arbitrary Oriented Boundaries

One way to understand the coefficient of permeability is to observe the total flux as function of the angle α, so the next topic will focus on the value of total flux with respect to different positions of the boundary. In this research, the boundary $\partial\Gamma_1$ is fixed and the boundary $\partial\Gamma_2$ is rotated around x-axis, anticlockwise for α which $0 \leq \alpha \leq 180$. The examples of the domain have been shown in Fig. 4.10. Using the surface finite element method we are able to approximate the total flux and hence the permeability of the particle.

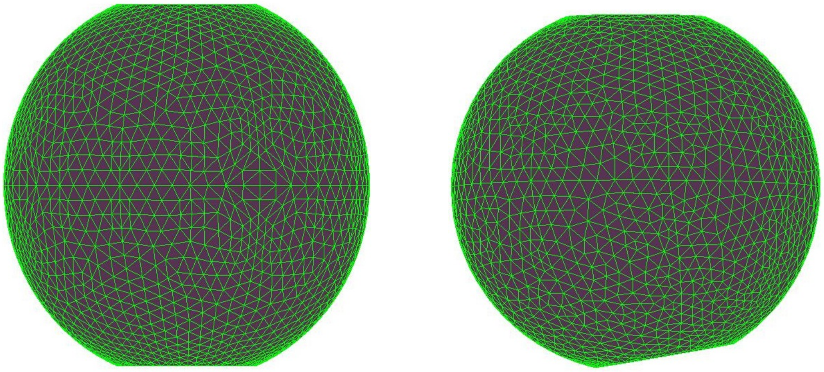

(a) $\alpha = 180°$, $N = 2368$.　(b) $\alpha = 170°$, $N = 2273$.

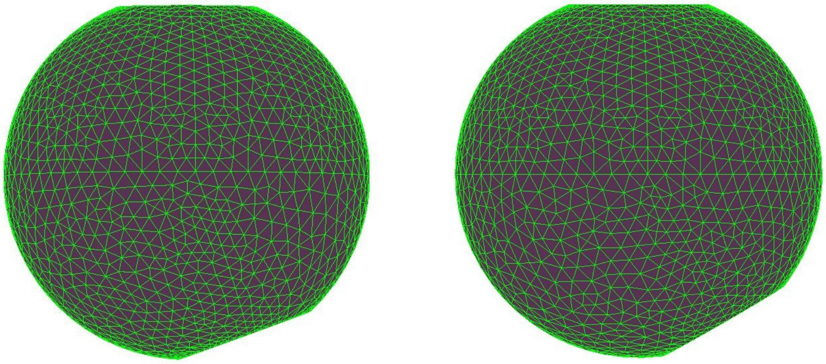

(c) $\alpha = 160°$, $N = 2082$.　(d) $\alpha = 150°$, $N = 2047$.

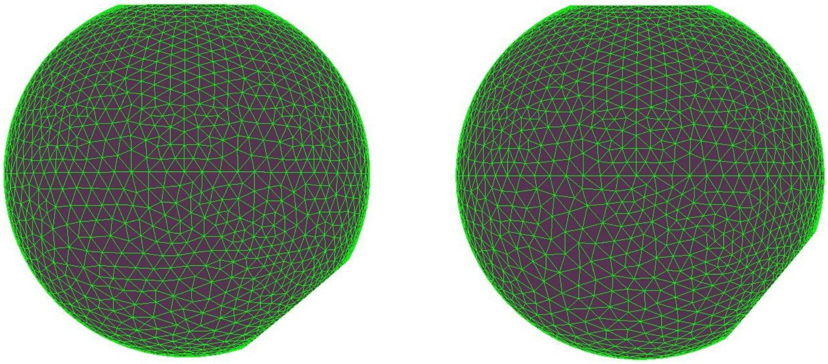

(e) $\alpha = 140°$, $N = 2133$.　(f) $\alpha = 130°$, $N = 2084$.

Figure 4.10: Illustration examples of the surface given by a truncated sphere. The examples show the different angle α with $\theta_0 = 22.5°$, see details in Fig. 4.7. N is the number of nodes.

The results have been shown for the tilt angle $\alpha = 165^\circ$ and $\alpha = 150^\circ$ in Fig. 4.11 and Fig. 4.12 respectively, where the value of the non-dimensional pressure on the boundaries are fixed at $\left.\frac{u_1}{u_0}\right|_{\partial\Gamma_1} = 0.8$ and $\left.\frac{u_2}{u_0}\right|_{\partial\Gamma_2} = 0.2$.

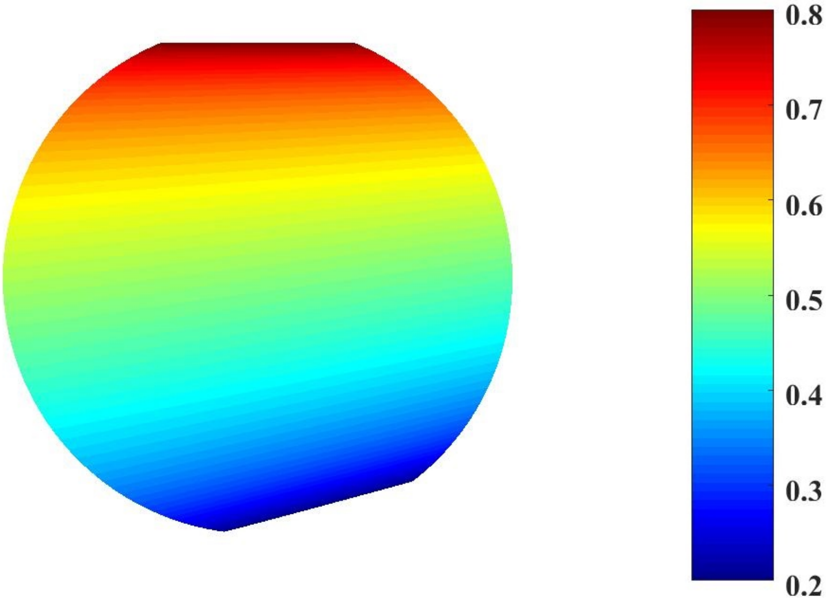

Figure 4.11: Distribution of non-dimensional pressure u/u_0 plotted on the surface using 523328 nodes resolution of the numerical method. The angle $\alpha = 165^\circ$, $\theta_0 = 22.5^\circ$ The colour bar presents value of non-dimensional pressure. Here, $u_0 = \frac{2\gamma}{R}\cos\theta_c$, θ_c is the contact angle and γ is the surface tension.

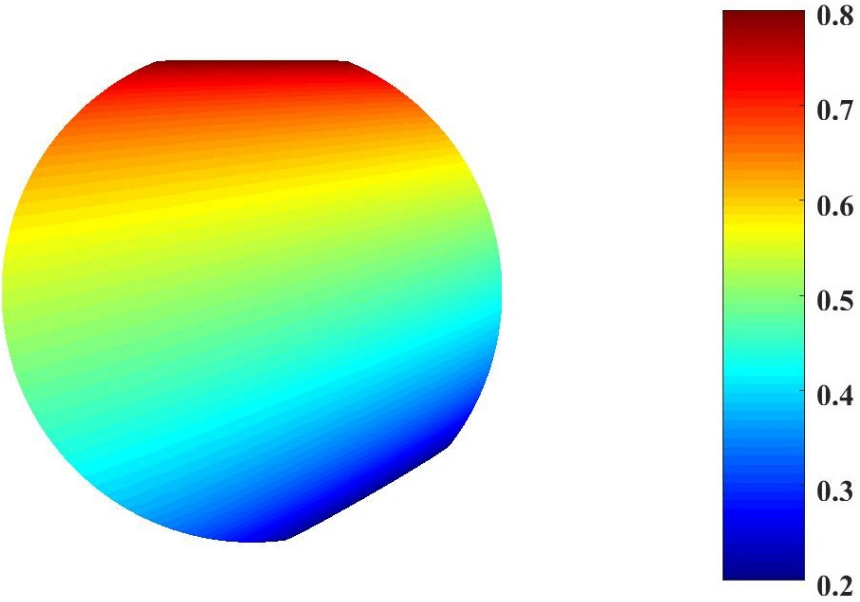

Figure 4.12: Distribution of non-dimensional pressure u/u_0 plotted on the surface using 613090 nodes resolution of the numerical method. The angle $\alpha = 150°$, $\theta_0 = 22.5°$ The colour bar presents value of non-dimensional pressure. Here, $u_0 = \frac{2\gamma}{R}\cos\theta_c$, θ_c is the contact angle and γ is the surface tension.

Now we have observed the total flux in case of arbitrary oriented boundaries, see Table 4.4.

Tilt angle α, [deg]	Total flux Q_T/Q_0	Tilt angle α, [deg]	Total flux Q_T/Q_0
75	1.5527	125	1.0882
80	1.4567	130	1.0711
85	1.3803	135	1.0562
90	1.3183	140	1.0435
95	1.2656	145	1.0327
100	1.2244	150	1.0236
105	1.1882	155	1.0161
110	1.1574	160	1.0102
115	1.1311	165	1.0055
120	1.1079	170	1.0024

Table 4.4: Non-dimensional total flux Q_T/Q_0 for one spheres problem in case of arbitrary oriented boundaries with the different tilt angle α. The value of the non-dimensional pressure on the boundaries are fixed at $u_1/u_0 = 0.8$ and $u_1/u_0 = 0.2$ on $\partial\Gamma_{(1,2)}$. Here, Q_0 is the normalized total flux in the azimuthally symmetric case, $u_0 = \frac{2\gamma}{R}\cos\theta_c$, θ_c is the contact angle and γ is the surface tension. Q_T is the dimensional total flux, see formula 3.18.

.

This table shows the values of non-dimensional total flux at the different tilt angle α between 75 degrees and 170 degrees at 5 degrees interval.

It can be seen that the value of non-dimensional total flux Q_T/Q_0 through the spherical element decrease slightly when the tilt angle α is increasing and the boundary contours move away from each other.

Next, we will take those data to examine the dependency of the total flux, and hence the permeability as a function of the tilt angle α. The graph is already illustrated in Figure 4.13.

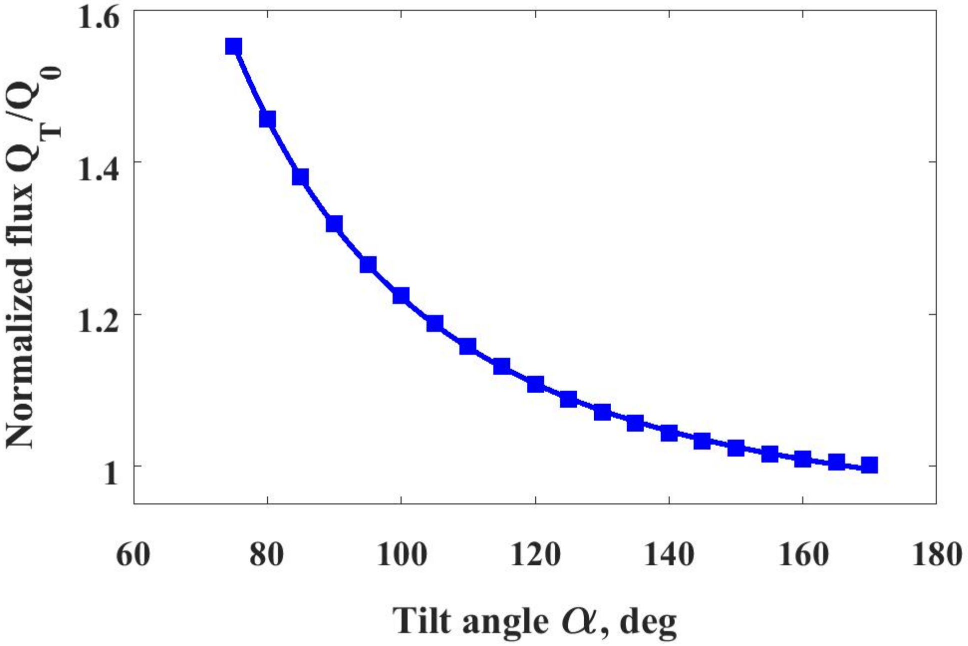

Figure 4.13: Non-dimensional total flux Q_T/Q_0 as a function of tilt angle α at fixed values of the non-dimensional pressure on the boundaries $u_1/u_0 = 0.8$ and $u_1/u_0 = 0.2$ on $\partial\Gamma_{(1,2)}$, where Q_0 is the normalized total flux in the azimuthally symmetric case, $u_0 = \frac{2\gamma}{R}\cos\theta_c$, θ_c is the contact angle and γ is the surface tension. Q_T is the dimensional total flux, see formula 3.18. The solid line is the fit to the data $Q_T/Q_0 = A\alpha^B + C$ at $A = 4.11 \times 10^4$, $B = -2.565$ and $C = 0.9183$.

The picture 4.13 presents the non-dimensional total flux Q_T/Q_0 as a function of tilt angle α set up with the value of the non-dimensional pressure on the boundaries $u_1/u_0 = 0.8$ and $u_1/u_0 = 0.2$ on $\partial\Gamma_{(1,2)}$ as is shown in Fig. 4.7. Symbols are the numerical result obtained at high resolution (maximum mesh size h/R $\approx$ 0.003). The solid line is the fit to the data $Q_T/Q_0 = A\alpha^B + C$ with $A = 4.11 \times 10^4 \pm 1.23 \times 10^4$, $B = -2.565 \pm 0.0710$ and $C = 0.9183 \pm 0.0070$.

One can conclude that at relatively large tilt angles which close to the the angle in the azimuthal symmetrical case, the liquid total flux value and hence permeability also close to that predicted on the basis of the azimuthally symmetric solution, see equation (3.19). One may notice that the value of permeability can be approximated with the accuracy 50 % for the small tilt angles (Sirimark et al. 2018b). This effect will be considered in a particle ensemble setting in Chapter 6.

Since the permeability is expected to be related with (or even proportional to) the effective length of the pathway connecting the boundary contour, we next consider the specific systematic change of the original spherical shape to understand the role of effective parameters characterising these variations.

4.4.2 Arbitrary Particle Shapes

In this section, the arbitrary particle shapes have been considered by perturbations of a sphere preserving surface smoothness. The results formed in part our recent publication (Sirimark et al. 2018b).

Based on the previous methodology, we will approximate solutions of the Laplace-Beltrami Dirichlet boundary value problem set up with perturbed particle surfaces element to calculate the liquid total flux, that is used to measure the surface permeability. We have changed the original spherical shape via the transformation $r(\theta, \phi) = R(1 + A_s \cos(m\theta)\cos(n\phi))$ at $m = n = 5$, where R is the radius of spherical, A_s is the shape perturbation amplitude, θ and ϕ are the angles in the spherical coordinate system. We keep the original boundary contours which are circular and are not perturbed. The results have been shown in Figure 4.14.

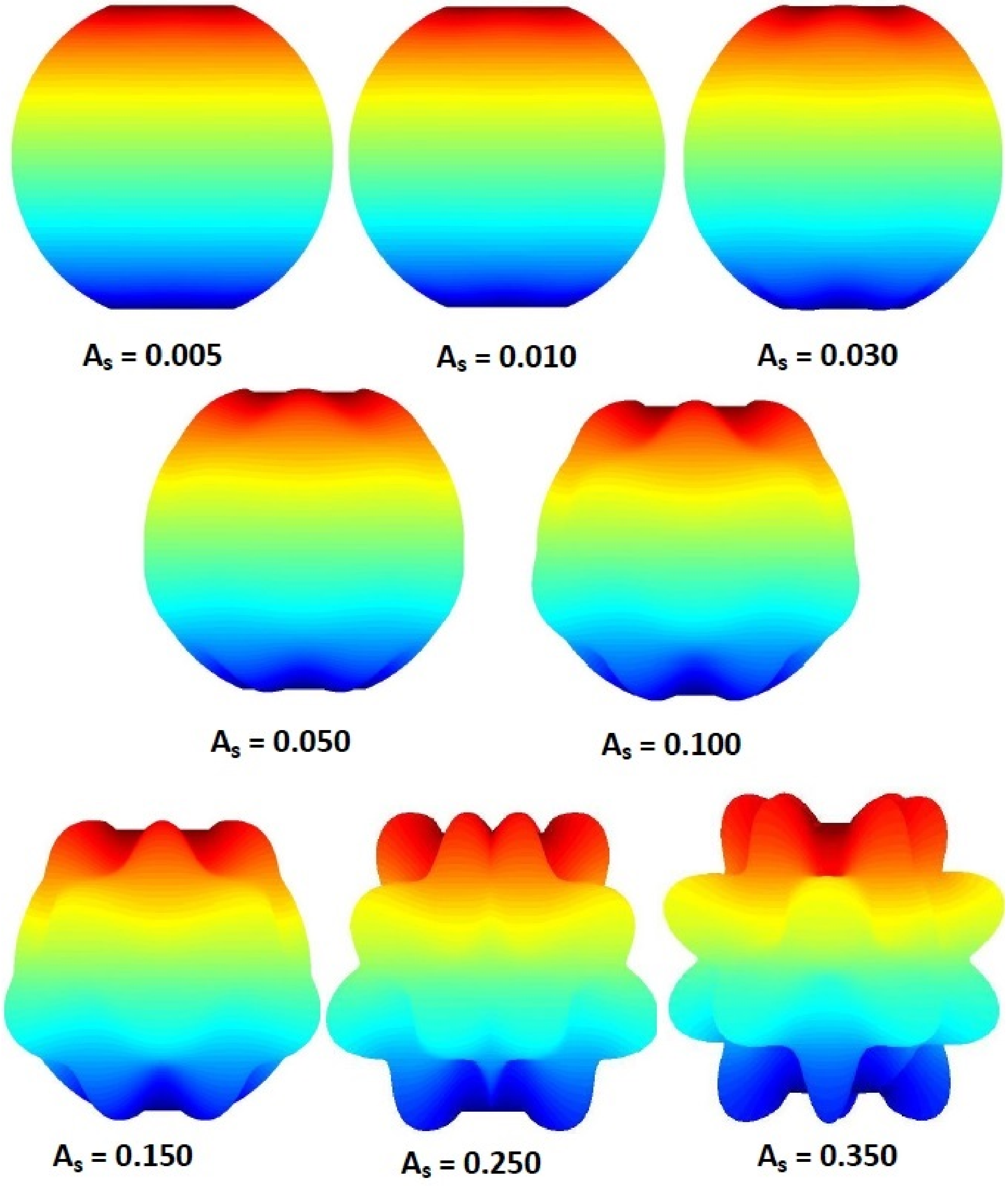

$A_s = 0.005$ $A_s = 0.010$ $A_s = 0.030$

$A_s = 0.050$ $A_s = 0.100$

$A_s = 0.150$ $A_s = 0.250$ $A_s = 0.350$

Figure 4.14: Distribution of the non-dimensional pressure u/u_0 on the truncated surfaces given by $r(\theta, \phi) = R(1 + A_s \cos(m\theta) \cos(n\phi)$ at $m = n = 5$ and different A_s, as is shown in the figure, with identical circular boundary contours at $u_1/u_0 = 0.8, u_2/u_0 = 0.2, \theta_0 = 22.5°$ and $\alpha = 180°$. The colour scheme represents the value of the non-dimensional pressure, as in Fig. 4.12. Here, $u_0 = \frac{2\gamma}{R} \cos\theta_c$, θ_c is the contact angle and γ is the surface tension of the liquid.

Next, we show how the perturbation of the spherical shape have an effect on the liquid total flux, and hence permeability. The results are given in the Table 4.5.

Amplitude A_s	Total flux Q_T/Q_0	Amplitude A_s	Total flux Q_T/Q_0
0.005	0.9960	0.100	0.9793
0.010	0.9948	0.150	0.9637
0.030	0.9900	0.250	0.9037
0.050	0.9869	0.350	0.8254

Table 4.5: Non-dimensional total flux Q_T/Q_0 in case of arbitrary particle shapes with different amplitudes A_s. The values of the non-dimensional capillary pressure on the boundaries are fixed at $u_1/u_0 = 0.8$ and $u_1/u_0 = 0.2$ on $\partial\Gamma_{(1,2)}$. Here Q_0 is the total flux value through the unperturbed spherical element in similar conditions, $u_0 = \frac{2\gamma}{R}\cos\theta_c$, θ_c is the contact angle and γ is the surface tension. Q_T is the dimensional total flux, see formula 3.18.

.

We now consider the characteristic arc length scale L_p which can be estimated by means of

$$\frac{Q_T}{Q_0} \approx \frac{L_P}{(\pi - 2\theta_0)R} \approx 1 + \frac{A_s^2 m^2}{8}, \tag{4.25}$$

at $A_s^2 m^2 \ll 1$. The estimate of the characteristic arc length scale L_P of the perturbed shape can be defined along the meridian line ($\phi = const$) taking into account that $A_s^2 m^2 \ll 1$ and considering the averaging in the azimuthal direction, we obtain the formula,

$$L_P = \int_{\theta_0}^{\pi-\theta_0} \sqrt{1 + \frac{1}{R^2}\left(\frac{\partial r}{\partial \theta}\right)^2} R d\theta$$

$$
\begin{aligned}
&= \int_{\theta_0}^{\pi-\theta_0} \sqrt{1 + A_s^2 m^2 \sin^2(m\theta)\cos^2(n\phi)} R d\theta \\
&= \int_{\theta_0}^{\pi-\theta_0} \sqrt{1 + A_s^2 m^2 \frac{(1-\cos(2m\theta))}{2}\frac{(1+\cos(2n\phi))}{2}} R d\theta \\
&= \int_{\theta_0}^{\pi-\theta_0} \sqrt{1 + \frac{A_s^2 m^2}{4}(1-\cos(2m\theta))(1+\cos(2n\phi))} R d\theta \\
&\approx \int_{\theta_0}^{\pi-\theta_0} \left\{1 + \frac{A_s^2 m^2}{8}(1-\cos(2m\theta))(1+\cos(2n\phi))\right\} R d\theta.
\end{aligned}
$$

That is after averaging over the azimuthal angle and neglecting the term of $\frac{\sin\theta_0}{2m} \ll 1$. Therefore, we obtain

$$
L_P \approx \left\{ \int_{\theta_0}^{\pi-\theta_0} \left\{1 + \frac{A_s^2 m^2}{8}(1-\cos(2m\theta))\right\} R d\theta \right.
$$

and

$$
L_P \approx (\pi - 2\theta_0) R \left\{1 + \frac{A_s^2 m^2}{8}\right\}.
$$

Since it is expected that the total volume flux is proportional to the pressure gradient, one can anticipate that it depends on the effective arc length. From this assumption, we have

$$
\frac{Q_T}{Q_0} \approx \frac{(\pi - 2\theta_0)R}{L_P} \approx 1 - \frac{A_s^2 m^2}{8}. \tag{4.26}
$$

To understand the effective pathway length scale, we now consider the dependency of the total flux through such elements with the amplitude of perturbation A_s as shown in Fig. 4.15.

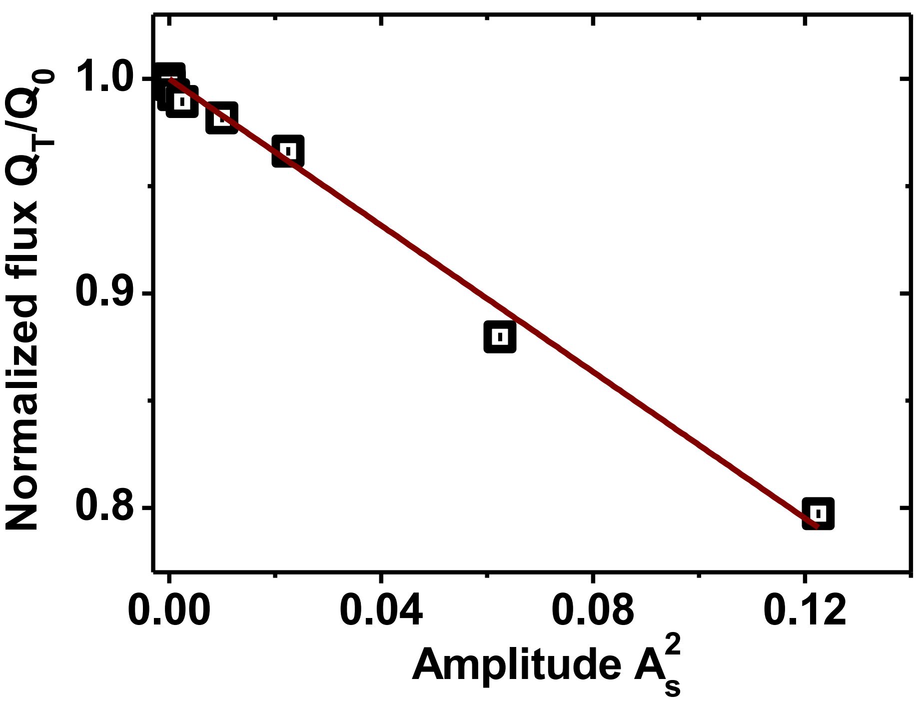

Figure 4.15: Non-dimensional total flux Q_T/Q_0 as a function of the shape perturbation amplitude A_s^2 at fixed values of $u_1/u_0 = 0.8$ and $u_1/u_0 = 0.2$ on $\partial\Gamma_{(1,2)}$, $\alpha = \pi$, $m = n = 5$ and $\theta_0 = \theta_1 = \pi/8$. Here Q_0 is the total flux value through the unperturbed spherical element in similar conditions. Q_T is the dimensional total flux, see formula 3.18. The numerical results obtained at medium resolution (maximum mesh size $h/R \approx 0.01$) are shown by symbols and the solid line is the best fit $Q_T/Q_0 = 1 - B_s A_s^2$ at $B_s = 1.7$.

The graph shows the dependency of the total flux and hence the permeability as a function of the amplitude A_s^2. It is related with the arc length L_P, equation (4.26). The simulations are performed at the medium resolution, $h/R \approx 0.01$ set up with the value of the non-dimensional capillary pressure on the boundaries, $u_1/u_0 = 0.8$ and $u_1/u_0 = 0.2$ on $\partial\Gamma_{(1,2)}$. Symbols are the results of averaging the liquid total flux averaging and the solid line is the best fit to the data
$\dfrac{Q_T}{Q_0} = 1 - B_s A_s^2$ at $B_s = 1.7$.

From the line graph, one can see that the match is not perfect because we have obtained the value of $B_s \approx 1.7$, while the expected value would be $B_s \approx \dfrac{m^2}{8} \approx 3.1$. This implies that the problem of surface diffusion over uneven landscapes is more complicated phenomenon than the simple scaling which is suggested by the effective path way length. We note that the effective parameter L_P cannot be estimated in the simple way. One need to consider the problem over strongly different surface profile with the large areas inaccessible to the liquid flow (Sirimark et al. 2018b).

In conclusion, we demonstrated how the coefficient of permeability of a porous matrix element can be estimated from the weak solution of the Laplace-Beltrami equation obtained by the FEM method. We have benchmarked the methodology using the simplest case of a single sphere without an internal boundary. We have then analyzed several cases of arbitrary particle shapes and arbitrary oriented boundaries. The methodology developed in this chapter can be used in practical application with more elements involved. This will be the subject in Chapters 5 and 6.

Chapter 5

The Laplace-Beltrami Problem in Coupled Domains

We present in this chapter the Laplace-Beltrami problem in two coupled domains using the finite element method. The key idea is quite similar to the Laplace-Beltrami problem on a single spherical surface, which is explained in the previous chapter, but now we have two domains with the continuity of pressure and the total flux on the boundary of internal sub-domains. The coupled-sphere problem is stated in Chapter 3, see 3.2.2. In order to ensure that the numerical method behaves with optimal efficiency in this case with modified boundary conditions, we verify the numerical results on a model problem with a known analytical solution (3.32)-(3.33) by checking the convergence of the numerical method. In this part, the experimental order of convergence (EOC) is calculated, as before, by means of (4.11).

5.1 The Problem in Two Coupled Domains

We consider the problem of two particles coupled through the "common" boundaries $\partial\Gamma_1^{(2)}$ and $\partial\Gamma_2^{(2)}$, as is shown in Fig. 3.3.

We are solving the following Laplace - Beltrami problem

$$-\Delta_{\Omega_0^{(1)}} u_1 = 0 \tag{5.1}$$

and

$$-\Delta_{\Omega_0^{(2)}} u_2 = 0, \tag{5.2}$$

with Dirichlet boundary conditions

$$u_1|_{\partial\Gamma_1^{(1)}} = \alpha_1 \quad \text{and} \quad u_2|_{\partial\Gamma_2^{(1)}} = \alpha_2 \tag{5.3}$$

and two continuity conditions due to the conservation of mass

$$u_1|_{\partial\Gamma_1^{(2)}} = u_2|_{\partial\Gamma_2^{(2)}} = const \tag{5.4}$$

and

$$\oint_{\partial\Gamma_1^{(2)}} \nabla u_1 \cdot \mathbf{n}_{s_1}|_{\partial\Gamma_1^{(2)}}\, dl = -\oint_{\partial\Gamma_2^{(2)}} \nabla u_2 \cdot \mathbf{n}_{s_2}|_{\partial\Gamma_2^{(2)}}\, dl, \tag{5.5}$$

where α_1 and α_2 are some real constants.

Next, the weak formulation of the mathematical model will be derived for the numerical analysis.

5.1.1 The Laplace-Beltrami Coupled Boundary Value Problem: Weak Formulation

In this section, we are going to describe the weak formulation of the coupled Laplace-Beltrami boundary value problem (5.1)-(5.2) set on the truncated spheres, which will be later solved numerically by the surface finite element method using the Galerkin formulation. We define the surface $\Omega_0^{(1)}$ and $\Omega_0^{(2)}$ as truncated spheres, shown in Fig. 3.3.

As before, Chapter 4, equation (5.1) is multiplied by a test function $v_1 \in H_0^1(\Omega_0^{(1)})$ and equation (5.2) is multiplied by $v_2 \in H_0^1(\Omega_0^{(2)})$ ($v_1|_{\partial\Gamma_1^{(1)} \cup \partial\Gamma_1^{(2)}} = 0$ and $v_2|_{\partial\Gamma_2^{(1)} \cup \partial\Gamma_2^{(2)}} = 0$) to get the weak form. We integrate over the domains to obtain

$$-\int_{\Omega_0^{(1)}} (\Delta_{\Omega_0^{(1)}} u_1) v_1 \, dA = 0 \qquad \text{on } \Omega_0^{(1)}, \tag{5.6}$$

$$-\int_{\Omega_0^{(2)}} (\Delta_{\Omega_0^{(2)}} u_2) v_2 \, dA = 0 \qquad \text{on } \Omega_0^{(2)}. \tag{5.7}$$

Using the product rule for divergence and gradient operators

$$\nabla \cdot (v \nabla u) = (\nabla v) \cdot (\nabla u) + v \nabla \cdot (\nabla u), \tag{5.8}$$

(5.6) and (5.7) can be rewritten as follows

$$-\int_{\Omega_0^{(1)}} v_1 \nabla_{\Omega_0^{(1)}} \cdot (\nabla_{\Omega_0^{(1)}} u_1) \, dA = \int_{\Omega_0^{(1)}} \Big(\nabla_{\Omega_0^{(1)}} v_1 \cdot \nabla_{\Omega_0^{(1)}} u_1 - \nabla_{\Omega_0^{(1)}} \cdot (v_1 \nabla_{\Omega_0^{(1)}} u_1) \Big) \, dA \tag{5.9}$$

and

$$-\int_{\Omega_0^{(2)}} v_2 \nabla_{\Omega_0^{(2)}} \cdot (\nabla_{\Omega_0^{(2)}} u_2)\, dA = \int_{\Omega_0^{(2)}} \Big(\nabla_{\Omega_0^{(2)}} v_2 \cdot \nabla_{\Omega_0^{(2)}} u_2 - \nabla_{\Omega_0^{(2)}} \cdot (v_2 \nabla_{\Omega_0^{(2)}} u_2) \Big)\, dA. \tag{5.10}$$

We now apply the Green theorem to the second term on the right-hand side of the both equations to obtain

$$-\int_{\Omega_0^{(1)}} v_1 \nabla_{\Omega_0^{(1)}} \cdot (\nabla_{\Omega_0^{(1)}} u_1)\, dA = \int_{\Omega_0^{(1)}} \nabla_{\Omega_0^{(1)}} v_1 \cdot \nabla_{\Omega_0^{(1)}} u_1\, dA - \int_{\partial\Gamma_1^{(1)} \cup \partial\Gamma_1^{(2)}} (v_1 \nabla_{\Omega_0^{(1)}} u_1) \cdot \mathbf{n}_{s_1}\, dl, \tag{5.11}$$

and

$$-\int_{\Omega_0^{(2)}} v_2 \nabla_{\Omega_0^{(2)}} \cdot (\nabla_{\Omega_0^{(2)}} u_2)\, dA = \int_{\Omega_0^{(2)}} \nabla_{\Omega_0^{(2)}} v_2 \cdot \nabla_{\Omega_0^{(2)}} u_2\, dA - \int_{\partial\Gamma_2^{(1)} \cup \partial\Gamma_2^{(2)}} (v_2 \nabla_{\Omega_0^{(2)}} u_2) \cdot \mathbf{n}_{s_2}\, dl. \tag{5.12}$$

Therefore, (5.6) and (5.7) become

$$\int_{\Omega_0^{(1)}} \nabla_{\Omega_0^{(1)}} v_1 \cdot \nabla_{\Omega_0^{(1)}} u_1\, dA - \int_{\partial\Gamma_1^{(1)} \cup \partial\Gamma_1^{(2)}} (v_1 \nabla_{\Omega_0^{(1)}} u_1) \cdot \mathbf{n}_{s_1}\, dl = 0, \tag{5.13}$$

and

$$\int_{\Omega_0^{(2)}} \nabla_{\Omega_0^{(2)}} v_2 \cdot \nabla_{\Omega_0^{(2)}} u_2\, dA - \int_{\partial\Gamma_2^{(1)} \cup \partial\Gamma_2^{(2)}} (v_2 \nabla_{\Omega_0^{(2)}} u_2) \cdot \mathbf{n}_{s_2}\, dl = 0. \tag{5.14}$$

The second terms in (5.13) and (5.14) vanish because of the choice of the test functions, so that as a net result

$$\int_{\Omega_0^{(1)}} \nabla_{\Omega_0^{(1)}} v_1 \cdot \nabla_{\Omega_0^{(1)}} u_1\, dA = 0, \tag{5.15}$$

and

$$\int_{\Omega_0^{(2)}} \nabla_{\Omega_0^{(2)}} v_2 \cdot \nabla_{\Omega_0^{(2)}} u_2 \, dA = 0. \tag{5.16}$$

We then apply the boundary condition (5.3) - (5.5) to find the solutions by using the finite element method.

5.1.2 Numerical Examples

Here, the surface finite element approximation to the Laplace-Beltrami problem in two coupled domains, see Fig. 5.1, corresponding to the equation (5.1)-(5.5) will be presented. In all examples, the linear finite element discretisation has been used. The experimental order of convergence is calculated by (4.11).

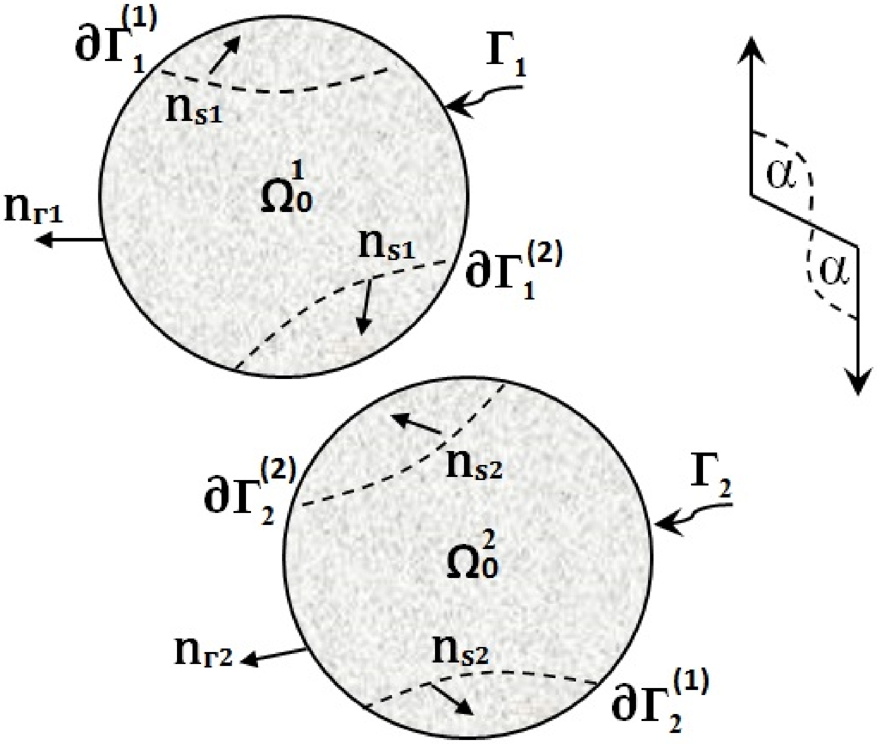

Figure 5.1: Illustration of the domains of two coupled particles. The flow domains are designated by Γ_1 and Γ_2 with the smooth boundary contours $\partial\Gamma_1^{(1)}$, $\partial\Gamma_1^{(2)}$, $\partial\Gamma_2^{(1)}$ and $\partial\Gamma_2^{(2)}$ respectively. Here, α is an angle between boundaries, $\mathbf{n}_{\Gamma_j}$ are the outward unit normal vectors to Γ_j and $\mathbf{n}_{s_j}$ are the outward unit tangential normal vectors to the boundary contours on Γ_1 and Γ_2 respectively.

The presentation of the simulation will be split between two case : one with the azimuthal symmetrical case, one with the case of arbitrary oriented boundaries. The numerical examples are illustrated next topic.

5.1.2.1 The Azimuthal Symmetrical Case in Coupled Domains

To start with the first example, we solve the Laplace - Beltrami equation (5.1)-(5.5) on two spherical domains. The methodology formulated in Chapter 4 is used to approximate the solutions of the Laplace -Beltrami. To obtain the exact solution 3.32-3.33, we have described in chapter 3 topic 3.2.5

We start our tests with a relatively low resolution of just 80 node approximation of Γ gradually increasing the number of nodes to a maximum value 296992 to observe numerical convergence of the procedure. For each resolution, we define the largest value of the mesh size h/R. The results of non-dimensional pressure are presented in Fig. 5.2. In order to show the convergence of the finite element approximation, we also show the error measured in the H^1 semi-norm, formula (4.9), see Fig. 5.3 and the and Table 5.1.

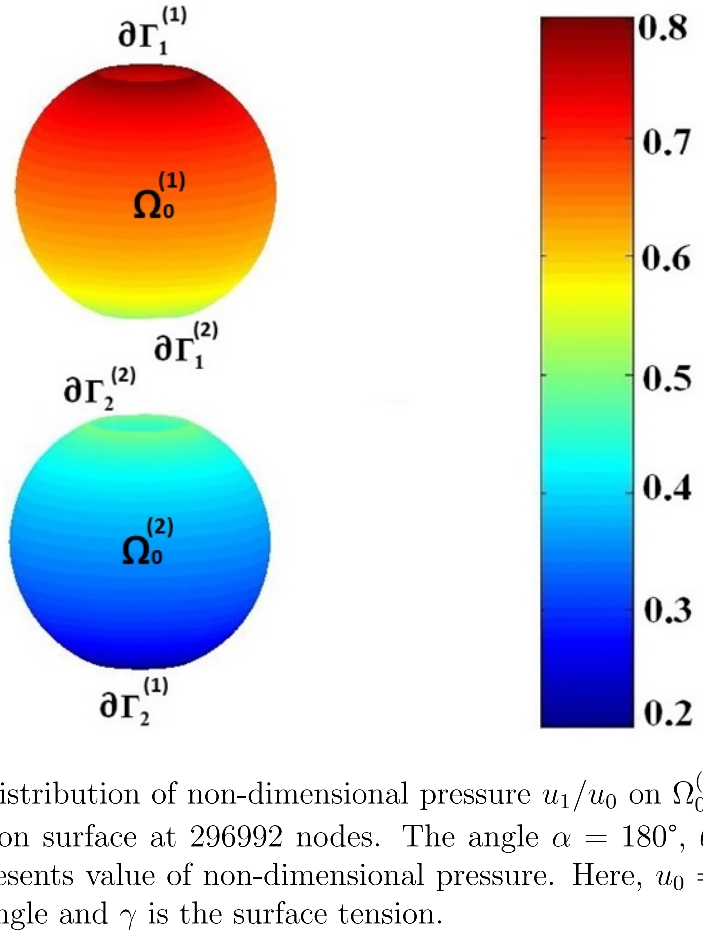

Figure 5.2: Distribution of non-dimensional pressure u_1/u_0 on $\Omega_0^{(1)}$ and u_2/u_0 on $\Omega_0^{(2)}$, plotted on surface at 296992 nodes. The angle $\alpha = 180°$, $\theta_0 = 22.5°$. The colour bar presents value of non-dimensional pressure. Here, $u_0 = \frac{2\gamma}{R}\cos\theta_c$, θ_c is the contact angle and γ is the surface tension.

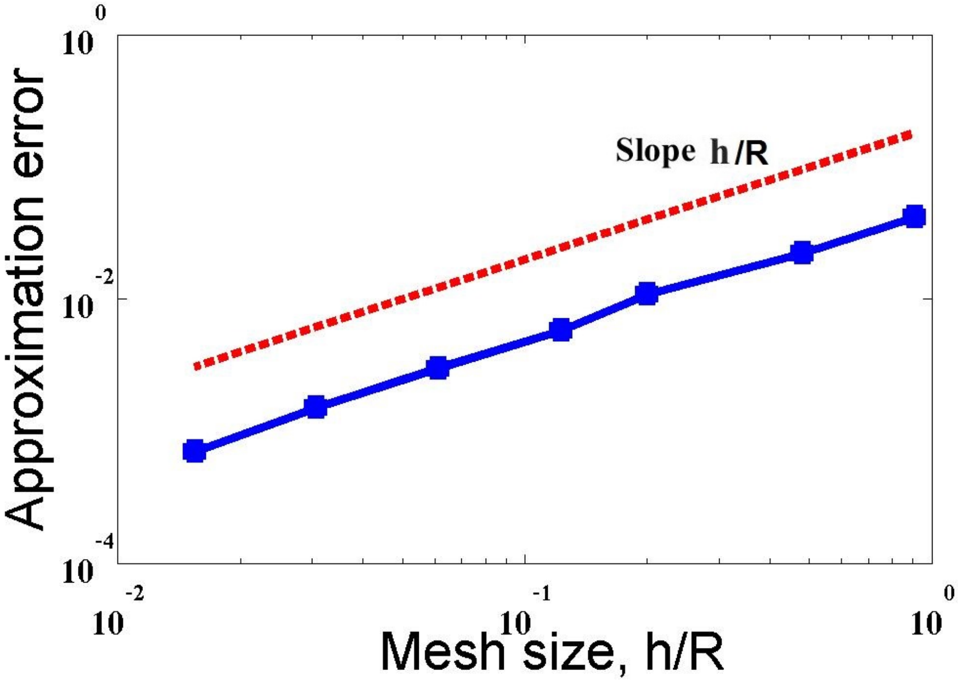

Figure 5.3: A log-log plot of the approximation error in H^1 semi-norm as a function of the mesh size h/R. The numerical data are shown by symbols and the dashed line is the slope error $\propto h/R$ shown for comparison.

i	n	h/R	$E(h)$	EOC
1	80	0.9078	0.0415	-
2	288	0.4815	0.0221	0.9929
3	1344	0.1996	0.0109	0.8048
4	4736	0.1226	0.0058	1.2812
5	18304	0.0611	0.0030	0.9694
6	74504	0.0307	0.0015	1.0076
7	296992	0.0154	0.0007	1.0176

Table 5.1: Results of the problem (5.1)-(5.5) benchmarking. Here, i is the refinement step, n is number of nodes, h/R is the non-dimensional mesh size, $E(h)$ is the error in H^1 semi-norm, see formula (4.9) and EOC is the experimental order of convergence which is defined in (4.11). Notice, that the results clearly show that the method is first order accurate in the H^1 semi-norm, as is also verified by theorem 4.5.

In this practice, we have approximated the solutions of the Laplace-Beltrami equation with coupled domains. The accuracy of the method is observed by the error in H^1 semi-norm which are shown in Table 5.1. It has been illustrated that the value of the errors converge optimally. Moreover, the approximation error plots in the log-log scale are presented in Fig. 5.3. The results showed the approximate solutions converge accurately to the analytic solutions as the mesh size, h/R is refined. We have also computed the experimental order of convergence and show that it approaches the values as we expected. These mean that the surface finite element method is very efficient for solving the solutions of the Laplace-Beltrami equation on the connected domains.

Next examples, we will present the solution in case of arbitrary oriented boundaries.

5.1.2.2 The Case of Arbitrary Oriented Boundaries in Coupled Domains

One way to understand the coefficient of permeability in case of the two connected domain is to observe the total flux as function of the angle α, so the next topic will focus on the value of total flux with respect to different positions of the boundary. In this work, the boundary $\partial\Gamma_1^{(1)}$ and $\partial\Gamma_2^{(1)}$ are fixed while the boundary $\partial\Gamma_1^{(2)}$ and $\partial\Gamma_2^{(2)}$ are rotated around x-axis, anticlockwise for α which $0 \leq \alpha \leq 180^\circ$. The examples of the domain have been shown in Fig. 5.1.

Using the surface finite element method to solve the system of the Laplace -Beltrami equations on truncated spheres we are able to find out the total flux and hence the permeability of the particles. The results are given for the angle $\alpha = 170^\circ$ and $\alpha = 135^\circ$ in Fig. 5.4 and Fig. 5.5 respectively. Here, the value of non-dimensional pressure on the boundaries are fixed at $\alpha_1/u_0 = 0.8$ and $\alpha_2/u_0 = 0.2$ on $\partial\Gamma_{(1,2)}^{(1)}$.

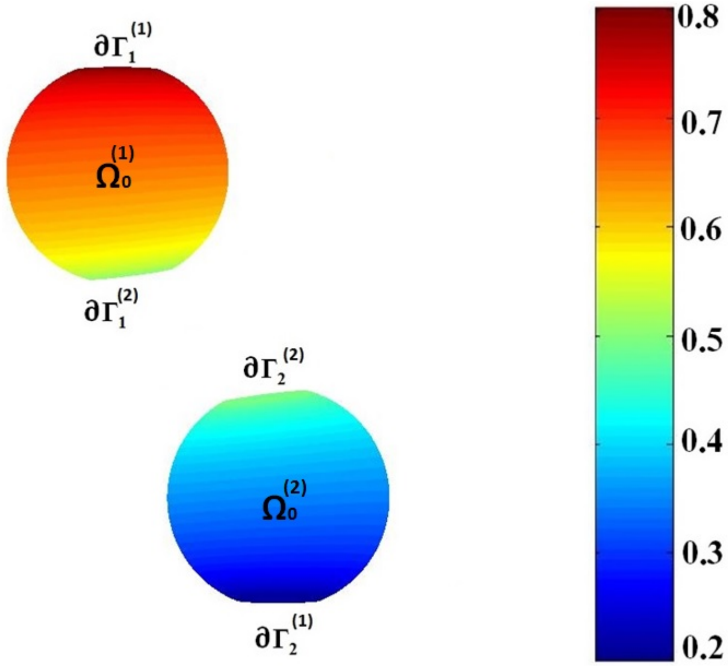

Figure 5.4: Distribution of non-dimensional pressure u_1/u_0 on $\Omega_0^{(1)}$ and u_2/u_0 on $\Omega_0^{(2)}$, plotted on surface at 289082 nodes. The angle $\alpha = 170°$, $\theta_0 = 22.5°$. The colour bar presents the value of non-dimensional pressure. Here, $u_0 = \frac{2\gamma}{R}\cos\theta_c$, θ_c is the contact angle and γ is the surface tension.

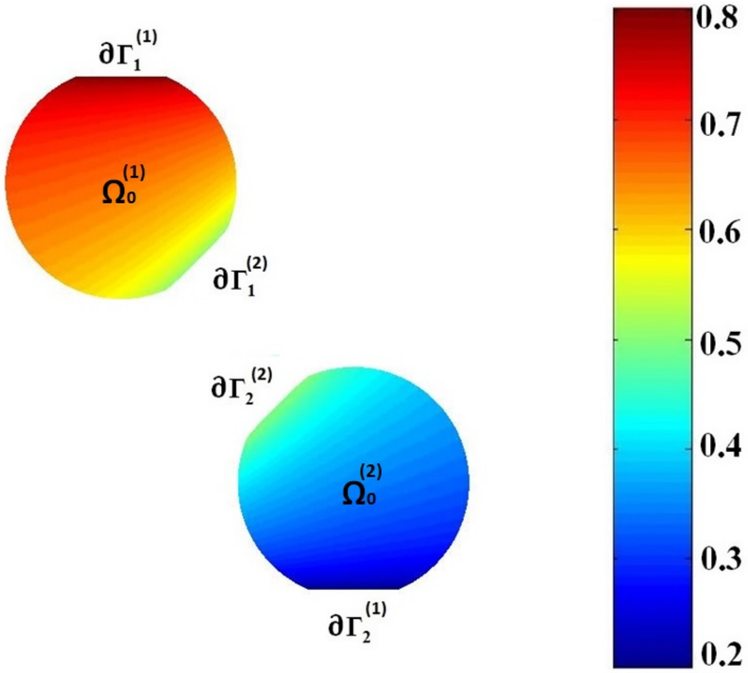

Figure 5.5: Distribution of non-dimensional pressure u_1/u_0 on $\Omega_0^{(1)}$ and u_2/u_0 on $\Omega_0^{(2)}$, plotted on surface at 289082 nodes. The angle $\alpha = 170°$, $\theta_0 = 22.5°$. The colour bar presents value of non-dimensional pressure. Here, $u_0 = \frac{2\gamma}{R}\cos\theta_c$, θ_c is the contact angle and γ is the surface tension.

Next we have observed the total flux in case of arbitrary oriented boundaries for two coupled domains, see Table 5.2.

Angle α, [deg]	Total flux, Q_T/Q_0	Angle α, [deg]	Total flux, Q_T/Q_0
75	1.5619	125	1.0881
80	1.4657	130	1.0711
85	1.3896	135	1.0561
90	1.3280	140	1.0454
95	1.2772	145	1.0343
100	1.2346	150	1.0255
105	1.1940	155	1.0167
110	1.1680	160	1.0072
115	1.1311	165	1.0024
120	1.1080	170	1.0022

Table 5.2: Tabulated values of the non-dimensional liquid total flux Q_T/Q_0 in case of arbitrary oriented boundaries for two coupled domains with the different tilt angle α. The value of the non-dimensional capillary pressure on the boundaries are fixed at $\alpha_1/u_0 = 0.8$ and $\alpha_2/u_0 = 0.2$ on $\partial\Gamma^{(1)}_{(1,2)}$. The data are from triangulation level 7 (the maximum mesh size $h/R \approx 0.018$). Here, Q_0 is the normalized total flux in the azimuthally symmetric case, $u_0 = \frac{2\gamma}{R}\cos\theta_c$, θ_c is the contact angle and γ is the surface tension.

This table shows the values of total flux at the different tilt angle α from 135 degrees to 75 degrees at 170 degrees interval.

If we look at the data on the table, we can see the value of the non-dimensional liquid total flux Q_T/Q_0 drops that result in the increasing the tilt angle α, and the boundary contours at the connected domains move away from each other. In order to understand the overall trend in data, we now show the dependence of the total flux, and hence the permeability as a function of the tilt angle α in case of two coupled domains. The graph is already illustrated in Figure 5.6.

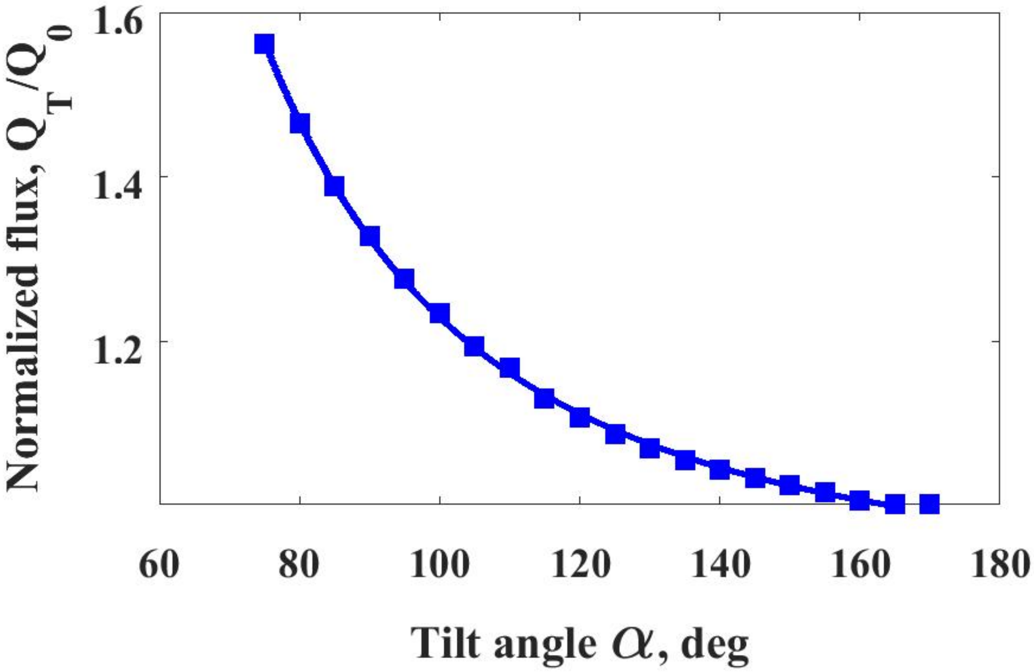

Figure 5.6: Non-dimensional total flux Q_T/Q_0 as a function of the tilt angle α at the fixed values of pressure on the boundaries, $\alpha_1/u_0 = 0.8$ and $\alpha_2/u_0 = 0.2$ on $\partial\Gamma^{(1)}_{(1,2)}$. Here Q_0 is the normalized total flux in the azimuthally symmetric case, $u_0 = \frac{2\gamma}{R}\cos\theta_c$, θ_c is the contact angle and γ is the surface tension. The solid line is the best fit to the data $Q_T/Q_0 = A\alpha^B + C$, at $A = 2.80 \times 10^4$, $B = --2.469$ and $C = 0.9065$. The data of the total flux are from (5.2) at triangulation level 7 (the maximum mesh size $h/R \approx 0.018$)

The graph 5.6 shows the non-dimensional total flux Q_T/Q_0 as a function of tilt angle αobtained with the boundary conditions at $\alpha_1/u_0 = 0.8$ and $\alpha_2/u_0 = 0.2$ on $\partial\Gamma^{(1)}_{(1,2)}$, as is shown in Fig. 5.1. Symbols are the numerical result obtained at the highest mesh refinement (maximum mesh size h/R $\approx$ 0.018). The solid line is the fit to the data $Q_T/Q_0 = A\alpha^B + C$ with $A = 2.80 \times 10^4$, $B = -2.469$ and $C = 0.9065$.

One can summarise that at relatively large tilt angles, which are close to the angle in the azimuthal symmetrical case, the liquid total flux value and hence permeability are also close to that predicted on the basis of the azimuthally symmetric solution, see equation (3.34) and the dependence is similar to that obtained for a single-sphere, see 4.4.1 in Chapter 4.

Moreover, we compare the liquid total flux and hence permeability between one sphere and two spheres, as shown in Fig.5.7. The red line illustrated the data of the liquid total flux of one sphere problem (the data shown in Table 4.4); the blue line illustrated the data of the liquid total flux of two spheres problem, showed in the data in Table 5.2.

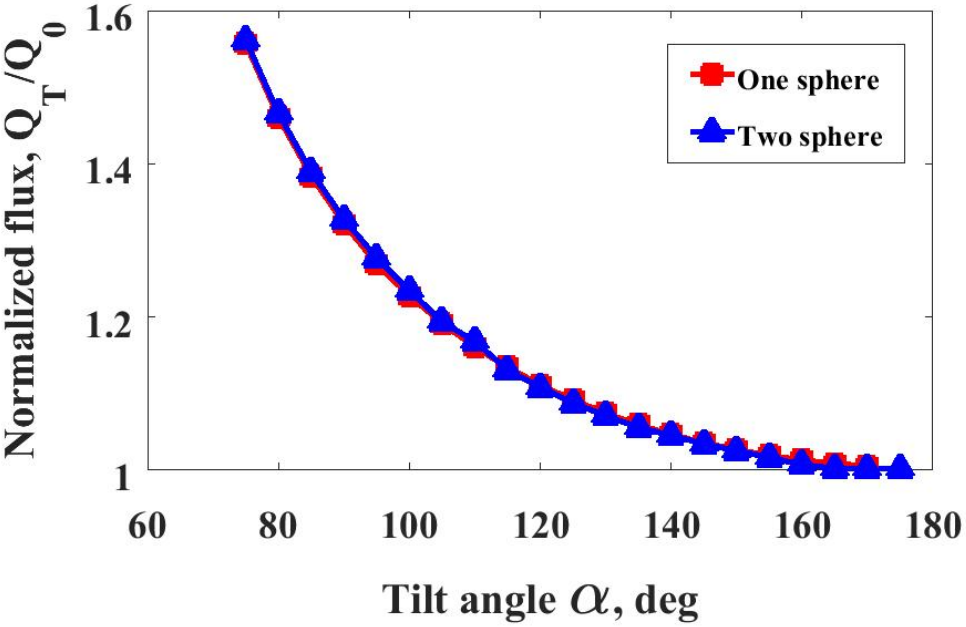

Figure 5.7: Non-dimensional total liquid flux Q_T/Q_0 as a function of the tilt angle α obtained in the solution of two problems: a single sphere with two tilted boundaries and two coupled spheres. Here, Q_0 is the normalized total flux in the azimuthally symmetric case $\alpha = \pi$.

It can be seen that the red line and the blue line have an overlap. It is shown that the permeability of a single spherical particle is identical to that of two coupled spheres as is expected according to (3.49). The effect is solely due to the symmetry of the two-coupled-particle problem and the continuity of the total flux and pressure set by the new set of the boundary conditions. As a result, the pressure at the link is an average of the boundary values $(\alpha_1 + \alpha_2)/2$, and hence we recover solutions similar to the ones found in the case of one element.

In conclusion, we have demonstrated how the coefficient of permeability of a few coupled elements of the porous matrix can be evaluated on the basis of the solution of the Laplace-Beltrami equation in the subsequent coupled domains. The idea is similar with the one used to obtain permeability of a single element, but with an addition of two coupling boundary conditions, namely the continuity of pressure and the total flux on the boundary of the internal sub domains. In azimuthally symmetric case, we were able to estimate the value of the errors. We have shown that the error converges with diminishing of the triangulation size. The optimal convergence rate observed implies that our method is efficient for solving the Leplace-Beltrami equations with the new set of the boundary conditions.

Moreover, in the symmetric case, we have shown that the total flux and hence permeability of the coupled elements can be obtained from the permeability of a single element, (3.51). The methodology developed in this and the previous chapters can be used in practical application involving more particles, as we will demonstrate in Chapter 6.

Chapter 6

Surface Permeability of a Particle Ensemble and the Laplace-Beltrami Problem.

In the previous parts of the study, we have developed a methodology based on the Laplace-Beltrami Dirichlet boundary-value problem to obtain surface permeability of porous matrix elements, which is one of the main ingredients of the super-fast diffusion model in porous media. We have thoroughly validated and demonstrated the use of the methodology by means of numerical simulations of the Laplace-Beltrami problem with the help of a specifically adopted surface finite element technique using simplified examples. We have shown, that surface permeability of a single element or a small cluster of the elements of a porous matrix can be accurately calculated by the developed method. The influence of the surface shape and the geometry, and configuration of the contacts between the particles have been investigated.

In this chapter, we will tackle a more realistic problem of the global surface permeability of a sample volume element containing many particles of an ensemble of randomly packed spheres of different diameters. This problem corresponds to a realistic scenario, when surface permeability, the macroscopic parameter, which is difficult to estimate a priori, can be accurately calculated for the use in porous media transport modelling. We have shown in Chapter 3, that permeability of particulate porous media comprised of isolated parallel chains of spherical particles coupled by liquid bridges is equivalent to permeability of a single spherical particle obtained in azimuthally symmetric case. Real configurations are more complex, and azimuthal symmetry is, of course, broken. So the objectives of this chapter are twofold. First, we study effects of tortuosity by comparing results obtained in randomly packed configurations with analytical result (3.19). Secondly, we observe permeability-saturation dependence and compare with the scaling expected according to (3.22).

6.1 Random Distribution of Spheres

To obtain a realistic distribution of the randomly packed spherical particles of different diameters, a method developed in molecular dynamics simulations has been used. In the simulations, initially uniform, but a random distribution of particles (about $200 - 3000$ particles) at some finite temperature interacting by the Lennard-Jones pair-wise potential

$$U_{ij} = \varepsilon \left\{ \left(\frac{\sigma_{ij}}{r} \right)^{12} - \left(\frac{\sigma_{ij}}{r} \right)^{6} \right\} \tag{6.1}$$

is evolving in time according to the Newton's second law under the action of an external force $\mathbf{F_e}$

$$m\frac{d\mathbf{v_i}}{dt} = -\sum_j \nabla U_{ij} + \mathbf{F_e}.$$

Here, m is particle mass, ε is an interaction parameter, r is the distance between the particle centres and $\sigma_{ij} = R_i + R_j$ is the sum of the particle radii $R_{i,j}$, which is roughly the shortest distance between the particles. The external force is applied to emulate the force of gravity in the standard procedure of obtaining a set of packed particles by gentle shaking. The shaking of the particle ensemble has been emulated by finite temperature, which then has been gradually reduced to almost zero values in the end of the procedure to obtain the randomly packed configurations. Standard cut-off procedure has been applied in the simulations to the interaction potential to reduce the costs of simulations. The particle radius distribution was normal $W(R) = \frac{1}{\sqrt{\pi}\Delta R} \exp\left(-\frac{(R-R_0)^2}{\Delta R^2} \right)$ with $\Delta R/R_0 \approx 0.3$.

The simulations were performed using an in-house C++ software package developed in the University of Reading Polymer Physics group (Lukyanov and Likhtman 2016). The temperature of the particles is controlled by a thermostat and is reduced during the simulations while the system is evolving towards the minimum energy state. The resultant minimum energy distribution at almost zero temperature corresponds to a randomly packed geometric configuration of the (spherical) particles.

6.1.1 Sample Volume Element

Once the randomly packed distribution of particles has been obtained, a sample volume element containing around $13-17$ particles to apply the Laplace-Beltrami method was cut-off preserving the particle positions, see illustration in Fig. 6.1. In order to obtain the sample volume element, we have chosen a box with characteristic dimensions L_x^B, L_y^B and L_z^B and defined its position inside the pack of particles. The box dimensions are adjusted to have approximately $13-17$ particles fully contained (the particle centre is within the radius of the particle from the box boundaries) in the box. This will be our subset, that is the sample volume element. The number of particles should be sufficient to obtain macroscopic properties by averaging, while at the same time allowing high resolution of the numerical method on each particle of the subset. We will check this a posteriori.

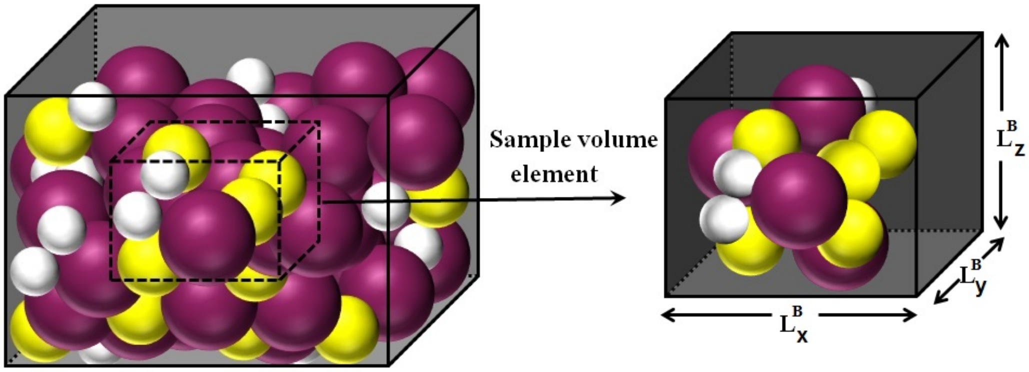

Figure 6.1: Particle ensemble and a sample volume element.

6.2 Finite Element Set-up for the Laplace-Beltrami Problem Evaluation

Once the set of test particles was chosen, the contacts between the particles are identified on the basis of the distance between the particles centres r and particle radii R_i and R_j

$$r < R_i + R_j + 0.05 \max(R_i, R_j).$$

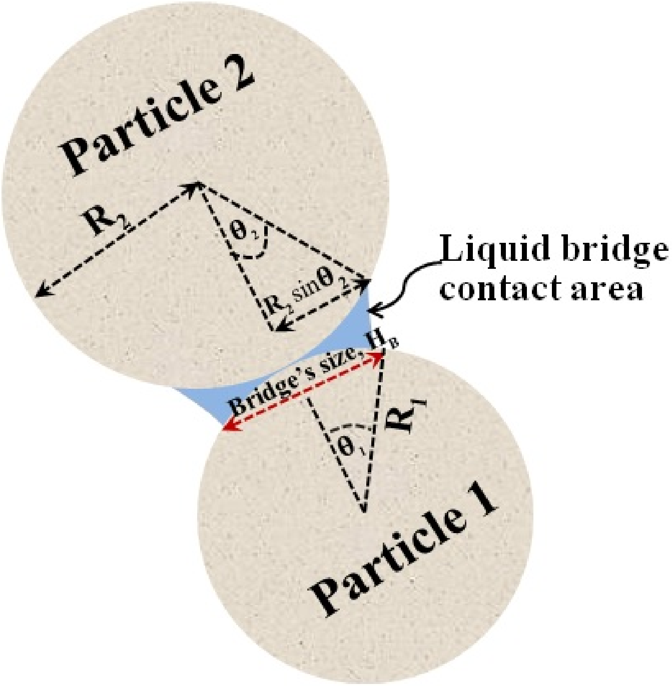

Figure 6.2: Illustration of a liquid bridge between particles and the size of bridge, H_B.

As one can see, we have allowed for some small gap between the particles to form a liquid bridge coupling the surface elements. Physically, this is justified since the liquid bridges are stable even if there is a small gap between two particles, if the gap δR is, of course, not too large $\delta R \ll R$ (Herminghaus 2005). In this chapter, we measure (normalise) all distances with respect to some average length scale R in the system, such that the average particle diameter $D/R = 1$. Once the contacts were identified, the internal and external boundaries are established on the basis of the given bridge size $2R\sin\theta_0$, see Fig.6.2. Despite the fact that radii of particles are not identical, the bridge size $2R\sin\theta_0$ can be assumed to be roughly the same if the pressure variations within the sample element are small, according to the estimate (1.22). In typical conditions of liquid spreading in porous materials, this condition is well satisfied.

After the tessellation of the domains is completed, the Laplace-Beltrami problem is solved numerically using the technique (weak formulation solved via the Galerkin method, see Bathe 2006) described in Chapters 4 and 5 with the boundary conditions formulated and discussed in Chapter 3. The external boundaries in the system, where the Dirichlet boundary conditions are set, are chosen on the particles within the characteristic distance R facing the edges in the z-direction, as is shown in Fig. 6.1. The external boundaries, the circles are oriented with zero tilt angle with respect to the z-axis. On those boundaries, we set constant pressure values u_{in} and u_{out} to generate the flow, as is shown in Fig. 6.3.

6.3 Results

For the sake of comparison, we have generated several sets of randomly packed particles together with a regular set consisting of a chain of coupled particles, similar to the problem setup (3.35)-(3.37) where the surface permeability is known, for example (3.48) and/or (3.51), see also Fig. 6.3. Consider first numerical evaluation of the surface flux in a regular set of particles, Fig. 6.3.

6.3.1 Surface Flux and Permeability in a System Consisting of Regular Sets of Particles.

Recall the system of the Laplace-Beltrami equations for the three truncated spheres.

$$-\Delta_{\Omega_0^{(1)}} u_1 = 0, \tag{6.2}$$

$$-\Delta_{\Omega_0^{(2)}} u_2 = 0, \tag{6.3}$$

and

$$-\Delta_{\Omega_0^{(3)}} u_3 = 0, \tag{6.4}$$

with the Dirichlet boundary conditions

$$u_3|_{\partial\Gamma_3^{(1)}} = u_{in} \quad \text{and} \quad u_1|_{\partial\Gamma_1^{(2)}} = u_{out} \tag{6.5}$$

and continuity boundary conditions due to small pressure gradients and the conservation of mass

$$u_1|_{\partial\Gamma_1^{(1)}} = u_2|_{\partial\Gamma_2^{(2)}} = const \quad \text{and} \quad u_2|_{\partial\Gamma_2^{(1)}} = u_3|_{\partial\Gamma_3^{(2)}} = const \tag{6.6}$$

$$\oint_{\partial\Gamma_1^{(1)}} \nabla u_1 \cdot \mathbf{n}_{s_1}|_{\partial\Gamma_1^{(1)}}\, dl = -\oint_{\partial\Gamma_2^{(2)}} \nabla u_2 \cdot \mathbf{n}_{s_2}|_{\partial\Gamma_2^{(2)}}\, dl, \tag{6.7}$$

and

$$\oint_{\partial\Gamma_2^{(1)}} \nabla u_2 \cdot \mathbf{n}_{s_2}|_{\partial\Gamma_2^{(1)}}\, dl = -\oint_{\partial\Gamma_3^{(2)}} \nabla u_3 \cdot \mathbf{n}_{s_3}|_{\partial\Gamma_3^{(2)}}\, dl, \tag{6.8}$$

where u_{in} and u_{out} are some real constants representing the pressure boundary values to create liquid flux through the system. In all numerical simulations, we fix $u_{in} = 0.8u_0$ and $u_{out} = 0.2u_0$, where $u_0 = \frac{2\gamma}{R}\cos\theta_c$ and R is the characteristic length scale.

Using the surface finite element method as described in Chapter 4 to obtain weak solutions of the system of the Laplace-Beltrami equations (6.2)-(6.8), we obtain the results shown in Fig.6.4 and Table 6.1.

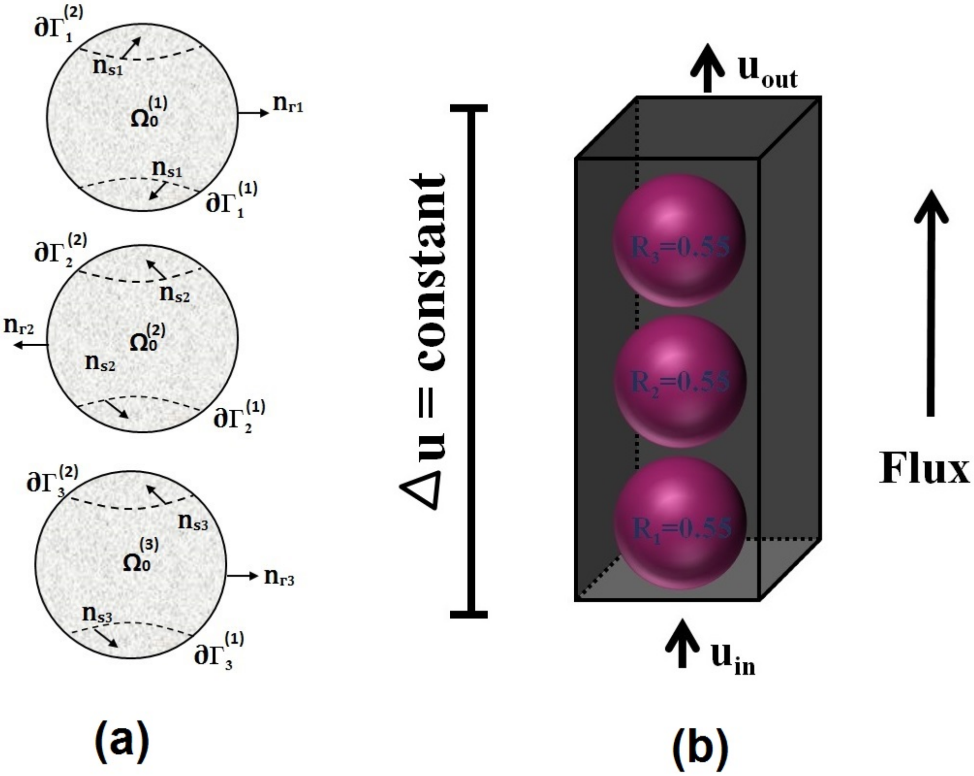

Figure 6.3: Illustration of the domains of the regular configuration $\Omega_0^{(1)}$, $\Omega_0^{(2)}$ and $\Omega_0^{(3)}$ with smooth boundary contours $\partial\Gamma_1^{(1)}$, $\partial\Gamma_1^{(2)}$, $\partial\Gamma_2^{(1)}$, $\partial\Gamma_2^{(2)}$, $\partial\Gamma_3^{(1)}$ and $\partial\Gamma_3^{(2)}$. Here, $\mathbf{n}_{\Gamma_j}$ are the outward unit normal vectors to Γ_j and $\mathbf{n}_{s_j}$ are the outward unit tangential normal vectors to the boundary contours on $\Omega_0^{(1)}$, $\Omega_0^{(2)}$ and $\Omega_0^{(3)}$ respectively.

The regular configuration of particles represent excellent benchmark problem for the numerical method and also may serve to provide a comparison to the simulations involving randomly packed particles. A regular model configuration is shown in Fig. 6.3.

We have done simulations, as before, with different mesh resolutions to verify the convergence rate and the experimental order of convergence (EOC) which is calculated by (4.11). At the same time, we have also varied the size of the bridge

$H_B = 2R \sin\theta_0$ to verify the fidelity of the approach at different entry parameters.

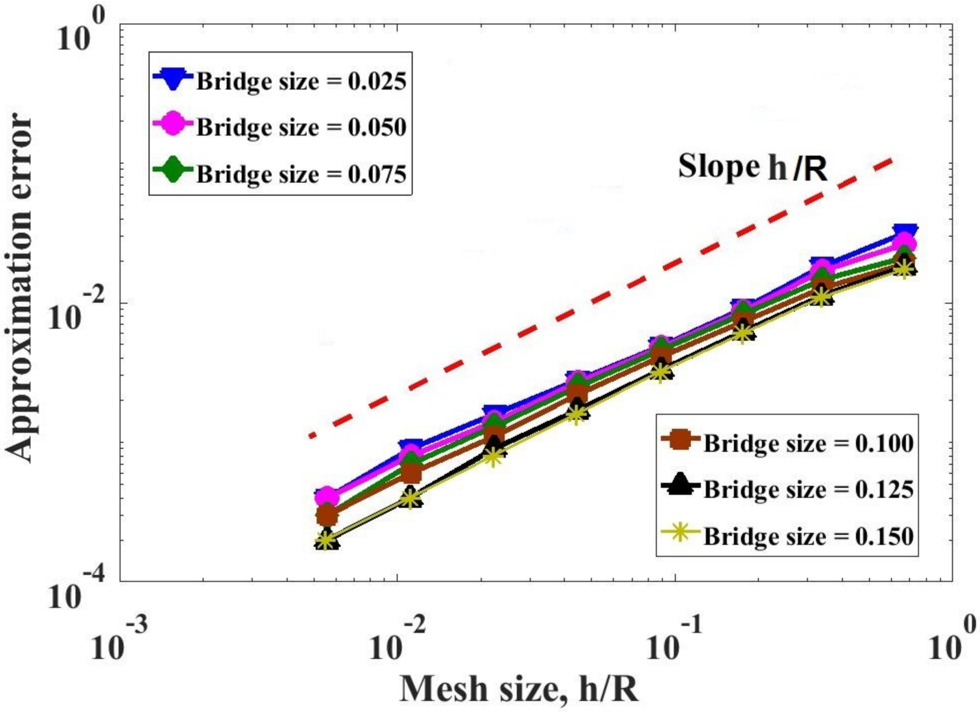

Figure 6.4: The graph illustrates the order of convergence of the surface finite elements method applied to the regular configurations of the three particles, as is shown in 6.3. The numerical data are shown by symbols and the dashed line is the slope error $\propto h/R$ shown for comparison.

Bridge size H_B/R		Triangulation Levels							
	Param.	1	2	3	4	5	6	7	8
	h/R	0.67	0.34	0.18	0.09	0.045	0.023	0.011	0.006
0.025	Error	0.03	0.02	0.009	0.005	0.003	0.002	$9 \cdot 10^{-4}$	$4 \cdot 10^{-4}$
	EOC	-	0.81	1.1	0.9	0.81	0.84	0.88	0.96
0.050	Error	0.03	0.017	0.009	0.005	0.003	0.0014	$8 \cdot 10^{-4}$	$4 \cdot 10^{-4}$
	EOC	-	0.65	1.01	0.879	0.847	0.89	0.94	0.98
0.075	Error	0.02	0.015	0.008	0.005	0.003	0.001	$7 \cdot 10^{-4}$	$3 \cdot 10^{-4}$
	EOC	-	0.53	0.88	0.86	0.88	0.93	0.97	0.99
0.100	Error	0.02	0.013	0.007	0.004	0.002	0.001	$6 \cdot 10^{-4}$	$3 \cdot 10^{-4}$
	EOC	-	0.57	0.85	0.86	0.9	0.95	0.98	0.99
0.125	Error	0.02	0.011	0.006	0.003	0.002	$9 \cdot 10^{-4}$	$4 \cdot 10^{-4}$	$2 \cdot 10^{-4}$
	EOC	-	0.7	0.9	0.92	0.95	0.98	0.99	1
0.150	Error	0.02	0.01	0.006	0.003	0.002	$8 \cdot 10^{-4}$	$4 \cdot 10^{-4}$	$2 \cdot 10^{-4}$
	EOC	-	0.67	0.92	0.93	0.96	0.98	0.99	1

Table 6.1: Approximation error in H^1 semi-norm (Error) and the experimental order of convergence (EOC) (4.11) of the surface finite element method applied to the regular distribution of spherical particles, Fig. 6.3, as a function of the mesh size h/R at different bridge length scales H_B/R.

The results are summarised in Fig. 6.4 and in Table 6.1. As one can see, as we expected the convergence rate is the first order in H^1 semi-norm. It is vital that the rate of convergence is uniform with respect to different size of the boundary H_B/R, that is the area covered by the bridge. In real conditions, as capillary pressure in the system is varied during the spreading, the size varies at the same rate, so that the uniform convergence guarantees solid output of the numerical simulations in different conditions.

Before comparing the simulation results of the regular distribution of particles with the different configurations, we now calculate the total liquid flux at different sizes of bridges, which is summarised in Table 6.2.

Bridge size H_B/R	Reduced Liquid Flux Q_T/S_0Q_0	
	Numerical solutions	Exact Solutions
0.0250	0.650	0.702
0.0500	0.781	0.830
0.0750	0.900	0.930
0.1000	0.995	1.017
0.1250	1.073	1.097
0.1500	1.162	1.172

Table 6.2: Tabulated values of the total liquid flux Q_T/S_0Q_0 through the system shown in Fig. 6.3 at different values of the bridge size H_B/R obtained in numerical simulations versus exact analytical solution at the triangulation level 8 with the maximum mesh size $h/R = 0.006$. Here, $Q_0 = \delta_R \frac{\kappa_m}{\mu} \frac{u_{in} - u_{out}}{\bar{L}_z^B}$, $u_{in} - u_{out} = 0.6\, u_0$, $u_0 = \frac{2\gamma}{R} \cos\theta_c$, θ_c is the contact angle, γ is the surface tension, δ_R is the characteristic length scale of the surface roughness, κ_m is the local permeability, μ is liquid viscosity, $S_0 = L_x^B L_y^B / R^2$. The total flux for the exact solution is calculated by means of equation (3.47).

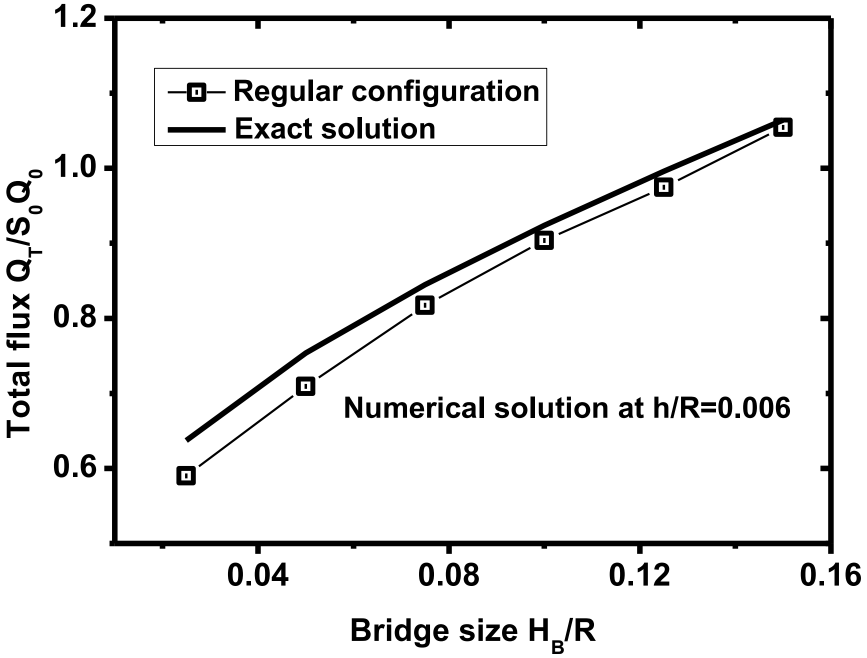

Figure 6.5: Comparison of the reduced flux Q_T/S_0Q_0 obtained in the numerical (symbols) and exact (solid line) solutions (3.44)-(3.46) as a function of bridge size H_B/R. Here, $Q_0 = \delta_R \frac{\kappa_m}{\mu} \frac{u_{in} - u_{out}}{\bar{L}_z^B}$, $u_{in} - u_{out} = 0.6\, u_0$, $u_0 = \frac{2\gamma}{R} \cos\theta_c$, θ_c is the contact angle, γ is the surface tension, δ_R is the characteristic length scale of the surface roughness, κ_m is the local permeability, μ is liquid viscosity, $S_0 = L_x^B L_y^B / R^2$.

Since the regular distribution of particles is described by the analytical solution (3.44)-(3.46), one can also compare them rigorously as functions of the boundary length scale, which is shown in Fig. 6.5. As one can see, the two curves are almost identical, as is expected. The largest error is observed at small size of the boundary contour due to the reduced resolution of the boundary line in the triangulation. We can conclude now that the numerical method can be safely applied to investigate the permeability of a random pack.

6.3.2 Permeability in a Random Configuration and the Laplace-Beltrami Method

We will now simulate steady surface flows in several randomly generated configurations of spherical particles of different diameters, as is illustrated in Fig. 6.7. The Dirichlet boundary conditions are applied to the particle surfaces at the top and the bottom of the pack, as is indicated in Fig. 6.7.

The idea of this investigation is many-fold. First of all, we would like to establish how the effective surface flux density Q_T/S_0Q_0 through the system varies with the configuration. Given that we have many particles in the pack randomly distributed, it is expected that the variations should be on the level defined by the number of particles, that is no more than 20%. We can achieve a better comparison of the configuration properties by measuring the flux density as a function of the bridge size. Varying the bridge size, one can also verify the scaling of the coefficient of diffusion $D \propto \frac{1}{\ln(s-s_0)}$ found in our previous analysis, which follows from the analytical form of the total flux (3.47). This would have practical meaning, since in applications one needs to have a simple way to estimate transport properties of porous matrices. Notice that, for the sake of the fair comparison between different configurations, we have reduced the total flux Q_T by the non-dimensinal cross-section area $S_0 = L_x^B L_y^B / R^2$ and by some characteristic value

$$Q_0 = \delta_R \frac{\kappa_m}{\mu} \frac{u_{in} - u_{out}}{\bar{L}_z^B}, \quad \bar{L}_z^B = L_z^B / R.$$

The later takes into account different system dimensions while applying constant pressure difference $u_{in} - u_{out} = 0.6\, u_0$. This reduction allows to compare geometrically different configuration by bringing them into equivalent conditions. Here, $u_0 = \frac{2\gamma}{R}\cos\theta_c$, θ_c is the contact angle, γ is the surface tension, δ_R is the characteristic length scale of the surface roughness, κ_m is the local permeability, μ is liquid viscosity.

To consider the problem of randomly packed spheres, we first recall the system of the Laplace-Beltrami equations for many, say k coupled particles, which is discussed in Chapter 3,

$$-\Delta_{\Omega_0^{(k)}} u = 0. \tag{6.9}$$

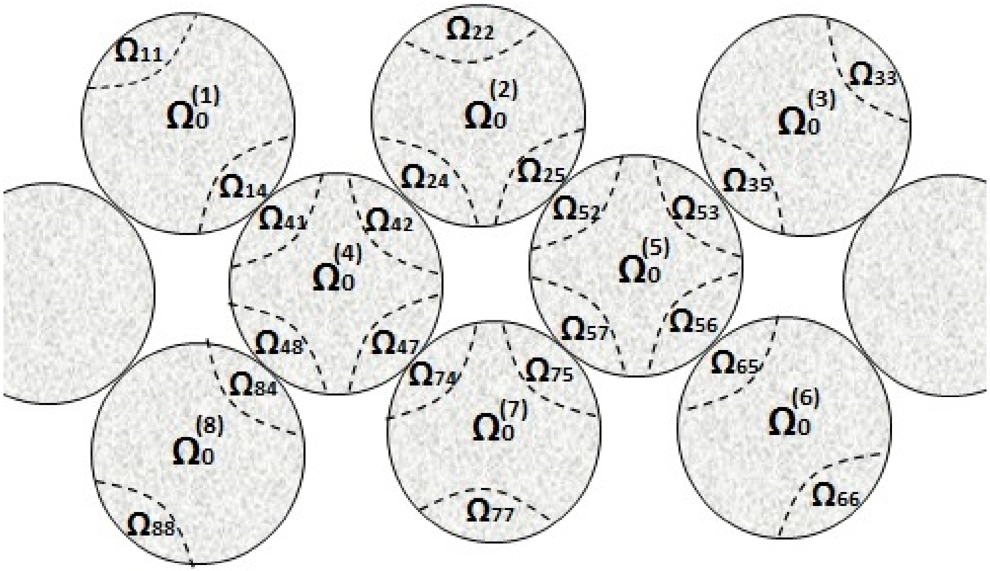

Figure 6.6: Illustration of the domains for the multi-particle connected problem

The Laplace-Beltrami system is augmented with the boundary conditions. On the internal boundaries of the sub-domains, one has continuity conditions

$$u|_{\partial\Gamma_k^{(j)}} = u|_{\partial\Gamma_j^{(k)}} = \text{constant}, \tag{6.10}$$

$$\oint_{\partial\Gamma_k^{(j)}} \nabla u \cdot \mathbf{n}_s|_{\partial\Gamma_k^{(j)}}\, dl = -\oint_{\partial\Gamma_j^{(k)}} \nabla u \cdot \mathbf{n}_s|_{\partial\Gamma_j^{(k)}}\, dl, \tag{6.11}$$

and on the external boundaries of the sub-domains, the Dirichlet conditions are set to generate the flow through the system

$$u|_{\partial\Gamma_k^{(k)}} = \quad u_{in} \quad \text{or} \quad u_{out} \quad = \text{constant}. \tag{6.12}$$

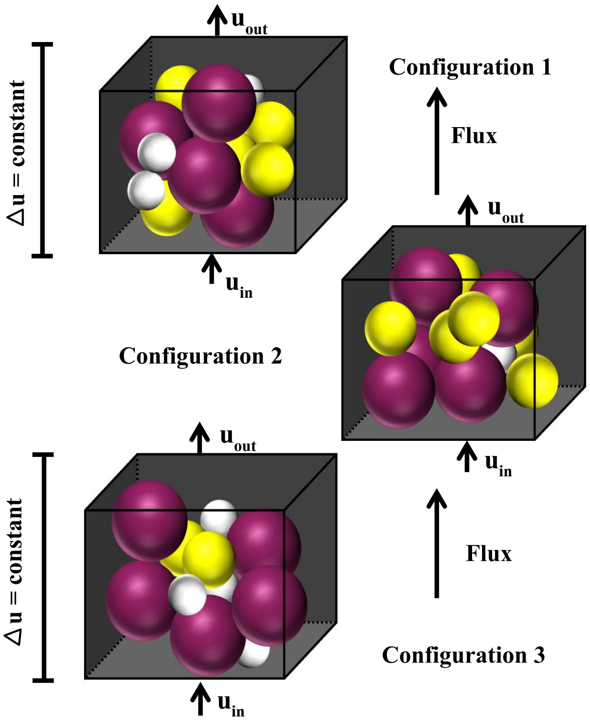

Figure 6.7: Random configurations of spherical particles with radius $R_1 = 0.53R$ (purple), $R_2 = 0.42R$ (yellow) and $R_3 = 0.31R$ (white). Here, the boundary conditions are fixed at $u_{in} = 0.8\, u_0$ and $u_{out} = 0.2\, u_0$.

We will consider four representative configurations consisting of the particles of size $R_1 = 0.53\,R$, $R_2 = 0.42\,R$, $R_3 = 0.31\,R$ and $R = 0.55\,R$. Here the number of particle in configuration 1, configuration 2, configuration 3 and regular configuration are $15, 17, 13$ and 3 respectively. Using the surface finite element method, which is described in Chapter 4 to solve the system of the Laplace-Beltrami equations (6.9)-(6.12), we obtain the results in Table 6.3, Fig. 6.8.

Bridge size	Reduced total flux Q_T/S_0Q_0			
	Config. 1	Config. 2	Config. 3	Regular (Fig.6.3)
H_B/R	N=15, $L_x^B = 2.8R$, $L_y^B = 2.5R$, $L_z^B = 3R$	N=17, $L_x^B = 3.1R$, $L_y^B = 2.6R$, $L_z^B = 2.7R$	N=13, $L_x^B = 2.8R$, $L_y^B = 2R$, $L_z^B = 2.9R$	N=3, $L_x^B = 1.1R$, $L_y^B = 1.1R$, $L_z^B = 3.3R$
0.025	0.3	0.26	0.33	0.65
0.050	0.39	0.35	0.43	0.78
0.075	0.46	0.4	0.49	0.9
0.100	0.51	0.45	0.55	1.
0.125	0.55	0.49	0.6	1.1
0.150	0.6	0.53	0.66	1.2

Table 6.3: Tabulated values of the non-dimensional total liquid flux Q_T/S_0Q_0 in different configurations with the different bridge size H_B/R. Here, N is the number of particles in the sample. Notice that, the configurations 1, 2 and 3 consist of the particles with radii $R_1 = 0.53\,R$, $R_2 = 0.42\,R$ and $R_3 = 0.31\,R$ respectively, while the regular configuration consists of the particles with radius $R_1 = 0.55\,R$.

If we look at the trend of the reduced flux Q_T/S_0Q_0 passing through the randomly packed configuration, one can see that the flux is a monotonically increasing function of the bridge size H_B/R, as is predicted on the basis of the azimuthally symmetric solution (3.20).

Moreover, one can see that the value of the flux Q_T/S_0Q_0 and hence the permeability of the random configuration is lower than that of the regular configuration. Consequently, this is an indication of the tortuosity effects in the randomly packed particles, that is longer pathways for the liquid to pass through the system. In total, the tortuosity effect can be estimated as a factor of two reduction of the system permeability. As it was expected, the variations of the flux dependencies in different random geometric configurations was within $10-20\%$. This justifies the chosen size of the sample volume elements.

Next, we analyse the permeability-saturation dependence and compare with the scaling expected according (3.22). To do so, we present the flux Q_T/S_0Q_0 as the function of the bridge size relationship inspired by (3.47) taking into account that $H_B = 2R\sin\theta_0$

$$g(H_B) = \ln^{-1}\left(\frac{1+\sqrt{1-\left(\frac{H_B}{2R}\right)^2}}{1-\sqrt{1-\left(\frac{H_B}{2R}\right)^2}}\right).$$

As one can see, Fig. 6.8, all the dependencies are straight lines indicating that indeed, the scaling found in the analysis of a single particle element is fully applicable here with correction coefficient to take into account the tortuosity effects.

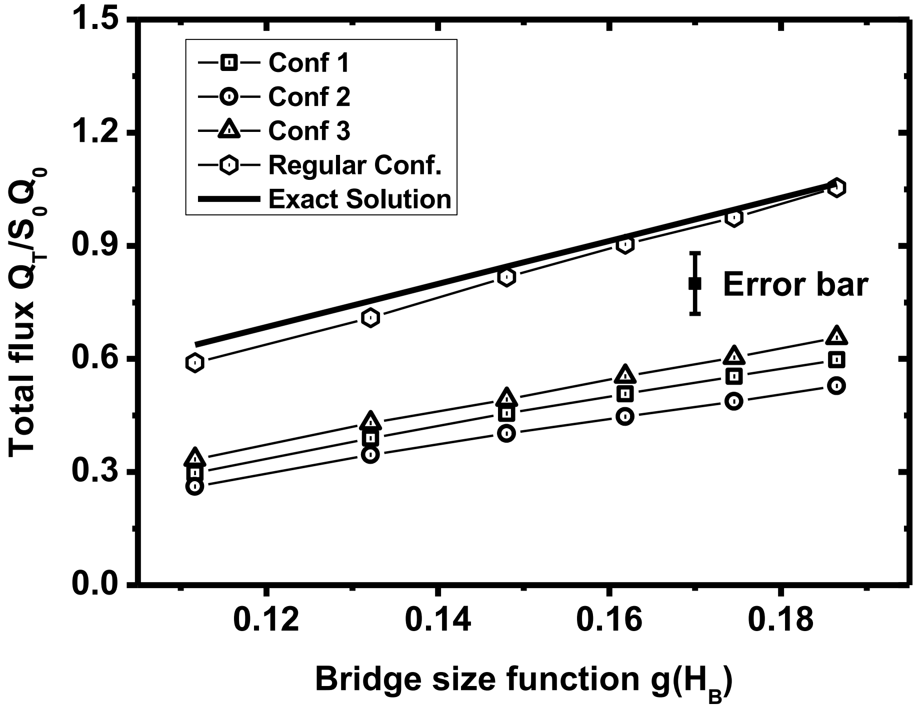

Figure 6.8: Reduced total flux Q_T/S_0Q_0 as a function of bridge size, $g(H_B) = \ln^{-1}\left(\frac{1+\sqrt{1-\left(\frac{H_B}{2R}\right)^2}}{1-\sqrt{1-\left(\frac{H_B}{2R}\right)^2}}\right)$ in the set up with the pressure at the boundary $u_{in} = 0.2\,u_0$ and $u_{out} = 0.8\,u_0$ as is shown in Fig. 6.7. Here, $Q_0 = \delta_R \frac{\kappa_m}{\mu}\frac{u_{in} - u_{out}}{\bar{L}_z^B}$ and $S_0 = L_x^B L_y^B/R^2$. Symbols are the numerical solutions and the solid line is the exact result. The error indicates potential dispersion of the flux values (20%) due to the finite number of particles in the sample volume element.

The results obtained in this chapter have been **submitted** to a journal (Sirimark et al. 2019).

Chapter 7

Conclusions and Future Work

We have demonstrated that transport processes in different porous matrices at low saturation levels can be simulated with high accuracy using the techniques developed and analysed in the study presented in the thesis. In particular, in Chapter 2 we have demonstrated how transport in fibrous porous materials at low saturation levels can be simulated using a mesoscopic network model. Based on the mesoscopic description, we have been able to validate a macroscopic approach to deal with this kind of problems, which requires less computational resources if it can be applied.

In Chapters 3, 4, 5 and 6 we have shown how permeability of particulate porous media can be investigated rigorously using the methodology based on the Laplace-Beltrami Dirichlet boundary value problem. We have formulated the problem of permeability calculation in terms of the Laplace-Beltrami problem in Chapter 3. Then, we have thoroughly verified the surface finite element technique with application to the problem in Chapters 4 and 5. Finally, in Chapter 6, we have demonstrated the application of the whole methodology to study permeability of randomly distributed particles. Based on the analysis presented in Chapters 4,5, and 6, we can conclude that the technique is ready to be applied to real problems involving, practically, arbitrary shapes and surfaces.

There are several problems we have not studied yet, but which could be of immediate practical importance as far as the developed method is concerned. First of all, this would be interesting to study surfaces with topological singularities, such as folds and/or cusps, for example. This would allow to extend the technique to more realistic situations, which can be found in practice. The second immediate goal, we have no time to investigate, is the situations (often found in applications) when the surface has many areas inaccessible to the flow, as is schematically shown in Fig. 7.1 by contours $\partial\gamma$. This can be further generalised to the case, when there are regions absorbing the liquid from the surface flow, contours $\partial\zeta$ in Fig. 7.1. For example, many porous materials have particles with internal structure so that the liquid may be soaked by the particle interior. This can be considered on the basis of the developed methodology by introducing some Neumann boundary conditions on the contours $\partial\zeta$, as is shown in Fig. 7.1.

As an extension of the network methodology developed in Chapter 2 of the thesis, this would be interesting to consider more complex fibrous materials involving a distribution of defects of a characteristic length scale different from the length scales involved. Also, the model can be generalised to a situation when the links have some internal structure, so that permeability of the links would depend on the history of the wetting process.

Concerning more long-term plans, in many industrial applications surface flows are accompanied by chemical reactions also taking place on the element surfaces. For example, many catalysis reactions are surface driven. This may require reformulation of the problem to study potential dynamic processes. It is completely in the realms of the developed methodology and the numerical techniques.

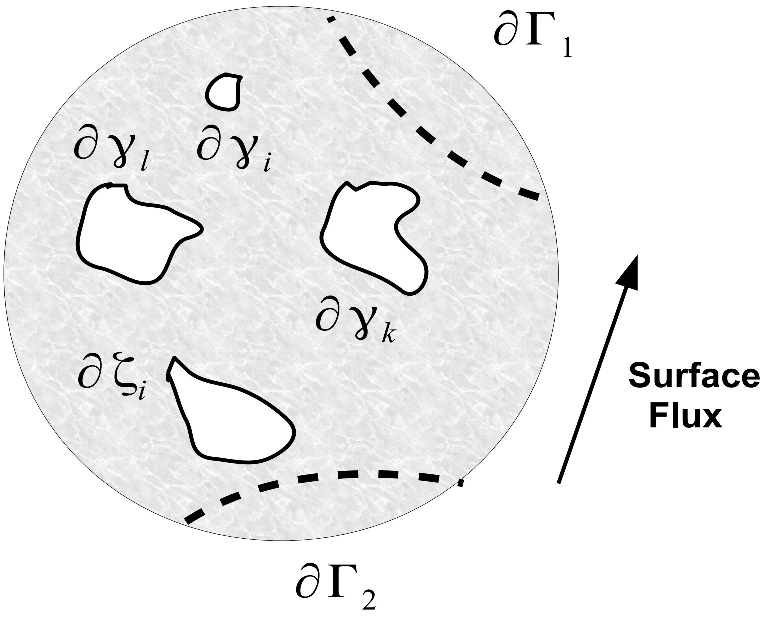

Figure 7.1: Illustration of a porous media particle with inaccessible areas $\partial\gamma$ and sink/source regions $\partial\zeta$. Contours $\partial\Gamma_{1,2}$ designate the footprint of the liquid bridge areas, as before.

Appendices

A The Numerical Simulation of the Network Model

In this model, we will consider a two-dimensional domain $\Omega \subset R^2$. An irregular Cartesian discretisation of the domain Ω is defined by distribution of nodes i. Let p_i be the pressure at each node i with the liquid volume V_B^i.

$$p_i = -\left(\frac{1}{V_B^i}\right)^{1/2}. \tag{A.1}$$

In fact, the liquid mass is $M_i = \rho V_B^i$, where ρ is liquid density. The flux I_{ij} between the nodes i and j, for example, can be presented as

$$I_{ij} = -\alpha_{ij}\,\frac{p_j - p_i}{L_{ij}}. \tag{A.2}$$

Here, the coefficient α_{ij} is an additional parameter to describe the links physical properties associated with their conductivity, p_i and p_j are the pressure at the nodes i and j respectively, and L_{ij} is the length of the link connecting the nodes.

If we consider evolution of the network during a small (theoretically infinitesimal, but in practice finite) time interval Δt the volumetric flux is obviously given by

$$I_{ij} = \frac{M_i^{n+1} - M_i^n}{\Delta t} \tag{A.3}$$

where, M_i^n is the mass at the node i at the time step n, and I_{ij} is the volumetric flux between nodes.

B Algorithm of the Network Model

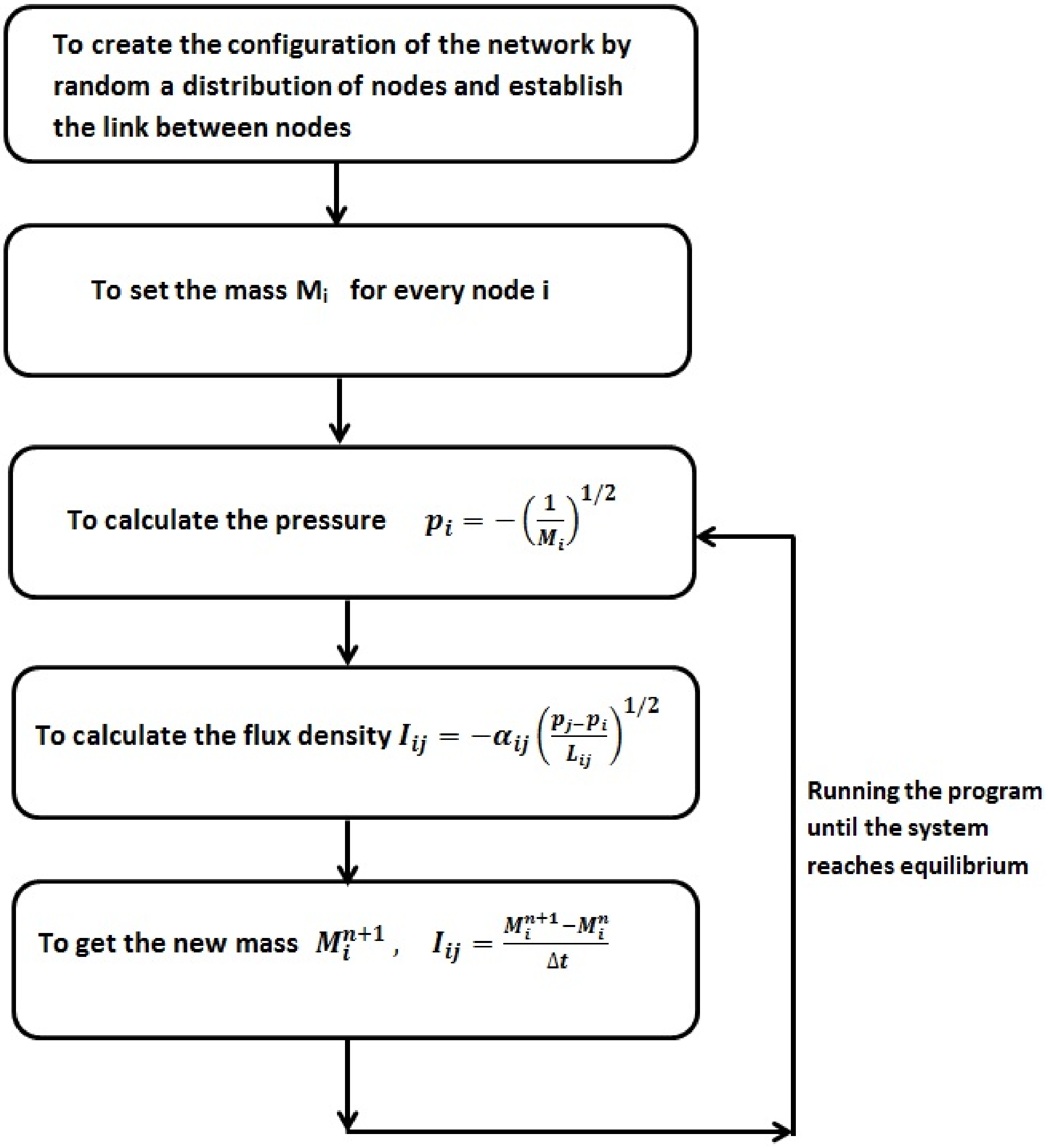

Figure B.1: Algorithm of the network model.

C Implementation of the Surface Finite Element Method

Surface discretization and parametric projection

We have generated the surface discretization by using a standard application, the GMSH software (Geuzaine and Remacle 2006). From the application output, we can extract the node coordinates x_i, y_i, z_i and the node arrangement in each particular triangular element. All triangular elements, that is the position of the nodes are then projected into the standard parametric domain (ξ, η), such that the vertices of the triangles have always coordinates $(0,0),(0,1)$ and $(1,0)$, as is shown in Fig. C.1.

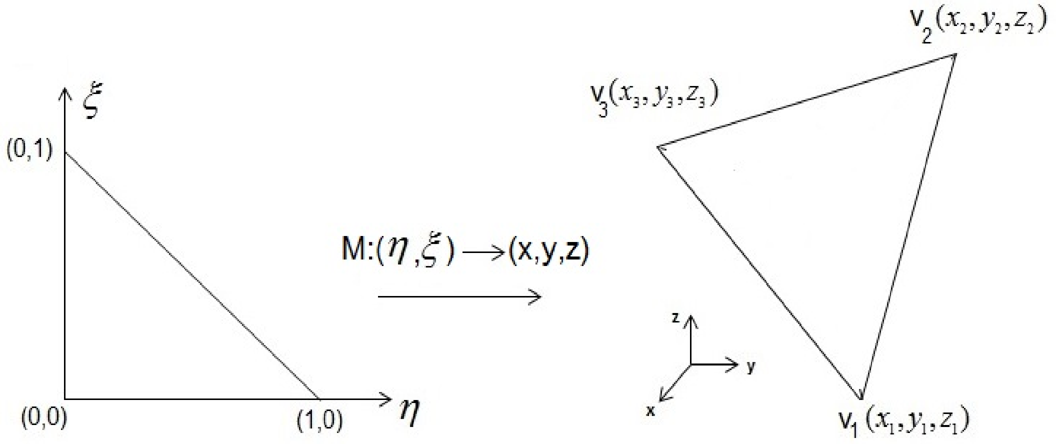

Figure C.1: Linear mapping between a reference triangles in the local coordinate system (η, ξ) (Left) and the physical coordinate system (x, y, z) (Right).

Consider the discrete surface Γ_h which consists of the set of the triangles, see Figure 4.2. In order to construct a mapping between a reference triangle in the local coordinate system (η, ξ) and the physical coordinate system (x, y, z), such that

$$M : (\eta, \xi) \to (x, y, z).$$

From the paramatric mapping, We first define $\mathbf{x}_\Gamma(\eta, \xi)$ which is the point on the surface Γ_h. From Theorem 3.2, for any given parametric mapping, we can extend its outside the surface by

$$\mathbf{x}(\eta, \xi, \zeta) = \mathbf{x}_\Gamma(\eta, \xi) + \zeta \mathbf{n}_\Gamma(\eta, \xi) \tag{C.1}$$

here the signed distance function ζ is chosen i.e $-t/2 \leq \zeta \leq t/2$ and $\mathbf{n}_\Gamma$ is the normal.

Next we specialize to the finite element parametrization of the surface :

$$\mathbf{x}_{\Gamma_h}(\eta, \xi) = \sum_i^n \mathbf{x}_i \Phi_i(\eta, \xi) \tag{C.2}$$

where $\mathbf{x}_i$ is the nodal point of triangles and the linear shape functions used in the FEM calculations $\Phi_i(\eta, \xi)$ are defined by

$$\Phi_1 = 1 - \eta - \xi, \quad \Phi_2 = \eta, \quad \Phi_3 = \xi,$$

with the derivatives

$$\left[\frac{\partial \Phi_1}{\partial \xi}, \quad \frac{\partial \Phi_2}{\partial \xi}, \quad \frac{\partial \Phi_3}{\partial \xi}\right] = [-1, \quad 0, \quad 1]$$

and

$$\left[\frac{\partial \Phi_1}{\partial \eta}, \quad \frac{\partial \Phi_2}{\partial \eta}, \quad \frac{\partial \Phi_3}{\partial \eta}\right] = [-1, \quad 1, \quad 0].$$

Using the parametrization to extend this approximation outside the surface, thus (C.1) can be approximated by

$$\mathbf{x}(\eta, \xi, \zeta) \approx \mathbf{x}_h(\eta, \xi, \zeta) = \mathbf{x}_{\Gamma_h}(\eta, \xi) + \zeta \mathbf{n}_{\Gamma_h}(\eta, \xi), \tag{C.3}$$

where the normal vector at each node to the element surface is defined as follows

$$\mathbf{n}_{\Gamma_h} = \frac{\dfrac{\partial \mathbf{x}_{\Gamma_h}}{\partial \eta} \times \dfrac{\partial \mathbf{x}_{\Gamma_h}}{\partial \xi}}{\left| \dfrac{\partial \mathbf{x}_{\Gamma_h}}{\partial \eta} \times \dfrac{\partial \mathbf{x}_{\Gamma_h}}{\partial \xi} \right|}.$$

Now, the finite element method can be employed to approximate the derivative of the chosen shape function Φ on the surface, at the local coordinate (η, ξ)

$$\nabla \Phi = \begin{bmatrix} \dfrac{\partial \Phi_i}{\partial x} \\ \dfrac{\partial \Phi_i}{\partial y} \\ \dfrac{\partial \Phi_i}{\partial z} \end{bmatrix} = J^{-1}(\eta, \xi, 0) \begin{bmatrix} \dfrac{\partial \Phi_i}{\partial \eta} \\ \dfrac{\partial \Phi_i}{\partial \xi} \\ \dfrac{\partial \Phi_i}{\partial \zeta} \end{bmatrix},$$

where the Jacobian is

$$J(\eta, \xi, \zeta) = \begin{vmatrix} \dfrac{\partial x_h}{\partial \eta} & \dfrac{\partial y_h}{\partial \eta} & \dfrac{\partial z_h}{\partial \eta} \\ \dfrac{\partial x_h}{\partial \xi} & \dfrac{\partial y_h}{\partial \xi} & \dfrac{\partial z_h}{\partial \xi} \\ \dfrac{\partial x_h}{\partial \zeta} & \dfrac{\partial y_h}{\partial \zeta} & \dfrac{\partial z_h}{\partial \zeta} \end{vmatrix}.$$

Note that, we have $\dfrac{\partial \Phi_i}{\partial \zeta} = 0$. Consequently, the derivative of the shape function on the surface is approximated by

$$\nabla\Phi = \begin{bmatrix} \dfrac{\partial\Phi_i}{\partial x} \\ \dfrac{\partial\Phi_i}{\partial y} \\ \dfrac{\partial\Phi_i}{\partial z} \end{bmatrix} = J^{-1}(\eta,\xi,0) \begin{bmatrix} \dfrac{\partial\Phi_i}{\partial\eta} \\ \dfrac{\partial\Phi_i}{\partial\xi} \\ 0 \end{bmatrix}.$$

From (C.3), one can obtain $\dfrac{\partial\mathbf{x}_h}{\partial\xi} = \mathbf{n}_{\Gamma_h}$. Therefore, the Jacobian on Γ can be rewritten as follows:

$$J(\eta,\xi,0) = \begin{vmatrix} \dfrac{\partial x_h}{\partial\eta} & \dfrac{\partial y_h}{\partial\eta} & \dfrac{\partial z_h}{\partial\eta} \\ \dfrac{\partial x_h}{\partial\xi} & \dfrac{\partial y_h}{\partial\xi} & \dfrac{\partial z_h}{\partial\xi} \\ \mathbf{n}_{\Gamma_{h,x}} & \mathbf{n}_{\Gamma_{h,y}} & \mathbf{n}_{\Gamma_{h,z}} \end{vmatrix},$$

where

$$\frac{\partial x_h}{\partial\eta} = \sum_i \frac{\partial\Phi(\eta,\xi)}{\partial\eta} x_{h,i}.$$

From the outlined methodology, the surface gradient of a function u can be approximated by

$$\nabla_\Gamma u \approx \sum_i \nabla_\Gamma\Phi u_i,$$

where

$$\nabla_\Gamma\Phi = (\mathbb{I} - \mathbf{n}_{\Gamma_h} \oplus \mathbf{n}_{\Gamma_h})\nabla\Phi_i = P_\Gamma\nabla\Phi_i$$

and $\mathbb{I}$ is a 3×3 matrix.

Note, more information can be found in the works (Cenanovic et al. 2017) and (Hansbo and Larson 2014).

Bibliography

Abramowitz, M. and Stegun, I. (1970). *Handbook of Mathematical Functions with Formulas, Graphs, and Mathematical Tables.* NBS, 9 edition.

Alava, M. J. and Niskanen, K. J. (1994). The physics of paper. *Rep. Prog. Phys.*, 69:669–723.

Alshibli, K. A. and Alsaleh, M. I. (2004). Characterizing surface roughness and shape of sands using digital microscopy. *J. Comput. Civil Eng.*, 18:36–45.

Baker, R. A. (1963). Theory of ground water movement: by p. ya. polubarinova-kochina, translated, princeton, princeton university press.

Barenblatt, G. I. (2003). *Scaling*, volume 34. Cambridge University Press.

Barenblatt, G. I. (2014). *Flow, deformation and fracture: Lectures on fluid mechanics and the mechanics of deformable solids for mathematicians and physicists*, volume 49. Cambridge University Press.

Bathe, K.-J. (2006). *Finite element procedures.* Klaus-Jurgen Bathe.

Bear, J. (2013). *Dynamics of fluids in porous media.* Courier Corporation.

Bear, J. and Verruijt, A. (1987). Theory and applications of transport in porous media. *Modeling of groundwater flow and pollution, Dordrecht: Reidel.*

Bear, J. and Verruijt, A. (2012). *Modeling groundwater flow and pollution*, volume 2. Springer Science & Business Media.

Bronkhorst, C. A. (2003). Modelling paper as a two-dimensional elastic–plastic stochastic network. *International Journal of Solids and Structures*, 40(20):5441–5454.

Brown, G. O. (2002). Henry darcy and the making of a law. *Water Resources Research*, 38(7):11–1.

Cenanovic, M., Hansbo, P., and Larson, M. G. (2017). Finite element procedures for computing normals and mean curvature on triangulated surfaces and their use for mesh refinement. *arXiv preprint arXiv:1703.05745*.

Chen, J., Wang, C., Wei, N., Wan, R., and Gao, Y. (2016). 3d flexible water channel: stretchability of nanoscale water bridge. *Nanoscale*, 8:5676–5681.

Corte, H. and Kallmes, O. J. (1962). Statistical geometry of a fibrous network. In *The Formation and Structure of Paper*, pages 13–46.

Denoth, A. (1999). Wet snow pendular regime: the amount of water in ring-shaped configurations. *Cold regions science and technology*, 30(1-3):13–18.

Dimri, V. P., Srivastava, R. P., and Vedanti, N. (2012). *Fractal models in exploration geophysics: applications to hydrocarbon reservoirs*, volume 41. Elsevier.

Dziuk, G. and Elliott, C. M. (2007). Surface finite elements for parabolic equations. *Journal of Computational Mathematics*, pages 385–407.

Dziuk, G. and Elliott, C. M. (2013). Finite element methods for surface pdes. *Acta Numerica*, 22:289–396.

Eichhorn, S. J. and Sampson, W. W. (2005). Statistical geometry of pores and statistics of porous nanofibrous assemblies. *J. R. Soc. Interface*, 2:309–318.

Enríquez-Cervantes, C. J. and Rodríguez-Dagnino, R. M. (2015). A super-resolution image reconstruction using natural neighbor interpolation. *Computación y Sistemas*, 19(2):211–231.

Ern, A. and Guermond, J.-L. (2013). *Theory and practice of finite elements*, volume 159. Springer Science & Business Media.

Evans, L. C. (2010). *Partial differential equations.* American Mathematical Society.

Freeze, R. Allan, J. A. C. (1979). *GROUNDWATER.* Prentice-Hall.

Gärtner, B. and Hoffmann, M. (2014). Computational geometry lecture notes1 hs 2012.

Geuzaine, C. and Remacle, J.-F. (2006). Gmsh. *URL http://www. geuz. org/gmsh.*

Guzman, J., Madureira, A., Sarkis, M., and Walker, S. (2018). Analysis of the finite element method for the laplace–beltrami equation on surfaces with regions of high curvature using graded meshes. *Journal of Scientific Computing*, 77(3):1736–1761.

Hansbo, P. and Larson, M. G. (2014). Finite element modeling of a linear membrane shell problem using tangential differential calculus. *Computer Methods in Applied Mechanics and Engineering*, 270:1–14.

Hebey, E. (2000). *Nonlinear analysis on manifolds: Sobolev spaces and inequalities*, volume 5. American Mathematical Soc.

Herminghaus, S. (2005). Dynamics of wet granular matter. *Advances in Physics*, 54(3):221–261.

Jackaman, J., Papamikos, G., and Pryer, T. (2019). The design of conservative finite element discretisations for the vectorial modified kdv equation. *Applied Numerical Mathematics*, 137:230–251.

Jost, J. (2007). *Partial Differential Equations (Graduate Texts in Mathematics)*. Springer New York.

Koorevaar, P., Menelik, G., and Dirksen, C. (1983). *Elements of soil physics*, volume 13. Elsevier.

Leverett, M. et al. (1941). Capillary behavior in porous solids. *Transactions of the AIME*, 142(01):152–169.

Lukyanov, A. V. and Likhtman, A. E. (2016). Dynamic contact angle at the nanoscale: A unified view. *Nano*, 10:6045–6053.

Lukyanov, A. V., Sushchikh, M. M., Baines, M. J., and Theofanous, T. G. (2012). Superfast nonlinear diffusion: Capillary transport in particulate porous media. *Physical review letters*, 109(21):214501.

Melnikov, K., Mani, R., Wittel, F. K., Thielmann, M., and Herrmann, H. J. (2015). Grain-scale modeling of arbitrary fluid saturation in random packings. *Physical Review E*, 92(2):022206.

Melnikov, K., Wittel, F. K., and Herrmann, H. J. (2016). Micro-mechanical failure analysis of wet granular matter. *Acta Geotechnica*, 11(3):539–548.

Miller, C. A. and Neogi, P. (2007). *Interfacial phenomena: equilibrium and dynamic effects*. CRC Press.

Millington, R. J. and Quirk, J. P. (1961). Permeability of porous solids. *Transactions of the Faraday Society*, 57:1200–1207.

Montzka, C., Herbst, M., Weihermüller, L., Verhoef, A., and Vereecken, H. (2017). A global data set of soil hydraulic properties and sub-grid variability of soil water retention and hydraulic conductivity curves. *Earth System Science Data*, 9(2):529–543.

Mualem, Y. (1974). A conceptual model of hysteresis. *Water Resources Research*, 10(3):514–520.

Mualem, Y. (1976). A new model for predicting the hydraulic conductivity of unsaturated porous media. *Water Resources Research*, 12(3):513–522.

Niskanen, K. J. and Alava, M. J. (1994a). Planar random networks with flexible fibers. *Phys. Rev. Lett.*, 73:3475.

Niskanen, K. J. and Alava, M. J. (1994b). Planar random networks with flexible fibers. *Physical review letters*, 73(25):3475.

Olshanskii, M. A., Reusken, A., and Xu, X. (2012). A volume mesh finite element method for pdes on surfaces. In *Proceedings of the European Congress on Computational Methods in Applied Sciences and Engineering (ECCOMAS 2012), Vienna, Austria*, pages 10–14. Citeseer.

Or, D. and Tuller, M. (2000). Flow in unsaturated fractured porous media: Hydraulic conductivity of rough surfaces. *Water Resour. Res.*, 36:1165–1177.

Orr, F. M., Scriven, L. E., and Rivas, A. P. (1975). Pendular rings between solids: meniscus properties and capillary force. *J. Fluid Mech.*, 67:723–742.

Pigola, S., Rigoli, M., and Setti, A. G. (2005). Maximum principles on riemannian manifolds and applications. *Memoirs of the American Mathematical Society*, 174:1–36.

Quere, D. (1999). Fluid coating on a fiber. *Ann. Rev. Fluid Mech.*, 31:347–384.

Ranner, T. (2013). Computational surface partial differential equations. proquest llc. *Ann Arbor, MI. Thesis (Ph. D.)–University of Warwick (United Kingdom).*

Ransohoff, T. C. and Radke, C. J. (1988). Laminar flow of a wetting liquid along the corners of a predominantly gas-occupied noncircular pore. *J. Colloid Interface Sci.*, 121:392–401.

Rasi, M. (2013). Permeability properties of paper materials. *Research report. Department of Physics, University of Jyväskylä*, (13).

Romero, L. A. and Yost, F. G. (1996). Flow in an open channel capillary. *J. Fluid Mech.*, 322:109–129.

Rye, R. R., Yost, F. G., and O'Toole, E. J. (1998). Capillary flow in irregular surface grooves. *Langmuir*, 14:3937–3943.

Sahimi, M. (1993). Flow phenomena in rocks: from continuum models to fractals, percolation, cellular automata, and simulated annealing. *Reviews of modern physics*, 65(4):1393.

Sampson, W. W. (2003). The statistical geometry of fractional contact area in random fibre networks. *J. Pulp Paper Sci.*, 29(12):412–416.

Sauret, A., Bick, A. D., Duprat, C., and Stone, H. A. (2014). Wetting of crossed fibers: Multiple steady states and symmetry breaking. *EPL (Europhysics Letters)*, 105(5):56006.

Sauret, A., Boulogne, F., Soh, B., Dressaire, E., and Stone, H. A. (2015). Wetting morphologies on randomly oriented fibers. *The European Physical Journal E*, 38(6):62.

Scheel, M., Seemann, R., Brinkmann, M., Di Michiel, M., Sheppard, A., and Herminghaus, S. (2008a). Liquid distribution and cohesion in wet granular assemblies beyond the capillary bridge regime. *Journal of Physics: Condensed Matter*, 20(49):494236.

Scheel, M., Seemann, R., Brinkmann, M., Michiel, M. D. I., Sheppard, A., Breidenbach, B., and Herminghaus, S. (2008b). Morphological clues to wet granular pile stability. *Nat. Mater.*, 7:189.

Shewchuk, J., Dey, T. K., and Cheng, S.-W. (2016). *Delaunay mesh generation*. Chapman and Hall/CRC.

Shikhmurzaev, Y. D. (2007). *Capillary flows with forming interfaces*. Chapman and Hall/CRC.

Sirimark, P., Lukyanov, A. V., and Pryer, T. (2018a). Surface permeability, capillary transport and the laplace-beltrami problem. *arXiv preprint*, (arXiv:1808.06077).

Sirimark, P., Lukyanov, A. V., and Pryer, T. (2018b). Surface permeability of porous media particles and capillary transport. *The European Physical Journal E*, 41(9):106.

Sirimark, P., Lukyanov, A. V., and Pryer, T. (2019). Surface permeability and surface flow tortuosity of particulate porous media. *arXiv preprint*, (arXiv:1906.03081).

Soleimani, M., Hill, R. J., and van de Ven, T. G. M. (2015). Capillary force between flexible filaments. *Langmuir*, 31(30):8328–8334.

Tuncer, N. (2013). Projected surface finite elements for elliptic equations. *Applications & Applied Mathematics*, 8(1).

Van Genuchten, M. T. (1980). A closed-form equation for predicting the hydraulic conductivity of unsaturated soils 1. *Soil Science Society of America Journal*, 44(5):892–898.

Vázquez, J. L. (2006). *Smoothing and decay estimates for nonlinear diffusion equations: equations of porous medium type*, volume 33. Oxford University Press.

Vázquez, J. L. (2007). *The porous medium equation: mathematical theory*. Oxford University Press.

Vázquez, J. L. (2014). Barenblatt solutions and asymptotic behaviour for a nonlinear fractional heat equation of porous medium type. *Journal of the European Mathematical Society*, 16:769–803.

Whitaker, S. (1969). Advances in theory of fluid motion in porous media. *Industrial & engineering chemistry*, 61(12):14–28.

Willett, C. D., Adams, M., Johnson, S. A., and Seville, J. P. K. (2000). Capillary bridges between two spherical bodies. *Langmuir*, 16:9396–9405.